Store Separations from a Supersonic Cone

THESIS

Richard J. Simko, First Lieutenant, USAF

AFIT/GAE/ENY/06-M29

DEPARTMENT OF THE AIR FORCE
AIR UNIVERSITY

AIR FORCE INSTITUTE OF TECHNOLOGY

Wright-Patterson Air Force Base, Ohio

The views expressed in this thesis are those of the author and do not reflect the official policy or position of the United States Air Force, Department of Defense, or the United States Government.

AFIT/GAE/ENY/06-M29

Store Separations from a Supersonic Cone

THESIS

Presented to the Faculty

Department of Aeronautics and Astronautics

Graduate School of Engineering and Management

Air Force Institute of Technology

Air University

Air Education and Training Command

In Partial Fulfillment of the Requirements for the

Degree of Master of Science in Aeronautical Engineering

Richard J. Simko, B.S.A.E.

First Lieutenant, USAF

March 2006

AFIT/GAE/ENY/06-M29

Store Separations from a Supersonic Cone

Richard J. Simko, B.S.A.E.
First Lieutenant, USAF

Approved:

/signed/	23 Mar 2006
Lt Col Raymond C. Maple, (Chairman)	date
/signed/	23 Mar 2006
Dr Mark F. Reeder (Member)	date
/signed/	23 Mar 2006
Maj Richard J. McMullan (Member)	date

Abstract

A CFD study of the base flow environment during an aft supersonic store separation was conducted using the Beggar CFD code. The geometry for the carrier was a 10^o half-angle cone and the store was a 10^o half-angle cone with a cylindrical base. Solid and hollow variations of the carrier were tested. Both geometries matched a previously conducted wind tunnel experiment. The free stream was set to Mach 2.93 with a Reynolds number matching the wind tunnel environment (wind tunnel Re = $3.9\text{x}10^8$/m). The Baldwin-Lomax (B-L), Spalart-Allmares (S-A) and Detached-Eddy simulation (DES) turbulence models were were applied and their impact on computed base pressures, near-wake regions, shock interactions and forces/moments on the store and carrier was evaluated. Analyses varied from an atmospheric environment to an exact replica of a wind tunnel environment where the carrier was mounted on a diamond-shaped sting.

Base pressure comparisons with empirical and theoretical models showed the S-A turbulence model to be deficient in simulating base flows. When the flow field was symmetric and free of complex turbulent structures, the B-L turbulence model did a satisfactory job of computing the mean base pressure on the base of the carrier. The DES turbulence model also provided satisfactory mean base pressures. DES also computed a more defined recirculation region in the near wake than B-L.

The presence of a cavity on the carrier had implications on the near wake region, but did not significantly affect force and moment results. The cavity caused higher velocities in the near-wake and a delayed reattachment of the base flow. The store surface pressures were lowered due to the delayed reattachment. Streamwise velocities of Mach 0.1 were found inside the cavity.

The addition of the sting created an asymmetric environment which would not be suitable for modelling an atmospheric case. Visual images of streamlines showed

flow being redirected around the carrier so symmetric conical flow was not being achieved. This affected base pressure profiles and dropped the mean base pressure computed by the DES turbulence model by 17.5% from the atmospheric case. The force coefficients on the store were significantly affected by the sting's presence when compared to atmospheric and no-sting wind tunnel cases.

Acknowledgements

There are a few people I would like to thank for helping me complete my thesis. First of all my thesis advisor, Lt Col Ray Maple, provided me with his mentorship the entire way. There were days when he sacrificed his own personal time to make sure I had the knowledge to complete my thesis. I am very happy I was lucky enough to have him as an advisor. I would also like to thank Maj Richard McMullan and Dr Mark Reeder for being on my thesis committee and also being great instructors to me in the areas of hypersonics and computational fluid dynamics. Maj Tim Jung did experimental wind tunnel tests for his own thesis with some of the configurations I used. I thank him for his help and the data he provided me with. I'd also like to extend my thanks to Rudy Johnson and AFRL/VA for sponsoring my thesis. Needless to say, without them this thesis would not exist. Last but not least, I'd like to thank my family and friends for supporting me through the master's program here at AFIT. I would have never been able to do it without them.

Richard J. Simko

Table of Contents

Page

List of Figures

List of Tables

List of Symbols

Symbol		Page
∞	free stream subscript	16
ξ,η,ζ	curvilinear coordinates	17
δ_ξ	central difference operator in ξ direction	17
δ_η	central difference operator in η direction	17
δ_ζ	central difference operator in ζ direction	17
$\tilde{F}$	flux in ξ direction	17
$\tilde{G}$	flux in η direction	17
$\tilde{H}$	flux in ζ direction	17
l	inner Newtonian iteration	18
μ_t	eddy viscosity	21
$\|\omega\|$	magnitude of vorticity	21
l_m	mixing length	21
y^+	law-of-the-wall parameter	21
D	base diameter of carrier	26
x/D	separation distance	26

List of Abbreviations

Abbreviation		Page
B-L	Baldwin-Lomax	iv
S-A	Spalart-Allmares	iv
DES	Detached-Eddy simulation	iv
CFD	computational fluid dynamics	2
AFSEO	Air Force SEEK Eagle Office	2
RANS	Reynolds Averaged Navier-Stokes	2
LDV	laser Doppler velocimeter	14
DNS	direct numerical simulation	20
LES	large eddy simulation	20
fps	frames per second	29
PSP	pressure sensitive paint	29

Store Separations from a Supersonic Cone

I. Introduction

1.1 Motivation

The future of warfare will lead the Air Force to develop vehicles capable of high-Mach flight while maintaining a low radar cross-section. The combination of the two capabilities requires the use of internally carried stores [5]. The nature of supersonic flight will cause major complications when the time comes for a store to be released. If the store is released laterally, bay doors will have to open in an environment of high dynamic pressures and the store will have to pass through a highly energetic shear layer [22]. The resonance generated by supersonic flow past the payload bay may also lead to weapon electronics deterioration and structural fatigue [5]. Another option is an aft ejection through the wake region of the vehicle. This type of store separation should be advantageous in a sense that the store will be introduced to subsonic flow and low pressure air as it is released or ejected from the aircraft [3]. However, base flows are inherently unsteady and any adverse effects should be studied to gain an understanding of possible pitfalls to overcome. The following are concerns that have to be taken into account in order to conclude whether or not an aft ejection is a conceivable option:

1. Forces and moments on the store through the base region.
2. Pitch and yaw rates of the store upon immediate separation.
3. Drag differences on the lead vehicle and store.

Forces and moments are a concern because they are likely to fluctuate due to the unsteady, turbulent nature of a base flow. This may affect whether or not the store will be able to maintain structural integrity. Pitch and yaw rates are also important

since they will have to be within a predetermined tolerance for stability and control purposes. Drag differences are important because there is a possibility of a drafting effect occurring between the two vehicles, causing them to reconnect.

1.2 Research Goals

The current research effort is aimed towards providing a basic understanding of the flow environment a store will be introduced to when being ejected out of the base of a supersonic carrier. In order to do so, combining experimental test data and computational fluid dynamics (CFD) simulations will be necessary. Experimental research will serve as a guideline for CFD runs by validating flow physics. CFD simulations can then record data for free flight cases which experimental cases cannot duplicate due to wind tunnel effects. This data will then serve as a baseline for future research where higher fidelity modelling can be achieved.

1.3 Beggar CFD code

The Beggar CFD code is used by the Air Force SEEK Eagle Office (AFSEO) at Eglin Air Force Base, Florida. The AFSEO is the certifying authority for all weapons (conventional and nuclear) carried internally or externally on all aircraft [20]. Various researchers [20, 24, 24, 26] using the Beggar code give a good description of its capabilities. It is a chimera grid solver, capable of numerically approximating solutions to the Reynolds Average Navier-Stokes (RANS) equations, thin-layer Navier-Stokes equations, or the inviscid Euler equations via finite-volume discretization of the governing equations. The chimera grid solver has the advantage of being able to use overlapping structured grids for domain decomposition [25]. This gives Beggar the ability to perform dynamic store separation simulations. The disadvantage of using the chimera technique is the governing equations are not satisfied where there is an overlapping region between grids. For a dynamic computation, the following is a summary of Beggar's step by step operations [26]:

1. Grids are assembled using a cookie cutter process.
2. Flow governing equations are solved.
3. Viscous stresses and pressures are integrated over a body's surface to compute forces and moments.
4. Equations of motion are solved to determine the new locations of the moving bodies.

The process is then repeated. A more detailed explanation of the flow solver schemes and discretization of the governing equations is presented later.

1.4 Research Approach

Basic steps will be taken in order to understand the effects of a store in the wake flow. The first step will be to get an accurate base pressure with CFD by comparing to experimental data and analytical models. This will aid in the validation of a proper turbulence model. Once this is done, CFD runs with the store in the wake flow can be run in a free flight environment and a wind tunnel environment to quantify effects a wind tunnel imposes on the test cases. As soon as the flowfield is understood within a reasonable confidence using static solutions, initial conditions for a dynamic run can be better approximated.

1.4.1 Step 1. Turbulence Model Validation. With most CFD research comes the validations of the flow solver and schemes used. The experimental testing by Jung [16] along with store separation literature will provide insight into whether or not CFD simulations are accurately representing what would be seen in real life. Part of this validation problem lies in the inability of current flow solvers to simulate massively separated turbulent flow behind the base of an object. The Beggar CFD code incorporates the B-L, S-A and DES turbulence models. Each will be analyzed so conclusions can be drawn towards which can most accurately model the base flow during a supersonic store separation.

1.4.2 Step 2. Flowfield Validation with Store. Wind tunnel testing has been accomplished by Jung [16] using the same geometries as the current research effort. This provides experimental data to compare with in order to find quantifiable differences between free flight cases. This will then allow a continuation of experimental testing to be done in parallel with computational studies. A closer look at the wind tunnel experiments is provided in the Chapter III.

1.4.3 Step 3. Force and Moment Analysis. Dynamic separations will eventually be modelled with the Beggar CFD code. Free flight force and moment data from initial static comparisons will help provide necessary knowledge of the flowfield for preparation of dynamic store separations. Using an assumed set of inertial properties will allow ejection forces to be approximated. The force and moment analysis will also provide another way to quantify wind tunnel and sting effects compared to atmospheric CFD cases.

1.5 Previous Research

1.5.1 Supersonic Base Flow. Although not much research has been done in the past relating to the effects of a store in the near wake of a projectile, base flows in general have been studied for over a century [19]. Various researchers [12,14,15,19,21] have reported the base drag of a projectile can contribute anywhere from one-third to two-thirds of a supersonic vehicle's total drag. The Air Force is obviously interested in this area since rockets, missiles, and other supersonic projectiles make up a large part of its tactical inventory. Since base drag is the difference between the vehicle's frontal and base surface pressures acting along the streamwise axis, it's important the base pressure is modelled accurately by CFD simulations so ejection trajectories are accurate [19].

In order to fully understand the base flow region, a more comprehensive description is needed. Figure 1 provides a schematic of a supersonic vehicle's base. At the corner of the base the freestream undergoes a sharp expansion. The turbulent bound-

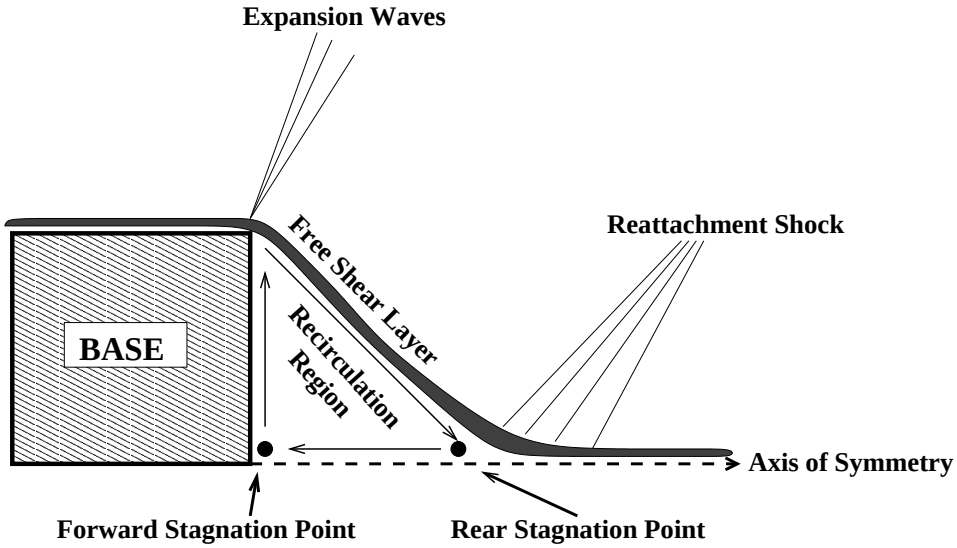

Figure 1: Overview of base flow

ary layer separates from the base and becomes a free shear layer which separates the outer inviscid flow from the inner recirculation region [7, 8, 15]. The free shear layer is characterized by having a maximum stress at its own centerline, while the outer edges have nearly no shear stresses. As the free shear layer bottlenecks down towards the axis of symmetry, recompression shocks form in order to realign the flow. The entrainment of mass from recompression causes the flow to reverse back towards the base of the cone. The velocity of this reversed flow has been recorded at 30 percent of the freestream velocity, with Mach numbers up to 0.5 [19]. The area created by the reversed flow is the recirculation region. This area has forward and rear stagnation points. The rear stagnation point marks the end of the recirculation region and the start of the turbulent trailing wake [12, 15, 21]. The size of the recirculation region is in direct correlation to the strength of the expansion waves, since it has an effect on the angle the flow will be allowed to turn. A smaller recirculation region allows the flow to turn more sharply, so there will be a stronger expansion. Since the expansion is stronger, there will be lower pressure at the base and larger base drag [13]. Base pressures are discussed in more detail later.

There is very little research available to gain a complete understanding of the effects a store will have on the base flow, and vice versa. Any wind tunnel results obtained for such cases have been viewed with skepticism since the presence of mounting interferences and wind tunnel effects influence the results. Figure 2 from Jung [16] shows a depiction of what can be expected from a qualitative standpoint if a conical

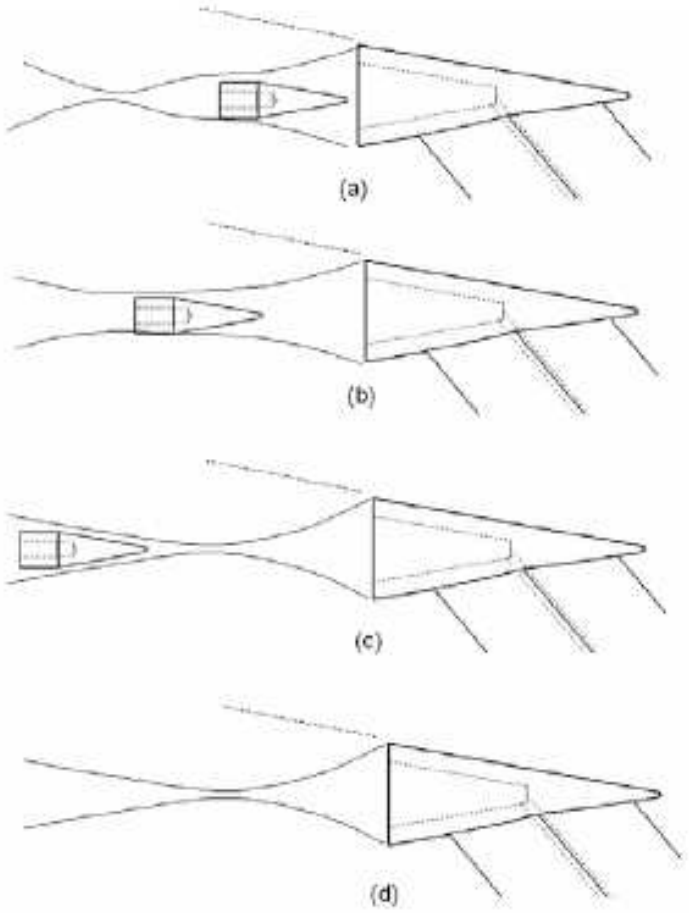

Figure 2: Graphical depiction of store in base flow

store with a cylindrical base is placed within the near wake of a supersonic conical carrier. When the store is in near the carrier's base, the shear layer reattachment will be delayed due to the presence of the store's base. At a point further downstream the shear layer edges will be pushed outward away from each other and the flow will not be allowed to come together at the axis of symmetry, reducing the strength of the

system of expansions and shocks. Next, the store will be at a point where the store no longer geometrically forces the shear layer outward. The original turning angle will once again be seen and the store's effect on the carrier should be minimal. If the ejection force is sufficient, the store will pass through the trailing wake signifying a successful separation.

1.5.2 Base Pressure. The significance of base drag can be seen in Figure 3 from Lamb and Oberkampf [19]. The accurate prediction of base pressures is

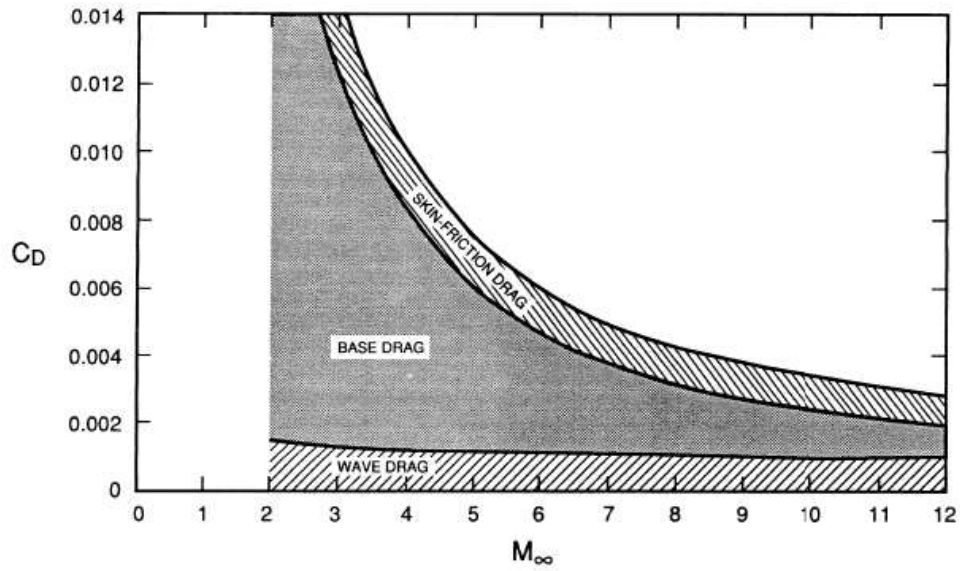

Figure 3: Components of total drag for a cone with a 2.9 degree half-angle [19]

extremely important since an accurate representation of drag is needed in order to perform a dynamic separation. There have been many different studies within the last half century related to finding accurate models of a supersonic/hypersonic vehicle's base drag. However, each study often uses different geometries or flow conditions which make finding any experimental data to compliment one's own research very difficult. Nevertheless, correlations have been made using experimental data over the years in order to have a simplified way of approximating the base pressure as a function of flow parameters and geometry.

Mach number seems to be the most influential factor in determining correlations for base pressure on supersonic projectiles [31]. Bulmer [10] produced in-flight test data for 9^o half angle cones in 1976 using Mach numbers ranging from 0.5 to 15.0. Some of his results for base pressure coefficient are shown in Figure 4. Base pressures

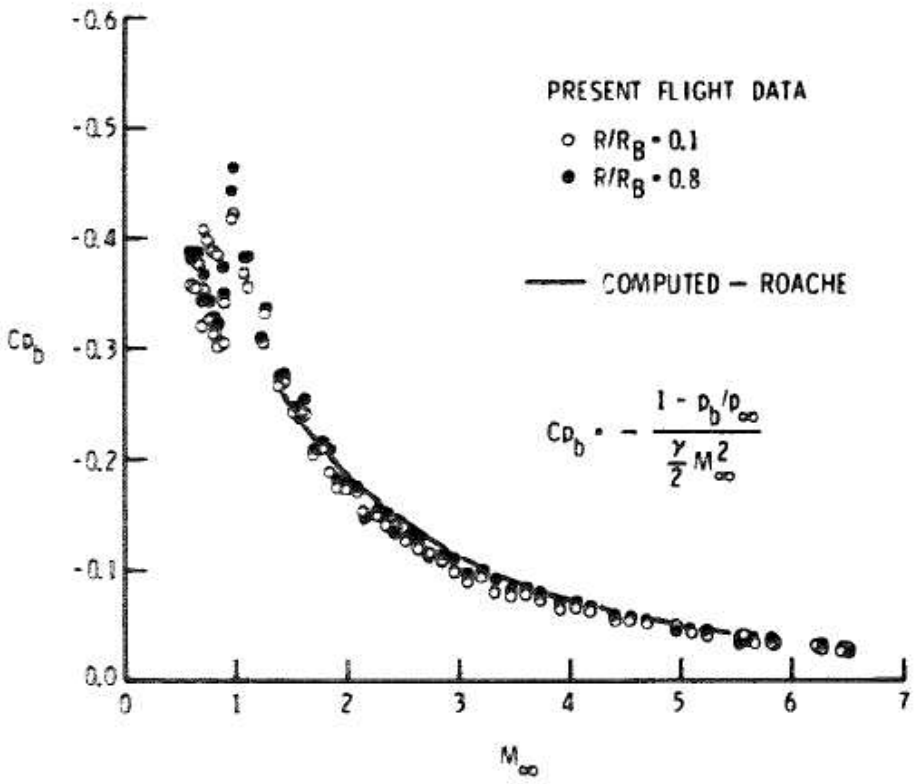

Figure 4: Base pressure coefficients as a function of Mach number [10]

were recorded at radial distances from the center of the vehicle's base (r/R) of 0.1 and 0.8. Figure 4 shows the high dependence on Mach number while also showing that at different outward radial distances from the axis of symmetry, the base pressure remains relatively unchanged. Bulmer's [10] research is also free of wind-tunnel effects so it is considered to be more accurate by other researchers of base flows.

Although Mach number is important, it alone cannot correlate all of the different factors that can change base pressure. One of the earliest studies of base pressures was done by Chapman [11] in 1951. He studied the effects of Reynolds number, length to height ratio, and boundary layer state on cones, ogives, cone-cylinders,

ogive-cylinders and wedges. One significant finding of his research showed that if a boundary layer had transitioned to turbulent before arriving at the base, the Reynolds number effect was less significant than if the boundary layer was still laminar. This can be seen by comparing Figure 5(a) to Figure 5(b). This is important for the present

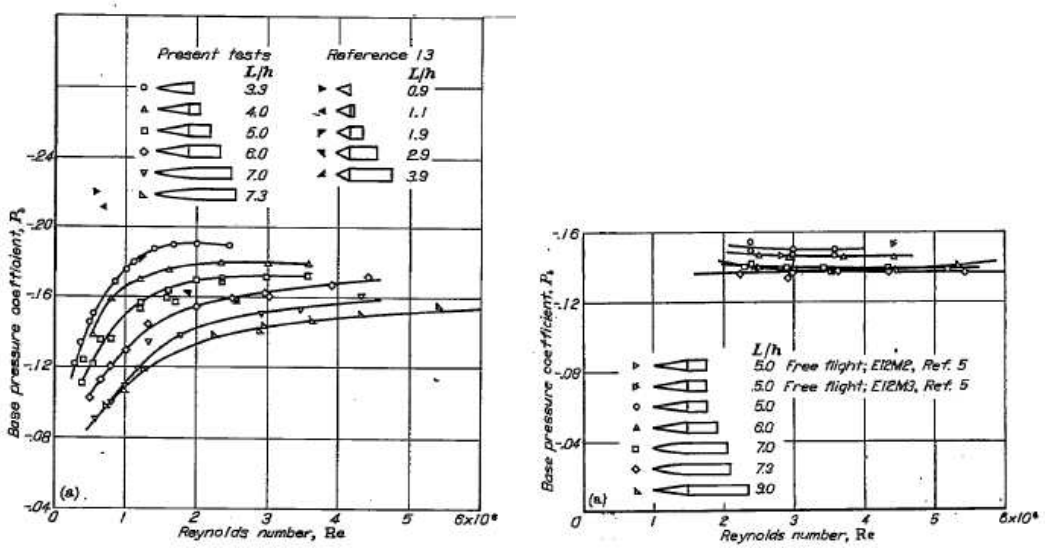

(a) Laminar (b) Turbulent

Figure 5: Variation of base pressure coefficient with Reynolds number for Mach 2.0 [11]

study since for the remainder of the research it will be assumed that the boundary layer has transitioned from laminar to turbulent since the Reynolds number based on streamwise length of the carrier was found to be $2.12 \text{x} 10^6$/m. With this in mind, a change in Reynolds number should not drastically affect the calculation of the vehicle's base drag when its boundary layer is in a turbulent state. Chapman also concluded the base pressures in laminar and turbulent cases were both a linear function of length to height ratio, with laminar cases showing less of an effect than turbulent cases.

There have been numerous empirical models for base pressure developed based on experimental research, most of which place dependence on Mach number and geometry. Lamb and Oberkampf developed such a model by taking experimental base pressure data from a number of past experiments on long cylinders and correlating to

the Crocco number, C given by

$$C = \left(1 + \frac{2}{\gamma - 1} M^{-2}\right)^{-\frac{1}{2}}, \tag{1}$$

where, γ, the ratio of specific heats, is 1.4. This parameter varies between zero and one, so it was useful to scale the large variation in Mach number (M) from all of the test data to a normalized value for correlation purposes. The correlation equation for normalized base pressure is given by

$$\frac{p_B}{p_1} = 0.05 + 0.967\left(1 - C_1^2\right) \tag{2}$$

where the subscript 1 denotes flow conditions between the conical shock and the expansion at the base. Lamb and Oberkampf then related the data for a cylinder to that of a cone by using a conversion from Bulmer's [9] work that factored in edge conditions near the base of the cone (denoted by a subscript e). After substituting back in Mach number, the final equation for normalized base pressure is shown as

$$\frac{p_B}{p_\infty} = \left(\frac{p_e}{p_\infty}\right)^2 \left[0.025 + 0.906\left(1 + \frac{\gamma - 1}{2} M_e^2\right)^{-1}\right]^J \tag{3}$$

where

$$J = \frac{1.7}{\ln\left(\frac{21}{\theta_C}\right)} \tag{4}$$

with the cone half-angle (θ_C) in degrees. For sharp cones, it has been shown that the values of the edge conditions can be assumed to be those values just after the shock using inviscid numerical solutions. These values can be obtained using the Taylor-Maccoll method [2]. The correlation for normalized base pressure is limited to θ_C's of less than 20 degrees due to lack of data available for θ_C variation. Base pressure coefficient can then be obtained using the following

$$C_{p_B} = \frac{2}{\gamma M_\infty^2}\left(\frac{p_B}{p_\infty} - 1\right) \tag{5}$$

Another method which has been more recently developed is that of van Raalte and van Oudheusden, where the base flow is considered to be two-dimensional and symmetric. They noticed that most models in the past have placed emphasis on Mach number along with some scaling term for geometry as the foundation for an equation for base pressure, ignoring Reynolds number effects. As shown previously in Chapman's testing, Reynolds number is still a major factor when dealing with laminar boundary layers entering the base flow. Van Raalte and van Oudheusden utilized a predictor-corrector method to find an equation for base pressure which took the state of the boundary layer and the Reynolds number into account. The predictor

$$C_{p_{pre}} = \frac{2}{\gamma M_\infty^2} \left\{ \left[1 + \frac{0.18\,(\gamma - 1)\,M_1^2}{1 + 0.32\,(\gamma - 1)\,M_1^2} \right]^{\frac{-\gamma}{\gamma - 1}} - 1 \right\} \tag{6}$$

is a modification of Korst's theory [18]. It uses conservation of mass in the mixing layer to obtain a base pressure as a function of Mach number alone [16]. A one-dimensional momentum equation provides a Gaussian velocity profile in the turbulent shear layer, and is solved using an integral of momentum balance. This is further simplified by considering the turbulent mixing layer to be a quasi-laminar compressible mixing layer. [31] The corrector then factors in Reynolds number effects and scaling due to the expanding boundary layer, the basis of which was found through boundary layer theory and assuming an adiabatic process. The corrector is

$$C_{p_{cor}} = A \frac{L/h}{\sqrt{\mathrm{Re}_L}} + B \tag{7}$$

where L/h is the length to base height ratio and Re_L is the Reynolds number based on the length of the cone. The coefficients A and B are:

$$\begin{aligned} A &= \left(\tfrac{14\sqrt{2}}{\gamma M^2 \pi} \right) \sqrt{\tfrac{1 + \frac{\gamma - 1}{2} M_\infty^2}{1 + \frac{\gamma - 1}{2} M_1^2}} \left(\tfrac{M_\infty}{0.015 M_1} \right) \\ B &= -\tfrac{2}{\gamma M_\infty^2} \end{aligned} \tag{8}$$

The final value of C_{p_B} can then be formulated using $C_{p_{pre}}$ and $C_{p_{cor}}$ as follows:

$$C_{p_B} = \frac{C_{p_{esc}} + C_{pB}}{2} \tag{9}$$

giving an analytical model of base pressure coefficient which takes into account Reynolds number, Mach number, scaling factors and the boundary layer state.

The two models from van Raalte and van Oudheusden, and Lamb and Oberkampf provide a quick approach for approximating base pressure. One is an empirical model based solely on Mach number, while the other is an analytical model which adds Reynolds number and geometric effects. These will allow CFD comparisons of base pressure for free flight cases presented later. The coupling of the two should yield similar approximations and a way to help validate CFD flow schemes.

Herrin and Dutton produced experimental results of the near wake flow around a cylinder in Mach 2.5 flow with a Reynolds number of 52x10^6/m at the nozzle exit of their wind tunnel. Their wind tunnel experiments are well known in the base flow community and have been used widely for CFD validation of supersonic base flows [15]. Their work is important because they document the pressure distribution along the base as well as provide insight and correlations to important flow features inside the near wake. They show the mean pressure distribution on the base of their cylinder to be fairly uniform, which is what can be expected for the current research. Figure 6 is a qualitative reproduction of the base pressure profile from Herrin and Dutton [15]. Their mean base C_p for their test setup was -0.102, using an area weighted average. Key features show the lowest base pressure towards the center of the base and the highest pressures towards the outer edges. The pressure on the outer edges was noted to be 3.9% higher than the pressure at the center [15]. Although the current research has a different geometry and flow conditions, one can expect the same type of distribution with a lower base pressure due to the larger turning angle around the base. This can be used as a general guideline when validating a turbulence model and other flow schemes.

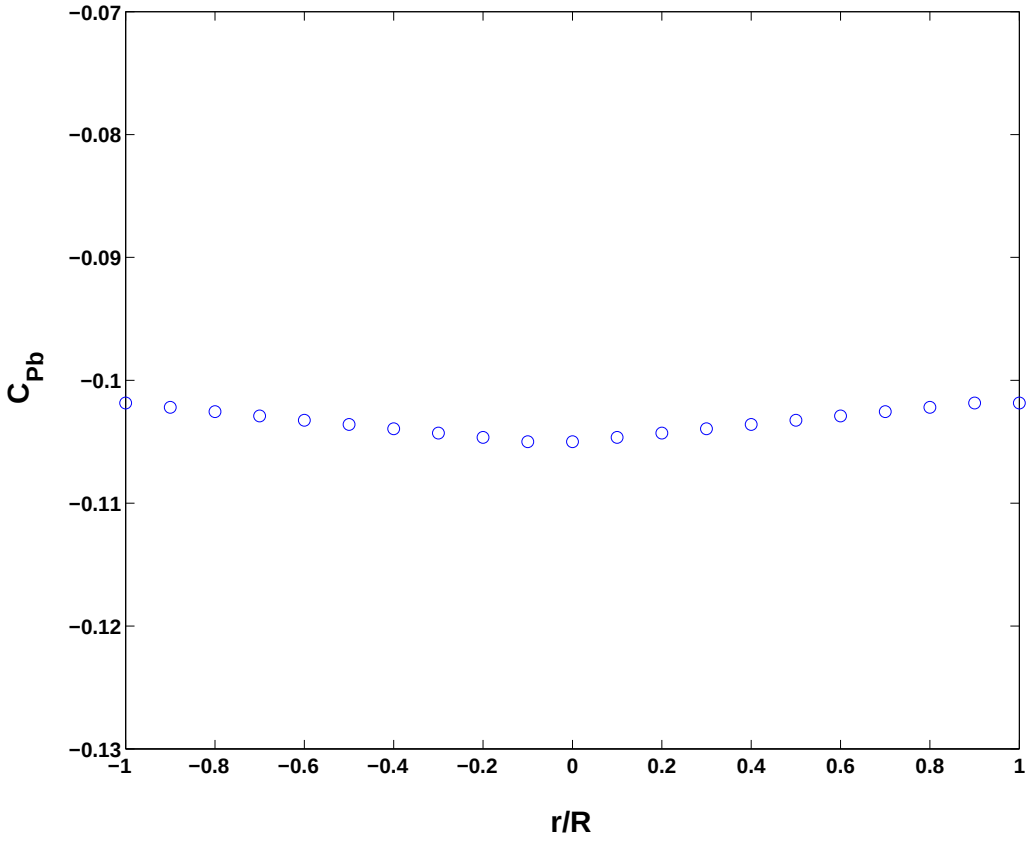

Figure 6: Herrin and Dutton base pressure profile (M = 2.5) [15]

1.5.3 Near Wake Region. Base pressure alone does not quantify all of the effects of the base region. The recirculation region and reattachment point are also important flow features since they help to define the geometry of the near wake region. As previously shown in Figure 1, a recirculation region is inherent to all supersonic base flows. The rear stagnation point defines where recirculation ends and is approximately where the flow is reattached, thus creating reattachment shocks. This is important to the current study since the store will be inserted directly through these flow features. It is also important in deciding which turbulence model to use since each will produce different recirculation velocities and reattachment points.

In addition to their studies on the base pressure distribution, Herrin and Dutton provide streamwise velocity plots along the centerline of their cylinder. Figure 7 is a

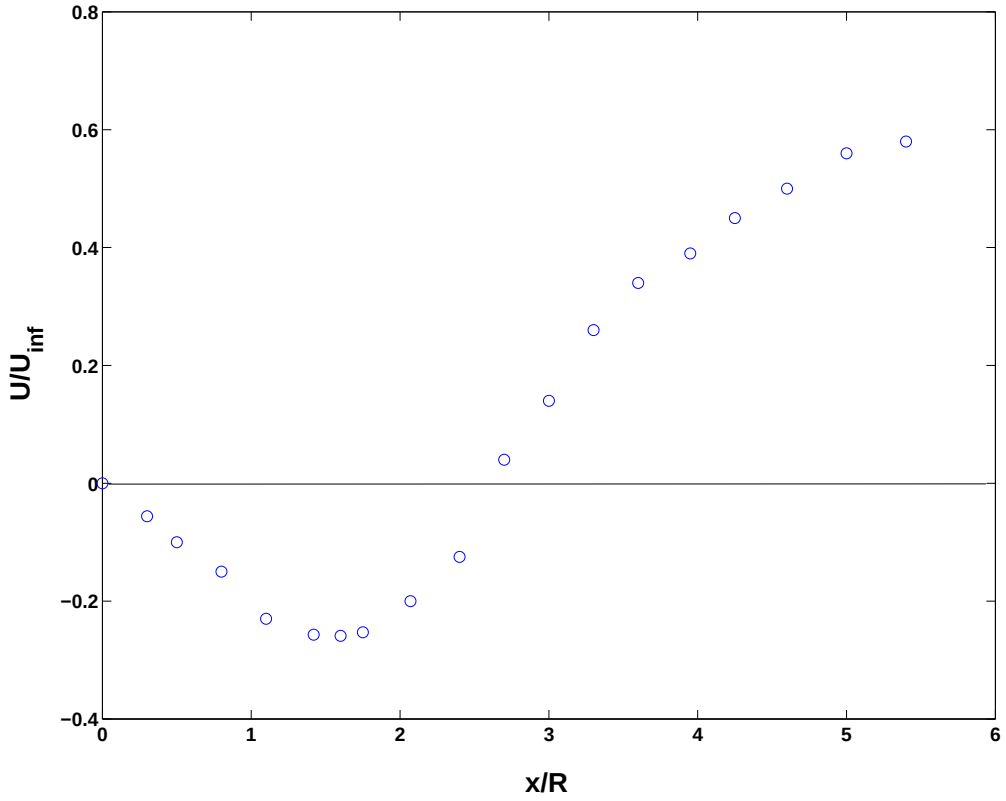

Figure 7: Herrin and Dutton streamwise velocity profile (M = 2.5) [15]

reproduction of their work. The distance along the centerline is taken from the base, and is non-dimensionalized by the radius of the cylinder (x/R). They recorded these velocities using a laser Doppler velocimeter (LDV). The recorded location of their rear stagnation point was at 2.65 x/R. Their maximum reverse velocity occurred at approximately 1.5 x/R and was 27% of the freestram velocity. With CFD, these quantities can be easily measured and compared. Again, values are expected to be different, but they present a comparison to get a good idea of what should be happening in the near wake.

II. Theory

2.1 Governing Equations

The governing equations for viscous fluid flow in three dimensions are the Navier-Stokes equations, which are based on the conservation laws of mass, momentum and energy in an arbitrary control volume [6]. The integral form in cartesian coordinates is shown to be:

$$\int_{\mathcal{V}} \frac{\partial \vec{Q}}{\partial t} d\mathcal{V} + \oint_{S} \left(\vec{F}_c - \vec{F}_v \right) dS = 0 \tag{10}$$

where $\vec{Q}$ is the vector of conserved variables, $\vec{F}_c$ is the vector of convective fluxes and $\vec{F}_v$ is the vector of viscous fluxes shown below. Convective transport quantities in the fluid are represented by $\vec{F}_c$, and viscous effects are taken into account by $\vec{F}_v$. The volume and surface area of the element are represented by $\mathcal{V}$ and S respectively [6].

$$\vec{Q} = \begin{bmatrix} \rho \\ \rho u \\ \rho v \\ \rho w \\ E_t \end{bmatrix}, \quad \vec{F}_c = \begin{bmatrix} \rho \\ \rho u V + p n_x \\ \rho v V + p n_y \\ \rho w V + p n_z \\ (E_t + p) V \end{bmatrix}, \quad \vec{F}_v = \begin{bmatrix} 0 \\ \tau_{xx} n_x + \tau_{xy} n_y + \tau_{xz} n_z \\ \tau_{yx} n_x + \tau_{yy} n_y + \tau_{yz} n_z \\ \tau_{zx} n_x + \tau_{zy} n_y + \tau_{zz} n_z \\ \Theta_x n_x + \Theta_y n_y + \Theta_z n_z \end{bmatrix} \tag{11}$$

The components of velocity in a cartesian coordinate system which make up the velocity vector, $\vec{U}$, are u,v, and w. E_t is the total energy. The density is ρ and the contravariant velocity is

$$V = \vec{U} \cdot \vec{n} \tag{12}$$

and

$$\begin{aligned} \Theta_x &= u\tau_{xx} + v\tau_{xy} + w\tau_{xz} + k\frac{\partial T}{\partial x} \\ \Theta_y &= u\tau_{yx} + v\tau_{yy} + w\tau_{yz} + k\frac{\partial T}{\partial y} \\ \Theta_z &= u\tau_{zx} + v\tau_{zy} + w\tau_{zz} + k\frac{\partial T}{\partial z} \end{aligned} \tag{13}$$

are the terms which incorporate viscous stresses and heat conduction. The thermal conductivity constant is denoted with a k, and T is the temperature. The values τ_{xx},τ_{yy},τ_{zz},τ_{xy} and τ_{xz} are components of the symmetric stress tensor $\bar{\tau}$ shown in

Equation 14

$$\bar{\tau} = \begin{bmatrix} \tau_{xx} & \tau_{xy} & \tau_{xz} \\ \tau_{yx} & \tau_{yy} & \tau_{yz} \\ \tau_{zx} & \tau_{zy} & \tau_{zz} \end{bmatrix} \tag{14}$$

which originate from analyzing a fluid element's volumetric state in a flow field. This includes the element's dilatation, rigid body rotation and shear deformation while under stress [27]. Applying Stokes' hypothesis, $\lambda + \frac{2}{3}\mu = 0$ reduces the normal viscous stresses to

$$\begin{aligned} \tau_{xx} &= 2\mu \left[\frac{\partial u}{\partial x} - \frac{1}{3} div \left(\vec{U} \right) \right] \\ \tau_{yy} &= 2\mu \left[\frac{\partial v}{\partial y} - \frac{1}{3} div \left(\vec{U} \right) \right] \\ \tau_{zz} &= 2\mu \left[\frac{\partial w}{\partial z} - \frac{1}{3} div \left(\vec{U} \right) \right] \end{aligned} \tag{15}$$

Even though Stokes' hypothesis is an educated guess, it can be accepted because it has been proven to be accurate in a large number of experiments. These equations are valid with the assumption that the fluid of interest is Newtonian and isotropic [27]. To close the system of equations, the ideal gas law is used [13].

Beggar uses non-dimensional quantities in its flow solver, but uses dimensional quantities for body-to-body and flow-to-body interactions [29]. In order to non-dimensionalize the Navier-Stokes equations, the values in Equation 11 are replaced with the following values denoted by an asterisk:

$$\begin{aligned} \rho = \rho^* \rho_\infty \qquad E_t = E_t^* \rho_\infty a_\infty^2 \qquad p = p^* \rho_\infty a_\infty^2 \\ t = t^* \frac{L_{ref}}{a_\infty} \qquad u = u^* a_\infty \qquad v = v^* a_\infty \qquad w = w^* a_\infty \end{aligned} \tag{16}$$

where ∞ subscripts denote freestream values. This non-dimensionalization provides the advantage of having normalized values when solving numerically. Also, the variance of Mach, Reynolds, and Prandtl number will be independent of one another in a flow solver that uses non-dimensional quantities [30].

In many cases the governing equations can be simplified. For example, high Reynolds number flows often exhibit thin boundary layers compared to the size of

the body of interest. In such a case, the viscous contributions can be ignored and the result is the Euler equations [6]. Although the research presented in this study does meet the criteria for high Reynolds number, fully viscous equations of motion were used in Beggar due to the inability of the inviscid solver to calculate a solution near the abrupt turning of the flow at the base of the conical geometries. Also,a shear layer is an important flow feature for this research which cannot be computed with an inviscid solver.

2.2 Discretization and Solver Schemes

Since there is no exact solution to the Navier-Stokes equations, time and space must be discretized so that the solution can be numerically integrated. Rizk et al [26] have a detailed formulation of how this was implemented into the Beggar code. Physical space is discretized using finite volumes while time is discretized into intervals. Once discretized, physical coordinates (x,y,z) are represented in the computational domain as body fitted curvilinear coordinates (ξ,η,ζ), which bound volumes that contain discretized flow variables. If i,j,k are cell indices in the ξ,η,ζ coordinate system, the discretized equations using the first order Euler implicit time discretization are

$$J_{i,j,k}\left(\frac{\Delta\vec{Q}}{\Delta t}\right)^{n+1}_{i,j,k} + R^{n+1}_{i,j,k} = 0 \tag{17}$$

where

$$R^{n+1}_{i,j,k} = \left[\delta_\xi \tilde{F} + \delta_\eta \tilde{G} + \delta_\zeta \tilde{H}\right]^{n+1}_{i,j,k} \tag{18}$$

and the central difference operators δ_ξ, δ_η and δ_ζ operate on the fluxes ($\tilde{F}$, $\tilde{G}$, $\tilde{H}$) for the curvilinear coordinates obtained using the Steger-Warming scheme discussed later. The incremental vector of conserved variables is ΔQ. The incremental time is Δt and $J_{i,j,k}$ represents the curvilinear cell volume at an i,j,k coordinate. Using

Newton's method to iterate through time leads to

$$\hat{J}\frac{\Delta\hat{Q}^{n+1,m+1}}{(\Delta T^{n+1,m})} + \left[\left(\frac{\partial\hat{R}}{\partial\hat{Q}}\right)^{n+1,m}\Delta\hat{Q}^{n+1,m+1} + \left(\frac{\partial\hat{R}}{\partial\bar{Q}}\right)^{n+1,m}\Delta\bar{Q}^{n+1,m+1}\right] = \\ -\left[\hat{J}\frac{\left(\hat{Q}^{n+1,m}-\Delta\hat{Q}^{n}\right)}{\Delta t} + \hat{R}^{n+1,m}\right] \tag{19}$$

which are the flow governing equations for an individual grid for all cells where

$$\hat{R}^{n+1,m} = \hat{R}\left(\hat{Q}^{n+1,m}, \bar{Q}^{n+1,m}, \tilde{Q}^{n+1,m}\right) \tag{20}$$

and the m superscript denotes the number of Newton iterations. The vectors $\hat{R}$, $\hat{Q}$ and $\Delta\hat{Q}$ are values which are updated by solving the governing equations. The vectors $\Delta\bar{Q}$ and $\bar{Q}$ are updated by boundary conditions ("phantom or ghost cells") and $\tilde{Q}$ is a vector which refers to flow values in interpolated cells that contain solutions from overlapping grids. Phantom cells that are within an interpolated region are kept constant through a Newton iteration. The diagonal matrix $\hat{J}$ contains the cell volumes and the diagonal matrix ΔT is used to replace the fixed time step with a variable time step in the subsequent iterations. The incremental solution for the next Newton iteration ($\Delta\hat{Q}^{n+1,m+1}$) is found by applying the symmetric Gauss-Seidel relaxation scheme to equation 19, which yields

$$\left[l^{n+1,m} + (1-\Phi)D^{n+1,m}\right]\Delta\hat{Q}^{n+1,m+1,l+1/2} + \left(\Phi D^{n+1,m} + u^{n+1,m}\right)\Delta\hat{Q}^{n+1,m+1,l+\Phi} = \\ -\left[\hat{J}\frac{\hat{Q}^{n+1,m}-\hat{Q}^{n}}{\Delta t} + \hat{R}^{n+1,m}\right] - \left(\frac{\partial\hat{R}}{\partial\bar{Q}}\right)^{n+1,m}\Delta\bar{Q}^{n+1,m+1,l} \tag{21}$$

where the number of inner iterations is l. When $\Phi = 1$ the inner iteration will do a forward sweep and when $\Phi = 0$ will perform a backwards sweep. The variables $l^{n+1,m}$, $\bar{D}^{n+1,m}$ and $\bar{U}^{n+1,m}$ are lower, block and upper diagonal matrices which split $\Delta\hat{Q}^{n+1,m+1}$ into coefficients. For each inner iteration, boundary conditions are applied explicitly and then implicitly at convergence of the inner iterations [26].

2.2.1 Steger-Warming Scheme. The Steger-Warming scheme is a flux-vector splitting scheme. This type of scheme uses upwinding to distinguish wave propagations in both directions, so it is one of the more advanced spatial discretization techniques [6]. Its formulation is based on dividing the vector of convective fluxes into positive and negative contributions shown as

$$\vec{F_c} = \vec{F_c^+} + \vec{F_c^-} \tag{22}$$

where the fluxes are defined by

$$\begin{aligned} \vec{F_c^\pm} &= \bar{A}_{SW}^{\pm} \vec{Q} = \left(\bar{M} \bar{\Lambda}^{\pm} \bar{M}^{-1}\right) \vec{Q} \\ \bar{\Lambda}^{\pm} &= \tfrac{1}{2}\left(\bar{\Lambda}_c \pm \left|\bar{\Lambda}_c\right|\right) \end{aligned} \tag{23}$$

and

$$\bar{\Lambda}_c = \begin{bmatrix} \Lambda_1 & 0 & 0 & 0 \\ 0 & \Lambda_2 & 0 & 0 \\ 0 & 0 & \Lambda_3 & 0 \\ 0 & 0 & 0 & \Lambda_4 \end{bmatrix} \tag{24}$$

is the diagonal matrix containing the real eigenvalues Λ_i [6]. There are other discretization methods available in Beggar, such as Roe's method, but the Steger-Warming scheme is the only one used in the current research.

2.3 Turbulence Models

In turbulent flows, air molecules move in a completely random nature which causes mixing of the various fluid layers. This mixing can be highly energetic, increasing momentum and energy between other molecules and boundaries which increase skin friction values and heat transfer [6]. This phenomenon is viscous in nature and occurs at high Reynolds numbers. This is important for this research since supersonic base flows are inherently highly turbulent with high Reynolds numbers.

The Navier-Stokes equations can resolve turbulence at all scales, however the current computational capabilities required to do so are not available for High-Reynolds number flows [23]. This approach to CFD is called direct numerical simulation (DNS). According to Blazek, the number of grid points needed for DNS spatial resolution is proportional to $\mathrm{Re}^{9/4}$ and the cpu time is proportional to Re^3, therefor instead of simulating turbulence directly it has to be modelled instead. The different types of modelling approaches are based on capturing different scales of turbulence. These turbulent disturbances are three-dimensional and are referred to as eddies. Large eddy simulations (LES) are the next step down from DNS, simulating the large eddy structures while the turbulence occurring at smaller scales is modelled. Reynolds Averaged Navier-Stokes turbulence models attempt to model all turbulence scales using a single length scale. RANS models are the most basic. In between RANS and LES are hybrid RANS/LES models which do exactly what their name implies [23]. Figure 8 from Nichols [23] gives a visual representation of the turbulence spectrum and what the different types of turbulence approaches model. There are a number of different models within these subcategories that have been developed over the years. The three different turbulence models compared in this research were Baldwin-Lomax,

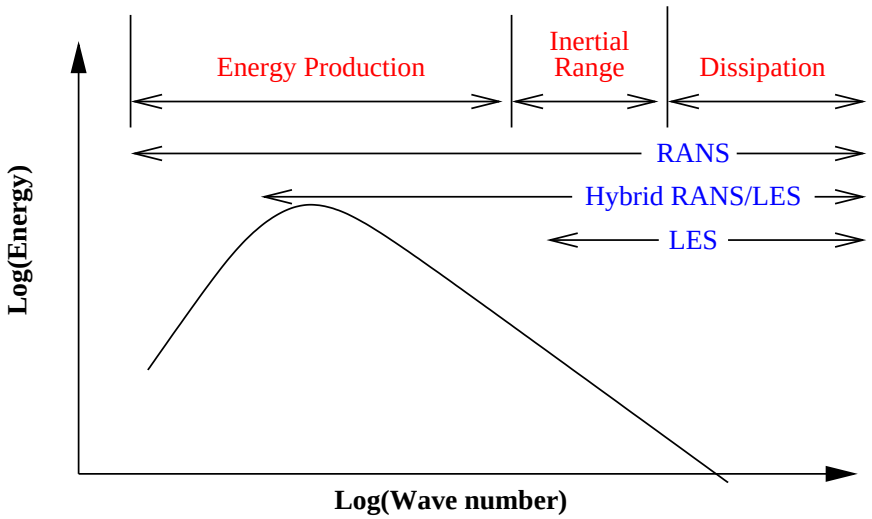

Figure 8: Region of turbulent energy spectrum modelled by different turbulence model approaches [23]

Spalart-Allmaras and Detached Eddy Simulation. Each of these are discussed in more detail.

2.3.1 Baldwin-Lomax. The B-L turbulence model is an algebraic model. Algebraic models are also referred to as zero equation models because they do not include any partial differential equations to compute the Reynolds stresses [32]. The B-L model is based on Prandtl's mixing length hypothesis, where the effects of turbulence are modelled through the eddy viscosity μ_t [4]. This coefficient is separated into an inner and outer formulation by dividing a turbulent boundary layer into an inner and outer region [23]. The inner region formulation for the eddy viscosity coefficient is

$$(\mu_t)_{inner} = \rho l_m^2 \left|\omega\right| \tag{25}$$

where $|\omega|$ is the magnitude of vorticity

$$\left|\omega\right| = \sqrt{\left(\frac{\partial u}{\partial y} - \frac{\partial v}{\partial x}\right)^2 + \left(\frac{\partial v}{\partial z} - \frac{\partial w}{\partial y}\right)^2 \left(\frac{\partial w}{\partial x} - \frac{\partial u}{\partial z}\right)^2} \tag{26}$$

and l_m is the mixing length

$$l_m = \kappa y_{wall} \left[1 - e^{\frac{-y^+}{A^+}}\right] \tag{27}$$

The law-of-the-wall parameter, y^+, is

$$y^+ = \frac{\rho_w u_\tau y_{wall}}{\mu_w} \tag{28}$$

where the subscript w represents conditions at the wall, y_{wall} is the distance away from the wall and

$$u_\tau = \sqrt{\frac{\tau_w}{\rho_w}} \tag{29}$$

is the friction velocity. The outer region formulation for eddy viscosity is

$$(\mu_t)_{outer} = \rho K C_{CP} F_{wake} F_{kleb} \tag{30}$$

where

$$F_{wake} = \min \left\{ y_{\max} F_{\max}, C_{wk} y_{\max} \frac{U_{diff}^2}{F_{\max}} \right\} \tag{31}$$

$F_{\max}$ and $y_{\max}$ are the maximum quantities from

$$F(y) = y_{wall} \left| \omega \right| \left(1 - e^{\frac{-y^+}{A^+}} \right) \tag{32}$$

and U_{diff} is the difference between the maximum and minimum velocities in the profile. F_{kleb}, is the Klebanoff intermittency factor

$$F_{kleb} = \left[1 + 5.5 \left(\frac{C_{kleb}}{y_{\max}} \right)^6 \right]^{-1} \tag{33}$$

Values for various constants are

$$\begin{aligned} A^+ &= 26, \quad C_{CP} = 1.6\,, \quad C_{kleb} = 0.3 \\ C_{wk} &= 0.25, \quad \kappa = 0.4, \quad K = 0.0168 \end{aligned}$$

The B-L turbulence model is useful when applied to problems that are characterized by a single length scale such as attached boundary layers. However, major shortcomings of the B-L model include a lack of turbulent transport terms and a tendency to switch between F_{max} values in complex flows that contain multiple shear layers [23]. Wilcox [32] comments that the B-L turbulence model is completely unreliable for separated flows, which describes the conditions in the wake of a high-Mach projectile. The model will be implemented, studied and compared because of its simplicity and because it is supposed to be computationally forgiving.

2.3.2 Spalart-Allmaras. The Spalart-Allmaras (S-A) turbulence model includes a transport equation for turbulent viscosity, making it a one equation model. According to Spalart and Allmaras, the model is based on empiricism, dimensional analysis, Galilean invariance and selective dependence of molecular viscosity [28]. The turbulence variable $\tilde{v}$ is used in the standard S-A equation and has dimensions of viscosity, and the eddy viscosity is $\nu_t = \tilde{\nu} f_{v1}$ [23]. The S-A model equation is

$$\frac{\partial \tilde{\nu}}{\partial t} + \vec{U}_i \frac{\partial \tilde{\nu}}{\partial x_i} = \frac{1}{\sigma} \left\{ \nabla \cdot \left[(\nu + \tilde{\nu}) \nabla \tilde{\nu} \right] + C_{b2} \left(\nabla \tilde{\nu} \right)^2 \right\} + P\left(\tilde{\nu}\right) - D\left(\tilde{\nu}\right) \tag{34}$$

where production term $P(\tilde{\nu})$ and destruction term $D(\tilde{\nu})$ are given by

$$P(\tilde{\nu}) = C_{b1} \left(|\omega| + \frac{\tilde{\nu}}{\kappa^2 d^2} f_{v2} \right) \qquad D(\tilde{\nu}) = C_{w1} f_w \left(\frac{\tilde{\nu}}{d} \right)^2 \tag{35}$$

with d being the distance from the nearest wall. The following set of functions completes the system

$$f_{v2} = 1 - \frac{\chi}{1 + \chi f_{v1}} \tag{36}$$

$$f_w = g \left(\frac{1 + C_{w3}^6}{g^6 + C_{w3}^6} \right)^{\frac{1}{6}} \tag{37}$$

$$f_{v1} = \frac{\chi^3}{\chi^3 + C_{v1}^3} \tag{38}$$

$$g = r + C_{w2} \left(r^6 - r \right) \tag{39}$$

$$r = \frac{\tilde{\nu}}{\left(|\omega| \, \kappa^2 d^2 + \tilde{\nu} f_{v2} \right)} \tag{40}$$

with the following constants

$$\begin{aligned} C_{b1} &= 0.1355, \;\; \sigma = 2/3 \, , \;\; C_{b2} = 0.622 \\ C_{w1} &= C_{b1}/\kappa^2 + (1 + C_{b2})/\sigma, \;\; \kappa = 0.41 \\ C_{w2} &= 0.3, \;\; C_{v1} = 7.1 \end{aligned}$$

The S-A turbulence model has shown to be capable of making realistic predictions of shear flows, with the exception of jet like flows [32]. One drawback commented on by Nichols [23] is S-A tends to overdamp some unsteady flows. This could be an issue since base flows are inherently unsteady. However, S-A should be better suited than B-L for separated flows. Overall, S-A is a widely used model because of its numerical stability and ease of implementation on both structured and unstructured grids and will be included in studies for this research.

2.3.3 Detached-Eddy Simulation. Detached-Eddy Simulation (DES) is another turbulence model that will be used for this study. It is based on S-A, but is modified to use the best parts of RANS and LES turbulence models. On one hand, RANS does a good job with attached boundary layers and has low grid resolution requirements, while LES models separated flows more accurately but has a high requirement for grid resolution in the streamwise direction [13].

Each piece of DES should be explained in more detail. The RANS approach takes the basic flow variables and breaks them into mean and fluctuating parts. After inserting them back into the Navier-Stokes equations and performing ensemble averaging, the basic structure of the Navier-Stokes equations is maintained with the exception of two additional terms. One adds transport terms to the viscous stress tensor. The other adds a vector of turbulent heat flux to the energy equation [6]. LES, on the other hand, approaches turbulence modelling from the vantage point of resolving large eddies accurately and using subgrid-scale models to approximate the smaller scales [13]. The LES approach is based on observations that Large eddies transport more turbulent energy so they should not be modelled. The small scale eddies tend to be easier to model since they posses easily discernable traits compared to large-scale eddies [6].

The DES model is formed by modifying the wall destruction term of the S-A model (equation 35). The wall distance d is replace with $\tilde{d}$, given by

$$\tilde{d} = \min(d, C_{DES}\Delta) \tag{41}$$

where d is the distance to the nearest wall, Δ is the grid spacing and C_{DES} is 0.65 for structured grids. If $d \ll \Delta$ the model acts like a RANS model and if $d \gg \Delta$ the model acts like a Smagorinski LES model. This means one can refine the grid spacing in areas of interest to switch to the LES model [13].

III. Methodology

3.1 Geometries

The geometries for the carrier and store are generic and do not represent any specific vehicles or payloads. The carrier geometry is a cone with a spherical nose, hollowed out to fit the store within. A solid carrier was also examined. The store is conically shaped with a spherical nose and a cylindrical aft section. Figure 9 shows the geometry for both the carrier and store. All values are non-dimensionalized by the carrier vehicle's base diameter (D = 21.75 mm). The positive x-axis is defined as going in the direction of the free-stream, while the y-axis is out of the top of the wind tunnel and the z-axis is coming out of the side when one is viewing the flow going from left to right down the positive x-axis. This should not be important for atmospheric flight cases since the conical flow should be symmetric at zero degree angle of attack. However, the wind tunnel cases with the sting present should show asymmetric effects. The tips of both vehicles are spherical with diameters of 0.046 units (1/2 mm radius). All cases for CFD were run at separation distances (x/D) of

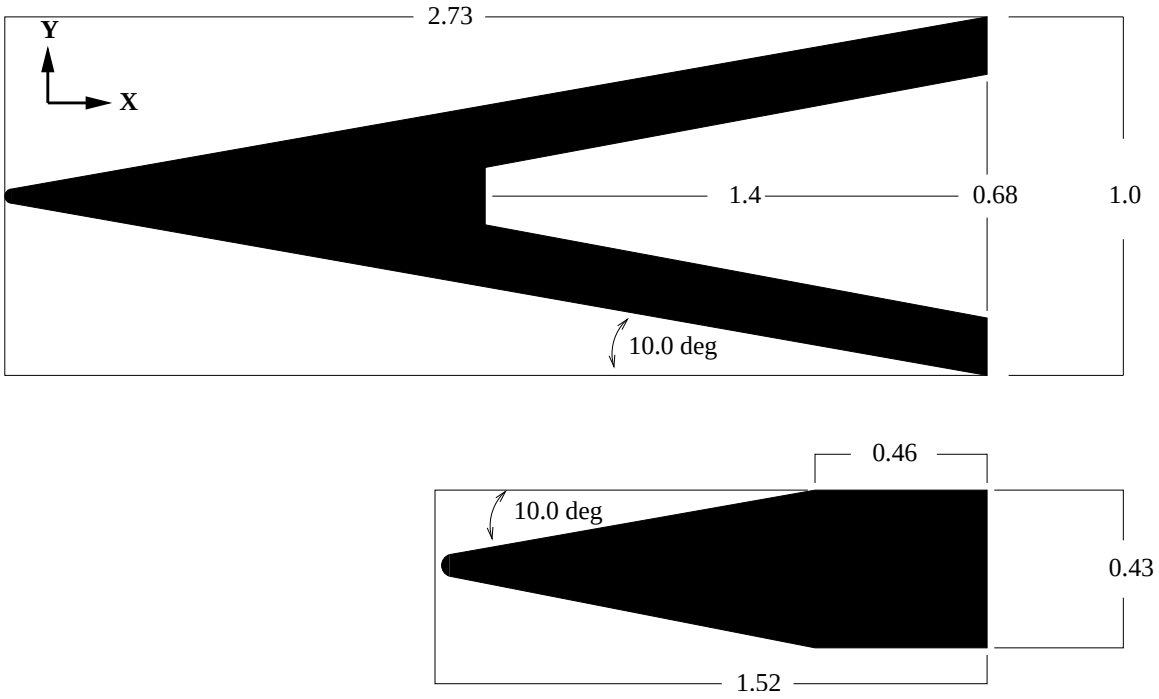

Figure 9: Carrier (top) and store (bottom) non-dimensionalized

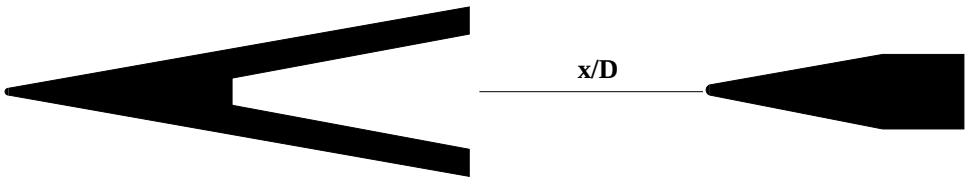

Figure 10: Separation distance (x/D)

either 0.22, 0.92 or 2.23 units between the base of the carrier and nose of the store as shown in Figure 10. Experimental cases by Jung were run at the same separation distances, however additional data was taken at 0.0, 0.46, 1.5, and 2.9 x/D.

Wind tunnel simulations included a sting. Its geometry is shown in Figure 11. Sting dimensions are non-dimensionalized by the base diameter of the carrier model. The sting is swept back 40^o from vertical and has a 9^o half-angle from the centerline. The rationale for this sting design was that a swept back sting would allow the flow interrupted by the sting at the attachment point time to return to conical flow by the time it reaches the base. The shape of the sting was chosen to be a symmetric diamond (instead of a rod or other shapes) because it should allow the flow to return to near free stream conditions. Its size was driven in part by the the hollow portion

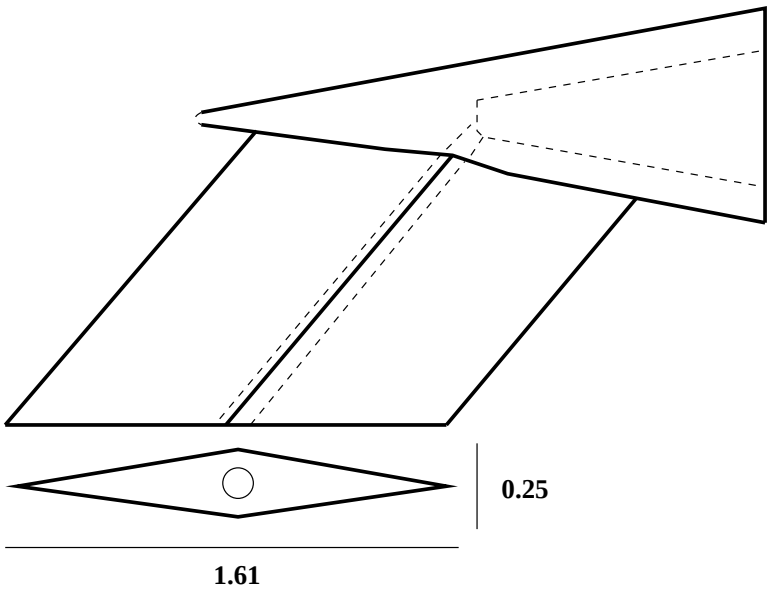

Figure 11: Sting setup [16]

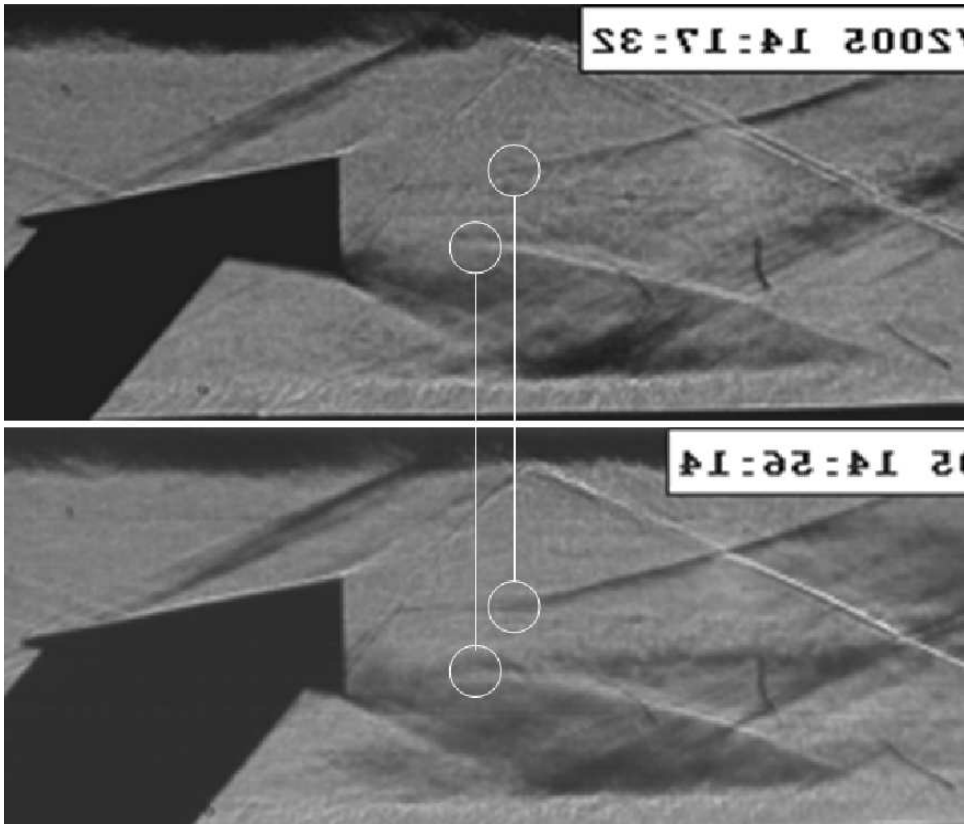

Figure 12: Schlieren images of diamond strut effects [16]

used to obtain pressure data. Jung conducted studies on the effects of varying the half-angle of the diamond as well as its length. The experiments showed that the shape of the sting had little effect, albeit detectable, on the reattachment point in the trailing wake, and a minimal effect on the overall shape of the base flow region [16]. Figure 12 provided by Jung [16] gives a visual comparison of the base flow using schlieren images.

3.2 Experimental Methodologies

Explanation of the wind tunnel environment and methodologies used by Jung [16] is necessary in order to compare to experimental results. The wind tunnel used was a supersonic blow-down tunnel, which utilizes a converging-diverging nozzle and a variable area diffuser for a range of Mach numbers. With a nominal stagnation pressure of 38 psi, the tunnel had a freestream static pressure of 1.17 psi and a test

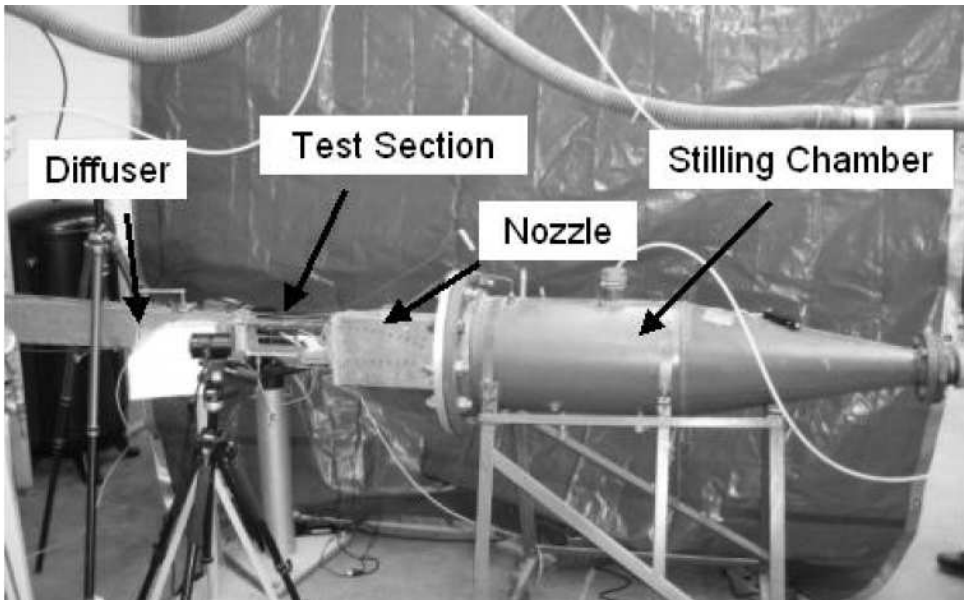

Figure 13: AFIT supersonic wind tunnel [16]

section static temperature of 110 degrees Kelvin. This yielded a wind tunnel free stream Mach number of 2.93 and a Reynolds number of $3.9 \text{x} 10^8$/m [16]. The wind tunnel has a square cross-section of 2.5 inches on a side. A picture of the tunnel is shown in Figure 13. The primary goal of the experimental research conducted by Jung was not to accurately predict a store separation, but rather to investigate and quantify effects the wind tunnel and sting were having on the flow physics of the current problem. Real-time sequences of Schlieren images were used for visual evidence of the base flow region. The Schlieren system took pictures using an exposure time of 1 μs at 20,100 frames per second (fps) for larger images and 94,500 fps for smaller images. Filtering and binning were not used. A power spectrum density study was then performed using the schlieren imaging system to analyze and record frequency data and related Strouhal numbers during the experiments [16].

Pressure sensitive paint (PSP) was also used in experimental testing. It enabled pressure data to be captured from the carrier and store to compare with analytical models and past experiments. The theory behind PSP is certain materials will fluoresce inversely proportional to pressure. Molecules within the PSP are excited to a

higher energy state by photons from a light source and get back down to their original state by either fluorescing at the visible wavelength or through oxygen quenching [16]. Oxygen quenching is the process by which oxygen molecules absorb energy from excited molecules via the oxygen molecule's vibrational mode. The higher the pressure, the more oxygen molecules are present to absorb energy from excited molecules. This limits the amount of luminescence from the PSP by giving excited molecules a higher chance to return to their original energy state through oxygen quenching. In order to capture this, a detector is used in conjunction with the light source and PSP. The PSP Jung [16] used was from Innovative Scientific Solutions, Inc, which had a pressure sensitivity of approximately 6 percent per psig at 1 atm and a response time of 0.3 s. The response time is too large to take into account any high frequency pressure changes, so all PSP data is assumed to be time averaged.

Pressure transducers were also mounted in the carrier cavity and on the outside of the store. Pressure data was sampled at 200 kHz for a half second. The transducers were used to capture differences on the store and in the carrier due to the presence of the store and to verify pressure data from the PSP system.

Notable conclusions drawn from experimental research are as follows [16]:

1. The diamond strut caused the reattachment shock to move closer to the base
2. The interaction of the conical shock from the carrier and oblique shock from the sting created a vertical pressure gradient causing asymmetric effects in the wake region.
3. The store caused the base pressure on the carrier to rise as it was moved aft, where maximum effect was noted at a distance approximately equal to half of the carrier vehicle's base diameter.
4. The cavity present in the carrier lowered its base pressure

3.3 Computational Methodologies

Beggar uses blocked, patched, and overlapping grids to compute solutions around complex dynamic geometries. From an efficiency standpoint, the grid assembly process is simplified greatly if grids made for a common rigid object are not overlapping. In Beggar, a collection of non-overlapping grids is called a superblock [1]. For a better understanding of the various superblocks and how they interact with each other, refer to Figure 14. Three main groups of grids are used–background grids (in red), grids

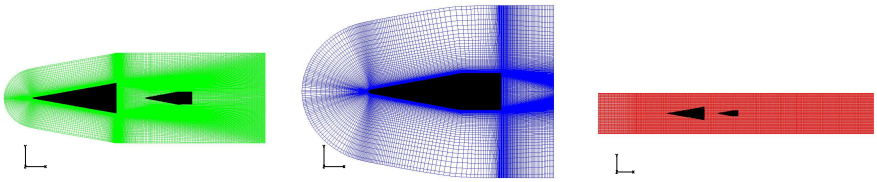

(a) Carrier superblock

(b) Store superblock

(c) Wind tunnel superblock

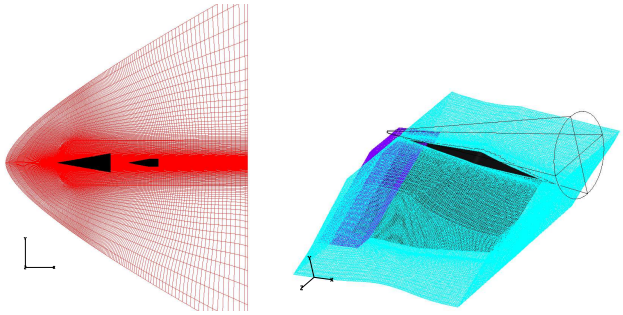

(d) Atmosphere superblock

(e) Sting and interface superblocks

Figure 14: Various superblocks

around the carrier (in green), and grids around the ejected store (in dark blue). The two remaining grids used were the interface mesh (in purple) and the mesh around the sting (in light blue). In general, an interface grid is a grid used to patch together superblocks that don't have enough cells overlapping to make an accurate interpolation during the cutting process. During CFD simulations of the experimental environment, the sting grid and background grid did not have enough cells overlapping in the front

near the carrier nose, so the interface mesh was used. For the store and carrier grids, a "C-O" topology was used, while the wind tunnel grid and interface grid were both cartesian meshes. The background grid for the free flight cases also used a "C-O" topology and the sting grid used an "H-H" topology.

There were many variations of the store/carrier in different background environments. Table 1 shows the different grid cell counts. The carrier grids with a cavity did not change the number of cells for the carrier in a significant way to differentiate between the two. Once the grids were overset, the minimum amount of cells

Table 1: Cell count for superblocks (millions)

Carrier	Store	Sting	Interface	Wind-Tunnel	Atmosphere
2.5-3.1	1.6	0.7	0.14	2.2	1.6

contained per CFD run was 5.7 million cells (atmospheric) and 7.74 million cells for the wind-tunnel with sting case. Initial grid spacing for the carrier and the store was found to be $1.4\text{x}10^{-4}$ and $2.1\text{x}10^{-4}$ respectively (non-dimensional) using a y^+ of 1. The grid stretching factor for grid growth normal to the frontal surface of each vehicle was 1.25. Carrier and store grids were revolved with equal spacing around the axis of symmetry, dividing the entire 360 degree rotation into 4 blocks, each with 25 equally spaced points along the circumference. Carrier grids with a sting attached used 40 grid points along each lower quarter revolution to allow the sting to be properly attached during the oversetting process. This is why the carrier grid cell count varies from 2.5 to 3.1 million cells in Table 1.

As previously mentioned in Chapter 2, the viscous Navier-Stokes equations were implemented by the flow solver. Mach number and Reynolds number were set to match the conditions in the experimental wind tunnel. Once initialized, the flow solver was set to calculate time accurate data starting at a non-dimensional dt of $1\text{x}10^{-4}$ and ramping up an order of magnitude every 200 iterations until the non-dimensional dt reached 1.0 ($2.54\text{x}10^{-4}$ seconds of physical time). Once this was accomplished, the solver was run from 4000 to 8000 iterations to get a solution (approximately 1 to 2

seconds total). Force and moment data were recorded every time step and used to determine when the flow was fully developed by observing the point at which oscillatory values had become stationary over time. This was done for all x/D distances and turbulence models. Data was taken from both the store and carrier, with variations of the carrier being hollow and solid.

IV. Results

4.1 Free Flight - No Store

The carrier in free flight will be used to compare against wind tunnel and sting effects. It will also give an idea of turbulence model accuracies since no other disturbances can be the cause of inaccurate data. Figure 15 shows the carrier in free flight using contours of Mach and DES as the turbulence model. Comparisons with

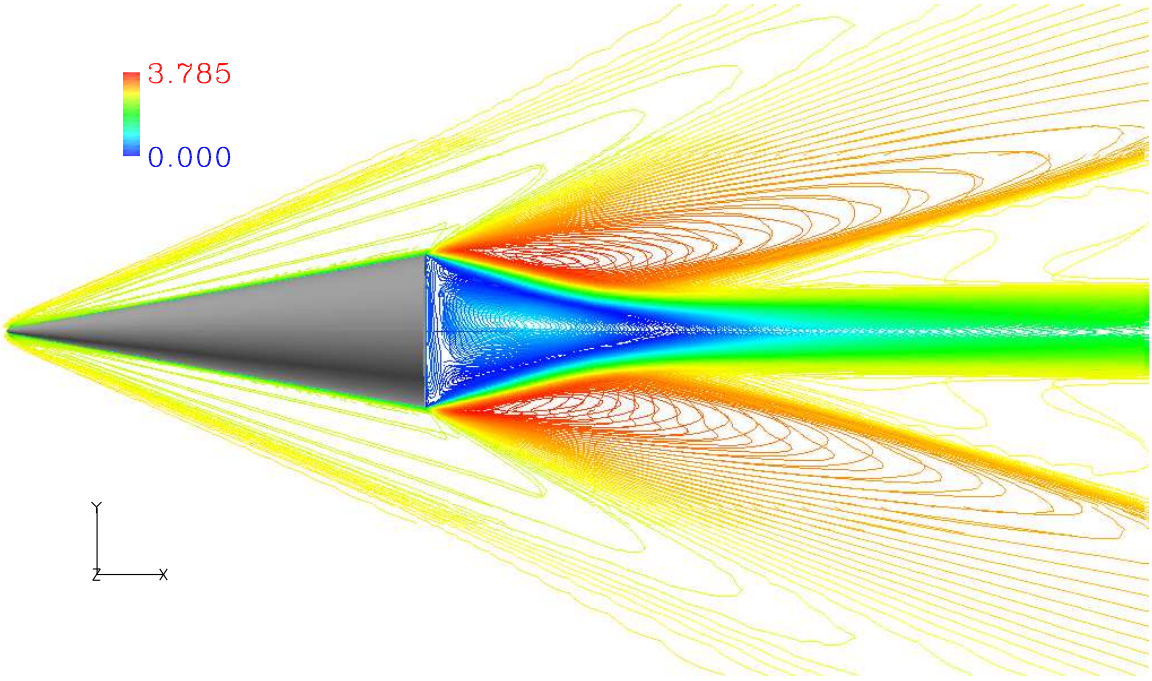

Figure 15: Contours of mach for carrier in free flight, Mach = 2.93

B-L and DES will be presented in a more quantifiable way using data from the near wake. For the remainder of the results presented in this chapter, all flow variables presented have been averaged out to at least a half second of physical time unless specified otherwise.

4.1.1 Base Pressures in Free Flight. Initial runs using all of the turbulence models for a free flight CFD case will give a general idea of the accuracy of each model when predicting base pressure without wind tunnel or mounting effects. The carrier vehicle's base pressure coefficients will be compared to the empirical and analytical models reviewed earlier for accuracy, as well as the work from Herrin and Dutton for

consistency. CFD plots of C_{p_B} are shown with empirical and theoretical values in Figure 16. The plots were taken from both horizontal and vertical strips of data from

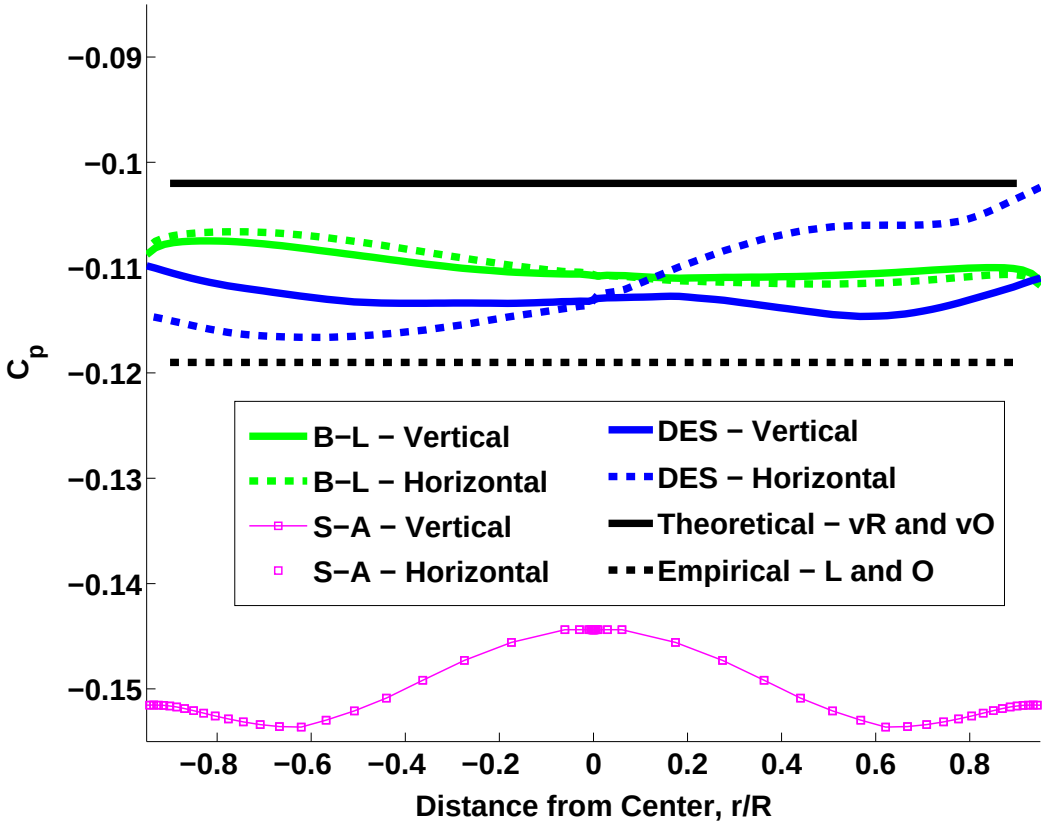

Figure 16: Base pressure coefficients on carrier in free flight compared to theoretical and empirical values

the carrier vehicle's base, as Jung [16] did in his experimentations. Computations for the theoretical and empirical models required an inviscid approximation of certain flow parameters immediately following the conical shock, which were obtained using the Taylor-Maccoll method for cones. The Mach number aft of the shock was computed as 2.651 and the pressure across the shock was 1.53. The Lamb and Oberkampf empirical model estimated a C_{p_B} of -0.119 using equations 3, 4 and 5. The van Raalte and van Oudheusden analytical model estimated a base pressure of -0.102 using Equations 6 through 9 ($Re_L = 2.12\text{x}10^6$).

As one can see, the base pressures for B-L and DES fall between the predicted values. S-A base pressures were by far the least accurate of the three turbulence models when comparing against empirical and analytical results. The S-A model computed exactly the same mean pressure distribution horizontally and vertically, showing no traces of randomness. In results obtained by Kawai and Fujii for supersonic base flow over a cylinder, the pressure distribution they compute for S-A has the same shape as the current research shows. This is apparently a common phenomenon for RANS turbulence models on supersonic base flows [17]. An explanation of this in S-A can be related to its tendency to over-damp unsteady solutions [23]. Figure 17 shows further evidence of the dissipative nature of S-A in unsteady flows as the time history of x force coefficients on the carrier reveals the S-A case has reached steady state.

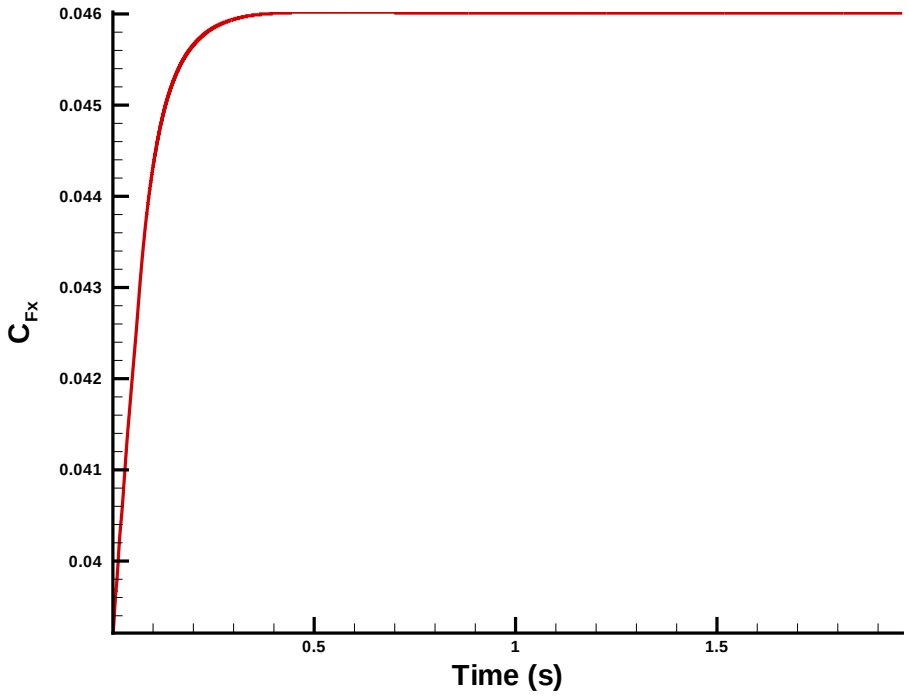

Figure 17: S-A x force coefficients on carrier in free flight

Previous research has shown the B-L turbulence model to be unreliable for separated flows. However, B-L shows reasonable accuracy for base pressure coefficients when comparing to theoretical and empirical values, which implies base pressure does not significantly depend on capturing separated flow features within the near wake of the vehicle. This shows the inviscid flow features remain the dominant factors in computing the mean base pressure, while viscous effects show the turbulent structures present in the subsonic near wake are responsible for oscillatory behavior in base pressure. DES also shows a reasonably accurate depiction of the base pressure compared to the two models. Interestingly, both B-L and DES are very close to computing the same C_{p_B} at the center of the base.

Both B-L and DES pressure distributions do not completely follow the same shape of Herrin and Dutton's, where the lowest pressure should be found in the center. However, the pressure is still fairly uniform. A cause for concern in the B-L C_{p_B}'s is the drop in pressure near the outer edges. This may be an effect of not capturing the shear layer accurately. DES captures the pressure rise towards the outer edges. The S-A pressure distribution is obviously not correct, since the pressure towards the center is the highest.

Since B-L has shown it can provide reasonable approximations of base pressure, it will be included in further studies, even though the separated wake will be completely unreliable. DES will be included because it also shows a reasonable accuracy for base pressure coefficient (compared to theoretical values) and has proven itself in previous research to provide better depictions of separated flows than B-L. The S-A turbulence model will not be included in any further studies because of its tendency to damp out unsteadiness in the flow and its inaccurate calculation of base pressure.

4.1.2 Near-Wake Region in Free Flight. Another way to analyze the turbulence models is to take data from the near-wake region. From what is known of base flows at the present, important features include a recirculation region, a free shear layer and reattachment shocks. Figure 18 shows this region for the B-L and

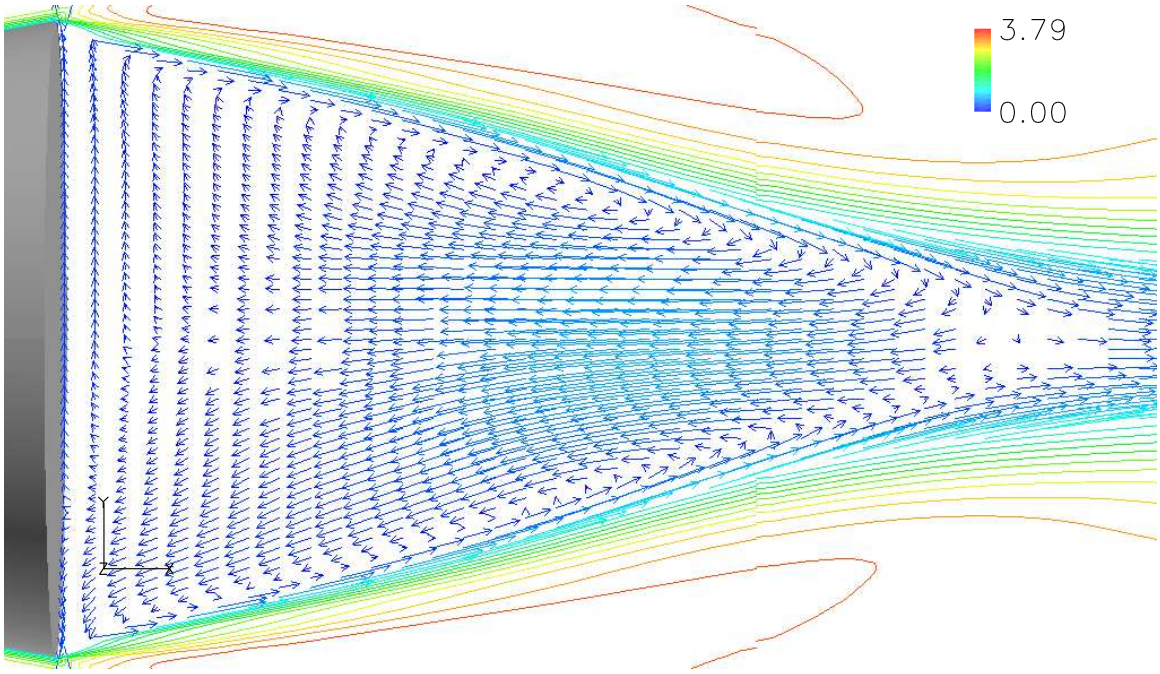

(a) B-L

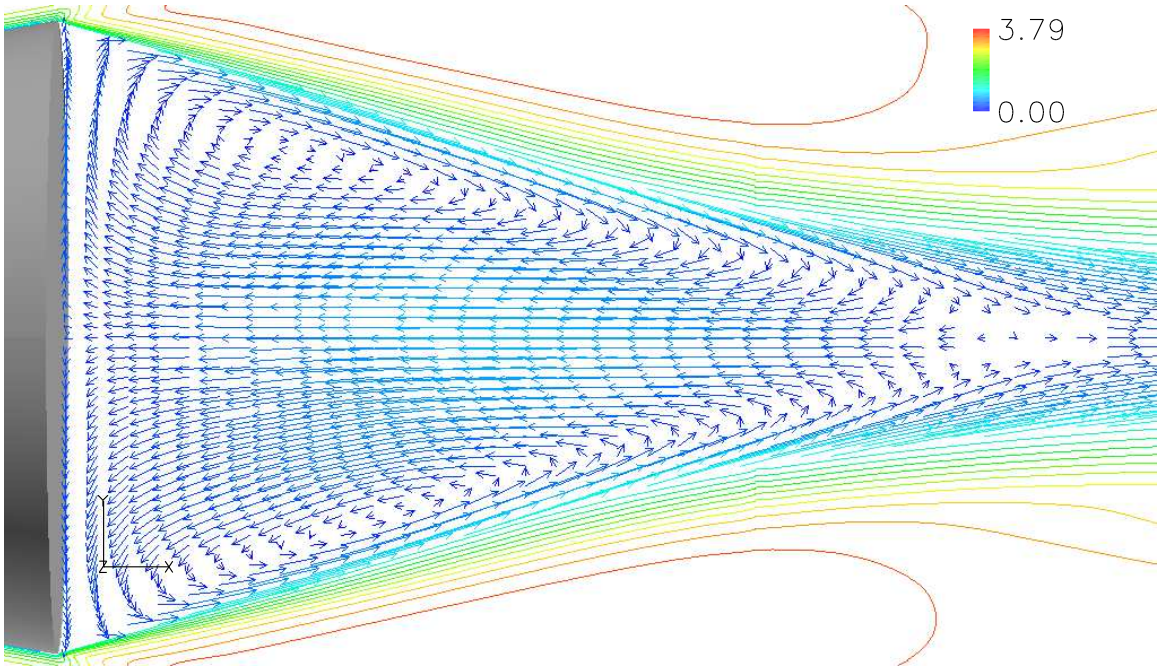

(b) DES

Figure 18: Near-wake vectors for atmospheric cases colored by Mach number

DES turbulence models. The recirculation area is shown with a coordinate surface of velocity vectors on the x-y plane within the shear layer. The shape of the shear layer is captured with contours of Mach number with the threshold set to capture only features outside of the shear layer. Velocity vectors and Mach contours are both colored by Mach number. The B-L turbulence model computed a solution that is symmetric by outer shape, but the inner wake region shows asymmetric behavior when comparing the top and bottom regions. This can be seen since velocity vectors in the lower half of the near wake appear larger than the top half. Also, the majority of velocity vectors along the base are pointing downward. The recirculation region for the B-L near-wake is almost non-existent. The DES near-wake is symmetric by shape and by inner velocity vectors. When comparing the two models, it is apparent the DES model is predicting more recirculation than the B-L model.

A quantitative approach to defining important features in the near-wake region is shown in Figure 19. It is similar to the work of Herrin and Dutton where the u

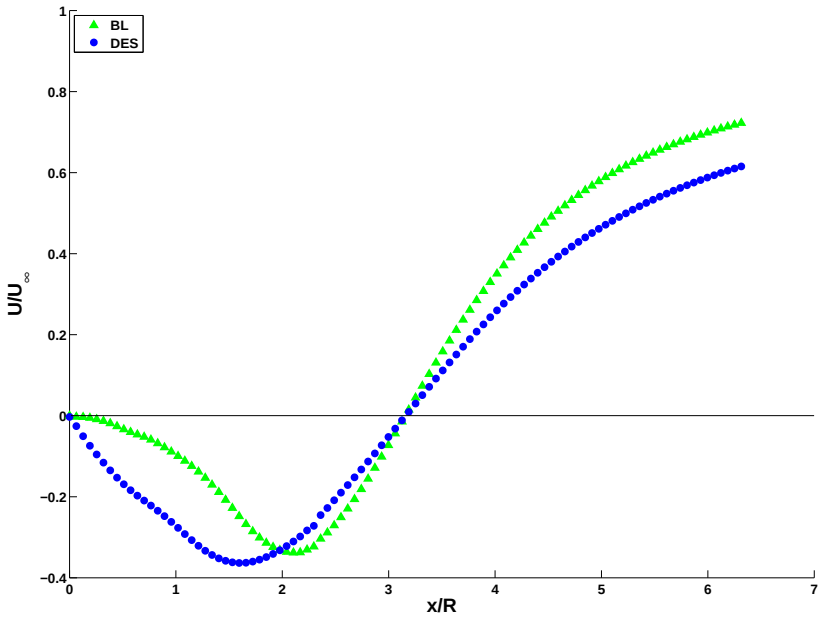

Figure 19: Non-dimensional streamwise velocity in near-wake region along center-line

velocity is non-dimensionalized by the free stream velocity and plotted against the non-dimensional distance from the carrier's base. Data from both turbulence models are included.

The rear stagnation point for both turbulence models can be seen by where their plots cross the x axis where U/U_∞ is 0. This occurs at approximately 3.2 x/R for both. The maximum reverse velocity occurs at 1.5946 x/R for DES and is approximately 36% of the freestream velocity, while the B-L maximum reverse velocity occurs at 2.1 x/R and is approximately 33% of the freestream velocity. With a freestream Mach number of 2.93, the maximum velocity using DES is Mach 1.06 and B-L is Mach 0.992. The major difference between the two turbulence models is the location of maximum reverse velocity. DES computes a solution where the maximum reverse velocity is closer to the vehicle's base. This data will be compared to the wind tunnel without a sting data in order to quantify wind tunnel effects in the near-wake.

4.2 Wind Tunnel - No Store

Wind tunnel cases are important because they provide the first step in changes between the experimental setup and free flight. Effects of the wind tunnel include reflected shock/expansion interactions as well as encased flow, which will not allow any flow out of the fixed area for a given cross-section. Figure 20 shows the carrier in

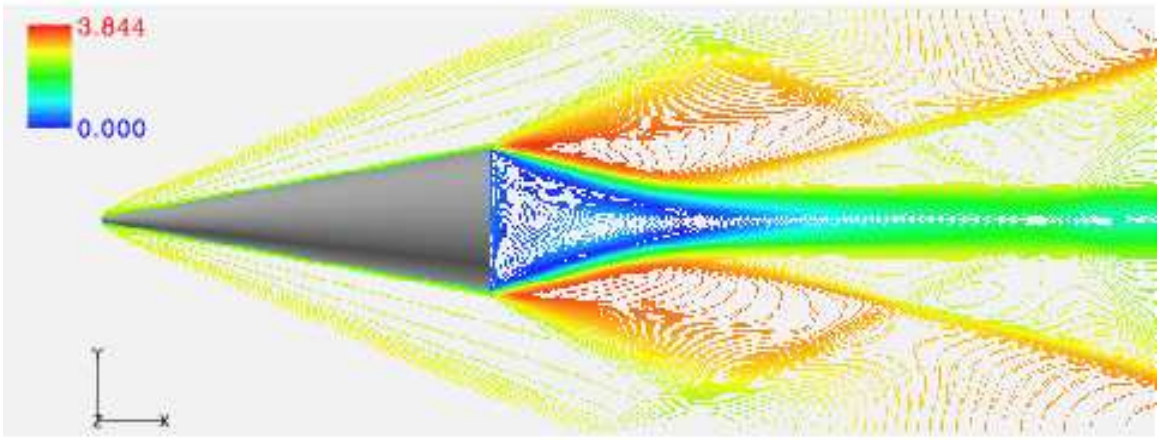

Figure 20: Contours of mach for carrier in wind tunnel, no-sting, Mach = 2.93

the wind tunnel without the sting using contours of Mach computed using the DES turbulence model. As one can see, the shock interactions from the wind tunnel walls create a more complicated environment to analyze store ejections. The base pressure profiles and the near-wake will be used to quantify any differences.

4.2.1 Base Pressures in Wind Tunnel. The wind tunnel environment without a sting should still be symmetric. Figure 21 shows the pressure distribution on the base of the carrier in the wind tunnel without a sting mount, with freeflight values. Values still fall within the theoretical and empirical base pressure coefficients.

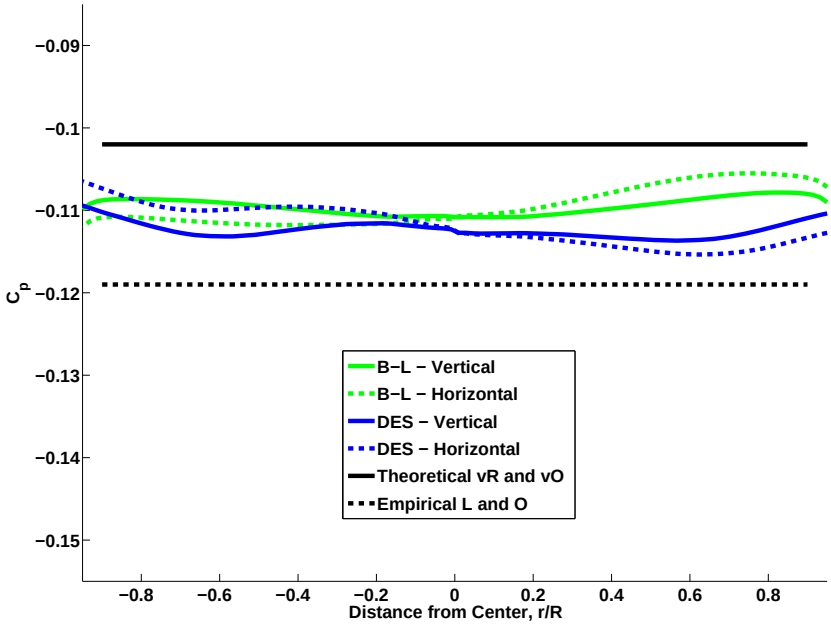

Figure 21: Mean base pressure coefficients on carrier base without sting

Even though the flow is enclosed by the wind tunnel, major changes from free flight are not expected since there is no physical object to reflect major disturbances back upstream through the subsonic flow. Mean base pressures computed from free flight data are -.110 for B-L and -.112 for DES. These values are averages of the vertical and horizontal means for each model. The mean base pressure coefficient values for the wind tunnel cases are -.1095 for B-L and -.112 for DES. This results in a 0.5%

change for B-L and no change for DES. Based on this, it can be said the reflected shocks interfere with the wake downstream, but do not appear to have an effect back upstream when speaking strictly in terms of base pressure. Qualitatively speaking, the reflected shocks intersect at approximately 4 x/D (x/R = 8).

4.2.2 Near-Wake in Wind Tunnel. Figure 22 shows a comparison of the non-dimensional centerline velocities for free flight and wind tunnel cases. The centerline

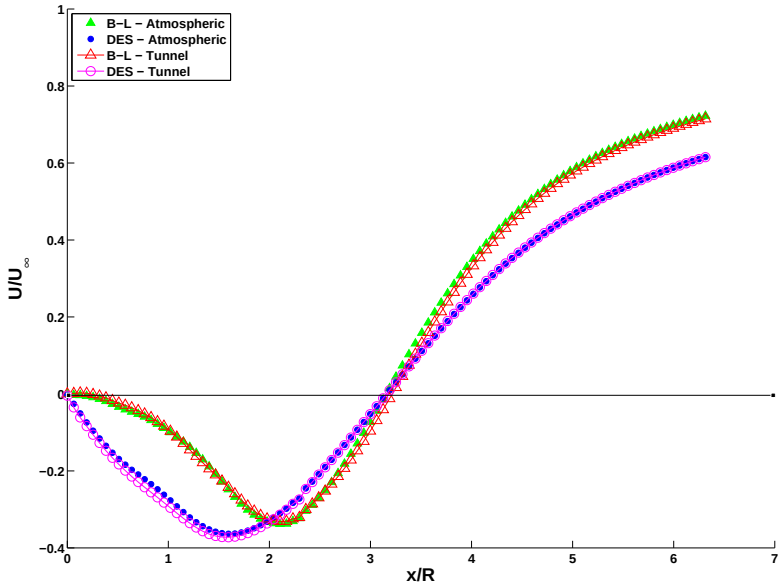

Figure 22: Non-dimensional streamwise velocity in near-wake for free flight and wind tunnel cases along centerline

profile shape is maintained when comparing to free flight cases, but subtle differences are noted. For wind tunnel runs, the maximum reverse velocities reached on the centerline were 33.1% of the freestream for B-L and 37.2% for DES. This marked a 2.0% increase from free flight for B-L and an 2.5% decrease for DES. The location for maximum reverse velocities did not change for either turbulence model. There was also no change in the location for reattachment for either turbulence model. The full recirculation regions are shown in Figure 23 for both turbulence models using the same contour and vector attributes that were used in Figure 18. The DES wind

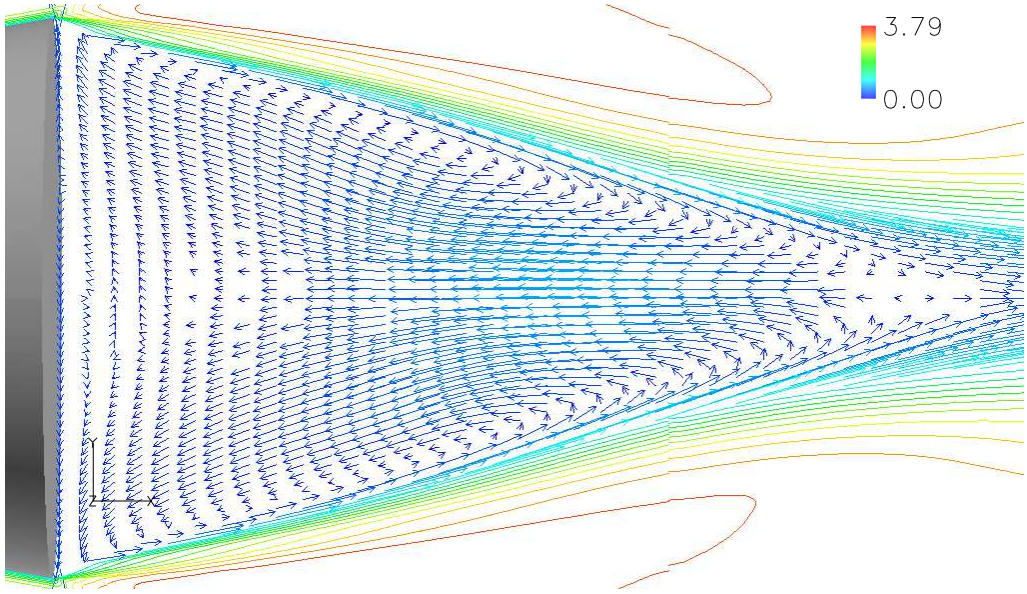

(a) B-L

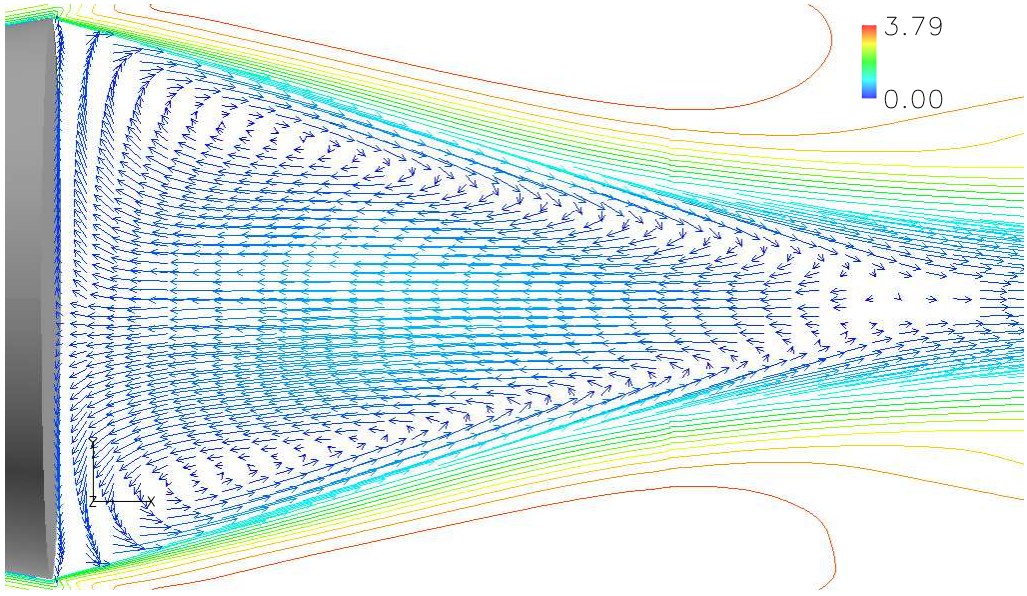

(b) DES

Figure 23: Near wake vectors for wind tunnel cases colored by Mach number

tunnel near-wake looks unchanged from free flight while the B-L wind tunnel near-wake is more symmetric than its free flight case. After comparing wind tunnel and free flight cases, it has been shown the wind tunnel does not significantly affect base pressures or the main features in the near-wake of the carrier vehicle when a store is not present. The quantitative comparisons in the near-wake were between 0.0 and 3.15 x/D, which is within the point at which the reflected shocks were qualitatively found to intersect (x/D = 4).

4.3 Shock Reflections

Before going further it is necessary to describe the effects the shocks will have on wind tunnel solutions. Downstream of the carrier near-wake, reflected shocks will interfere with the flow. The accuracy with which these shocks are captured will effect comparisons between experimental and CFD data. Since geometries and flow conditions have been set to match experimental runs, the intersection of shocks should ideally occur at the same points. Figure 24 shows visual comparisons of the reflected shocks. CFD solutions have over-predicted the length at which the reflected conical shock and reattachment shock intersect. If flow conditions are identical, the cause is most probably due to the inviscid boundary conditions set for the tunnel walls. In reality, there will be a boundary layer present which should be taken into account. This would have dramatically increased the number of grid cells needed within the wind tunnel background grid, which would have made running a large number of test cases impractical. The impact of this when comparing CFD to experimental solutions is the CFD solutions will have a slightly delayed reaction to reflected shocks as the store is moved downstream. The shock system should remain the same for different turbulence models as is shown in Figure 24 because these are not viscous effects. The experimental and CFD cases also show there is not a pronounced difference in the shock intersection locations due to an aft cavity being present on the carrier.

To get an idea of what interference roles shocks play, Figure 25 shows a coordinate surface of the difference in C_p from the free flight carrier superblock and carrier

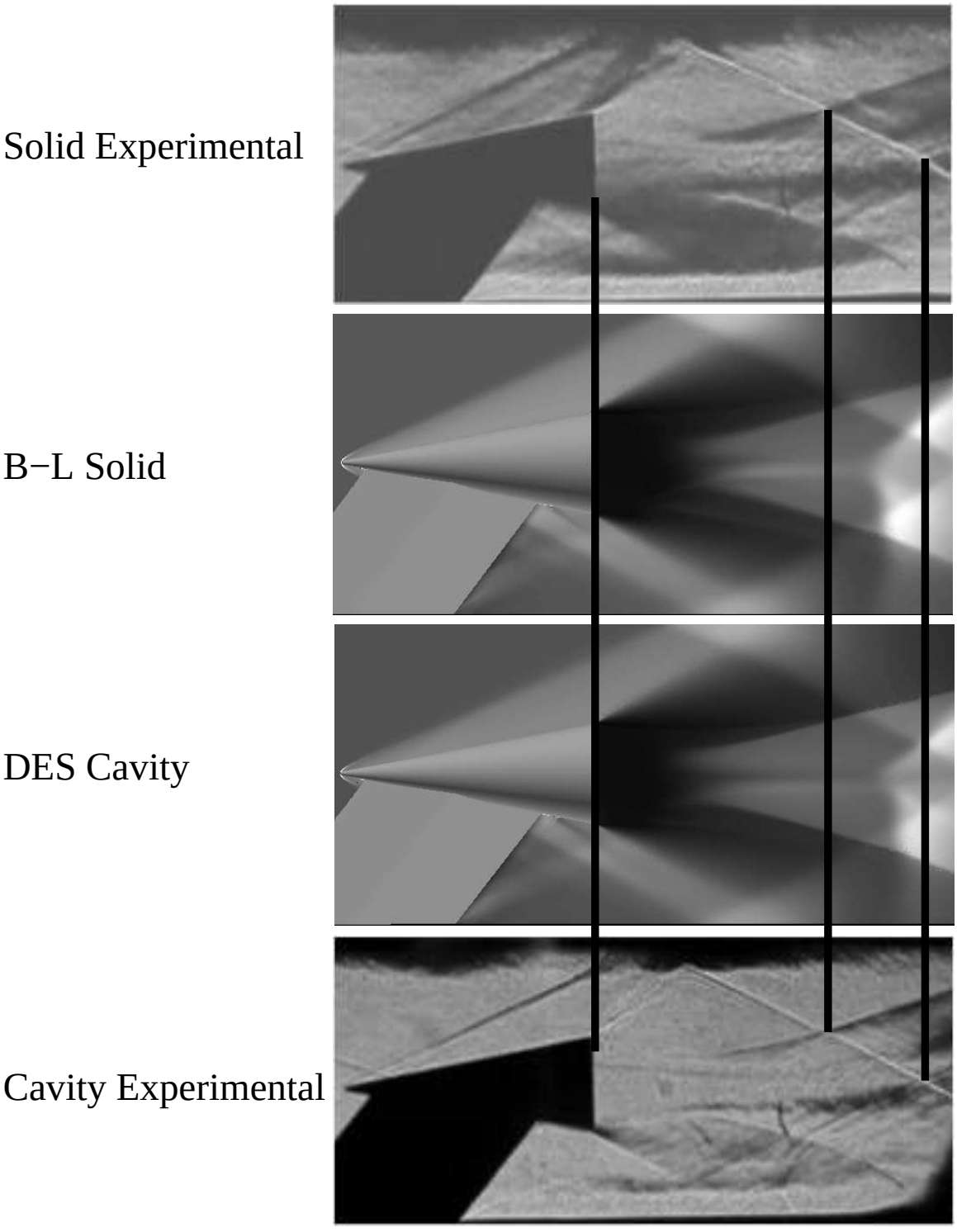

Figure 24: Base flow visualization comparisons - $Re = 3.9x10^9/\mathrm{m}$

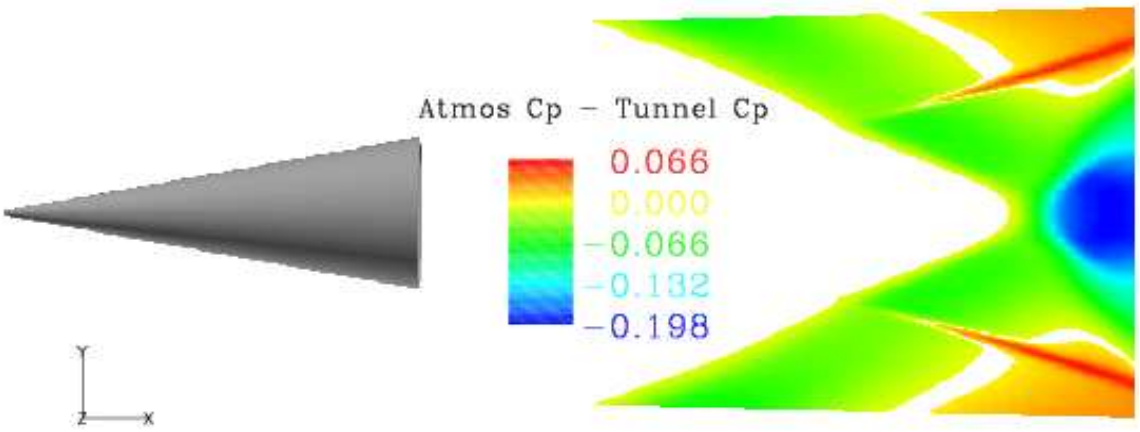

Figure 25: Difference in C_p between free flight and wind tunnel (no store) cases

superblock in the wind tunnel (no sting) using DES. The values between -0.005 and 0.005 have been removed. The area where the shock is reflected is evident due to the change in pressure. The pressure in the area between the nose shock and carrier is relatively the same between the free flight and the stingless wind tunnel environment. This is expected since shocks are inviscid phenomena. The pressure around the store will thus be affected only when it passes through the reflected shock.

The free flight wind tunnel comparison is the cleanest example as far as interference effects go. The addition of the sting will cause even more flow field disruption. Figure 26 shows a comparison of the shock environment of the wind tunnel case with a sting relative to the atmospheric case using DES. Bluish colors represent the atmospheric pressure contours and red-orange colors are wind tunnel pressure contours with the sting. The coordinate surface was placed on the x-y plane and both carrier models are solid. As one can see, reattachment shocks are no longer symmetric due to the sting interference. This will cause force and moment differences on the store since the flow field is no longer symmetric about the x-z plane. Figure 27 shows the same data on a horizontal plane. The same contour details apply to Figure 27 as were applied to Figure 26. The reattachment shocks appear to be symmetric and match up well with the free flight case. The shock off of the cone does not match up because of its interaction with the oblique shock from the sting. Since the leading

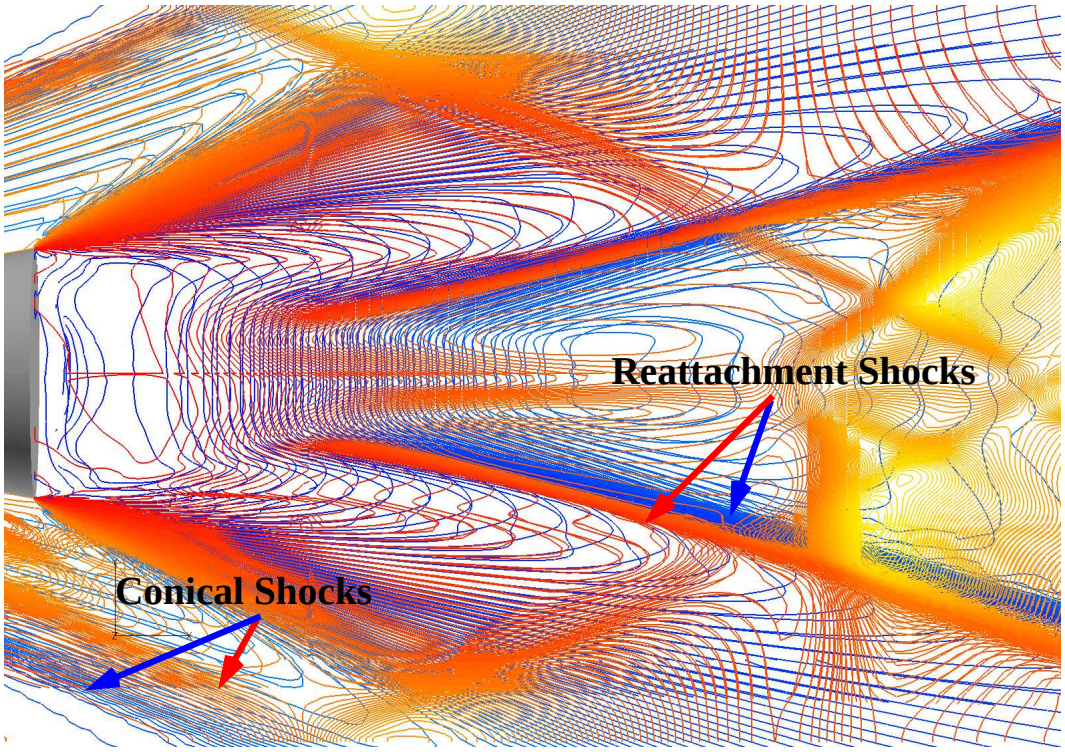

Figure 26: DES shock interactions with sting present (x-y plane)

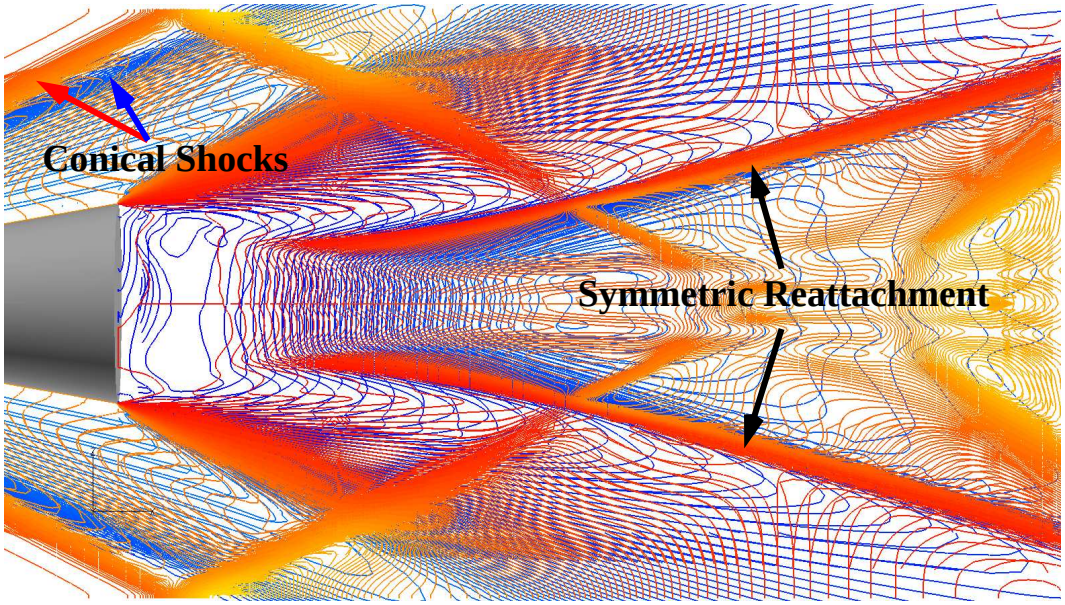

Figure 27: DES shock interactions with sting present (x-z plane)

shock is essentially weaker, the Mach number at the base is higher than it would have normally been in free flight, which creates a stronger expansion. This is evident as the red contour lines show the expansion region is thicker. Since the flow is turned at a steeper angle the flow reattaches itself quicker, which is shown by a close up view of the near-wake in Figure 28.

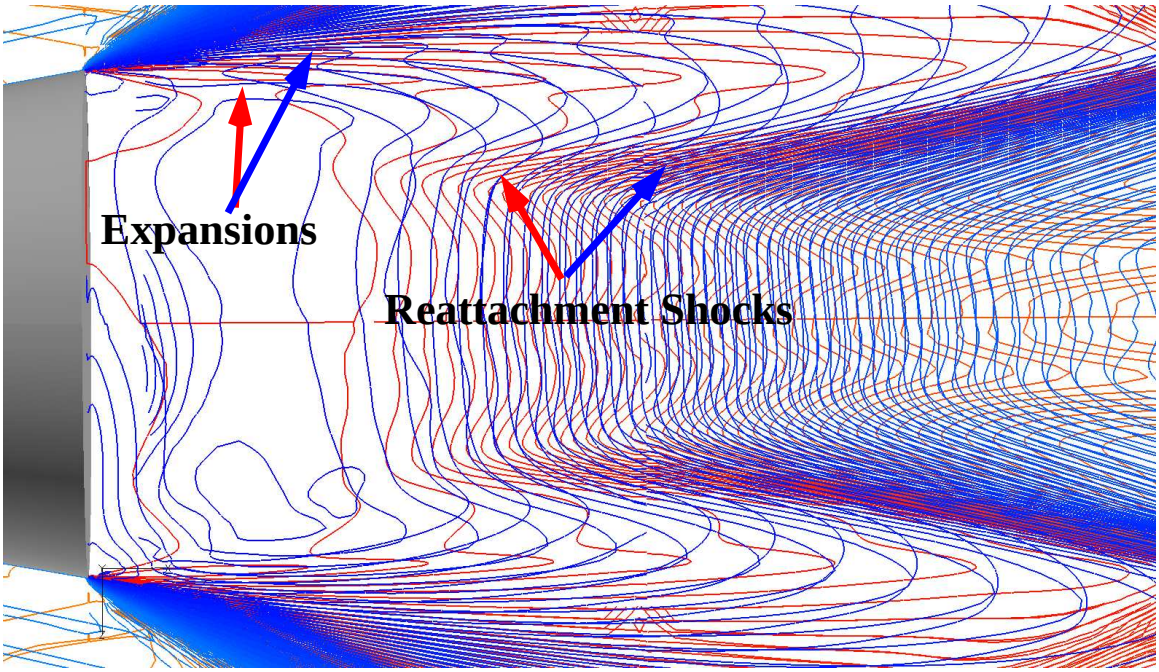

Figure 28: Close-up of expansion region and reattachment shocks (x-z plane)

Drag and pressure effects that will be felt by the store are three dimensional and cannot be fully explained by two coordinate planes. The three dimensional aspect of the problem can be seen in Figure 29 where iso-surfaces of pressure gradient magnitude were chosen to show both shocks and expansions. The conical structure behind the model is the reattachment shock. The three dimensional nature of the shock interactions will present difficulty in examining the sting/tunnel effects on the store using cut planes.

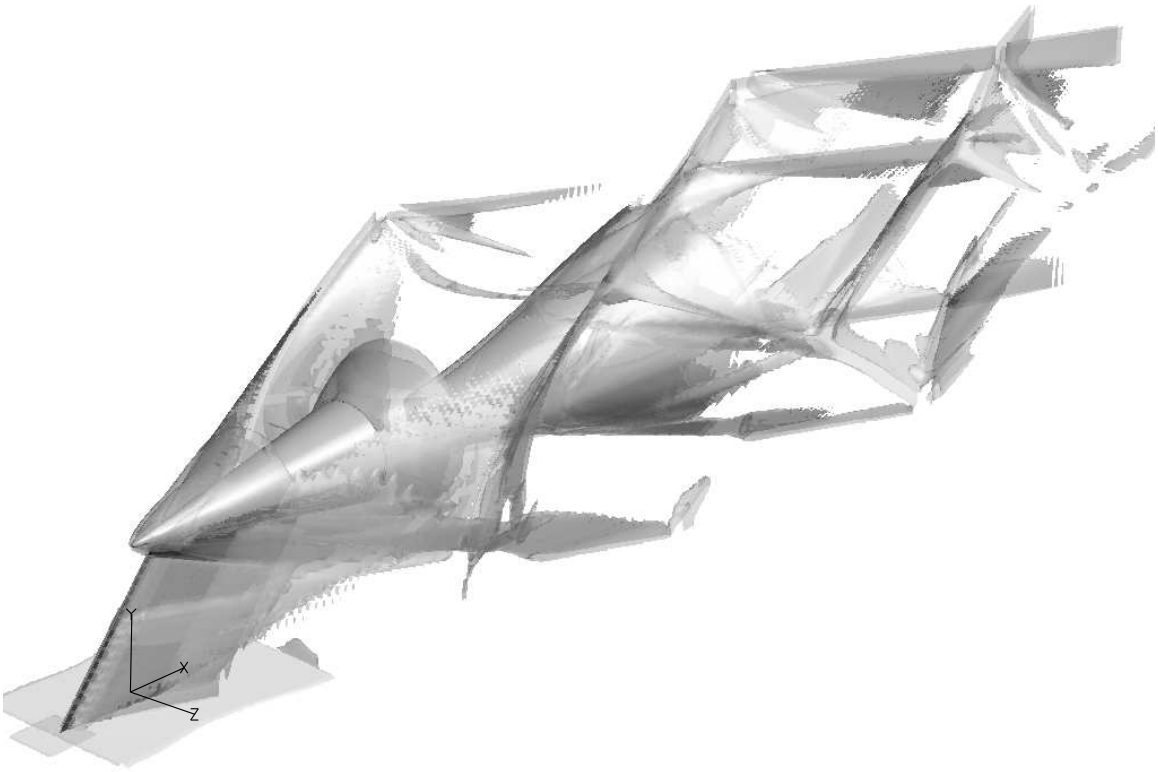

Figure 29: DES three dimensional shock interactions in wind tunnel environment with sting

4.4 Wind Tunnel with Sting - No Store

4.4.1 Base Pressures in Wind Tunnel with Sting. CFD and experimental data can be compared directly for cases with a sting present. Asymmetry of the flowfield due to the sting can also be studied. Figure 30 shows base pressure profiles for atmospheric and wind tunnel (with sting) cases, compared to experimental results. The experimental values are a guideline for the CFD solutions. It should be noted that the pressure is very low so precise PSP data could not be extracted. However, at the center of the base the pressure was taken using a static pressure port, which reflects the most accurate experimental data point. Free flight values will be referenced when computing percent changes due to the sting.

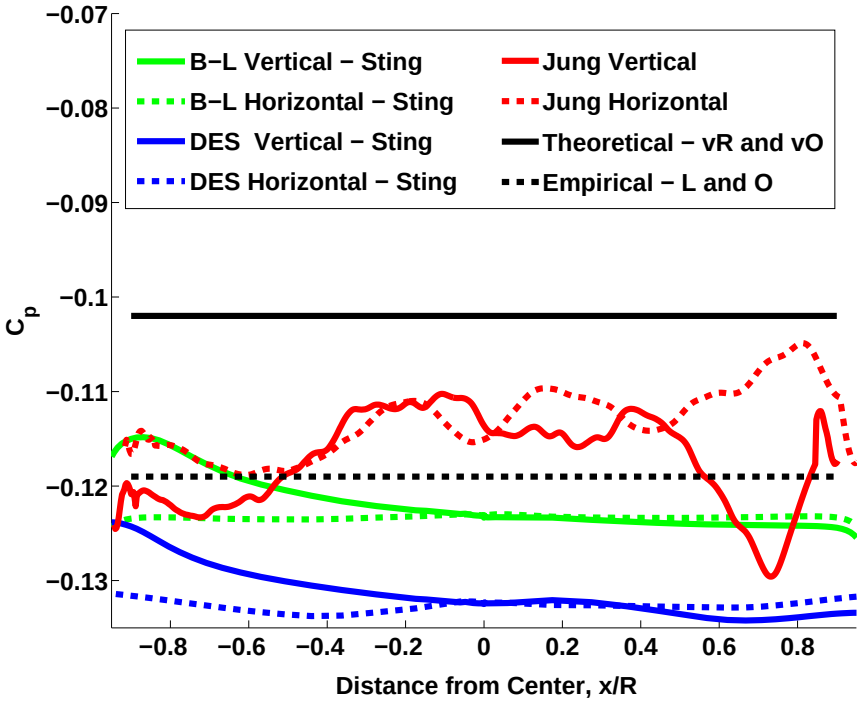

Figure 30: Mean base pressure coefficient comparisons with sting

B-L computed a decrease in mean base pressure of 11.8% when a sting is present and DES computed a decrease of 17.5%. Using Figure 3 for a rough estimate of total drag shows at Mach 3 the base drag accounts for approximately 85% of the total drag for a slender cone. Keeping this in mind, a 17.5% decrease in base pressure would significantly effect the total drag if this data was taken during wind tunnel experimentation.

The asymmetric effects due to the sting can also be seen in the vertical pressure profile for CFD cases. Experimental cases do not show any significant biases due to the sting. The horizontal pressure profile on the base is fairly uniform. The drop in base pressure and asymmetry of the vertical pressure distributions can both be explained using simple inviscid analysis of the flow field.

First, due to the sting, there is a vertical pressure gradient which causes the flow to become asymmetric. Figure 31 shows the surface pressure distributions for

experimental and CFD cases. For the CFD case, the turbulence model used was B-L. The diagonal lines in the PSP are due to slight imperfections in the model build and paint application. It can be assumed that there should be almost no difference between DES and B-L for these surface pressure coefficients since the only turbulent activity taking place on these surfaces is a turbulent boundary layer, which both turbulence models have been proven to be reasonably accurate at capturing. Overall, agreement between the CFD and PSP results is reasonable.

The conical shock and oblique shock off of the sting is clearly creating a pressure gradient, which causes the flow to be redirected towards the top of the carrier. Figure 32 shows this with streamlines seeded near the front portion of the sting where

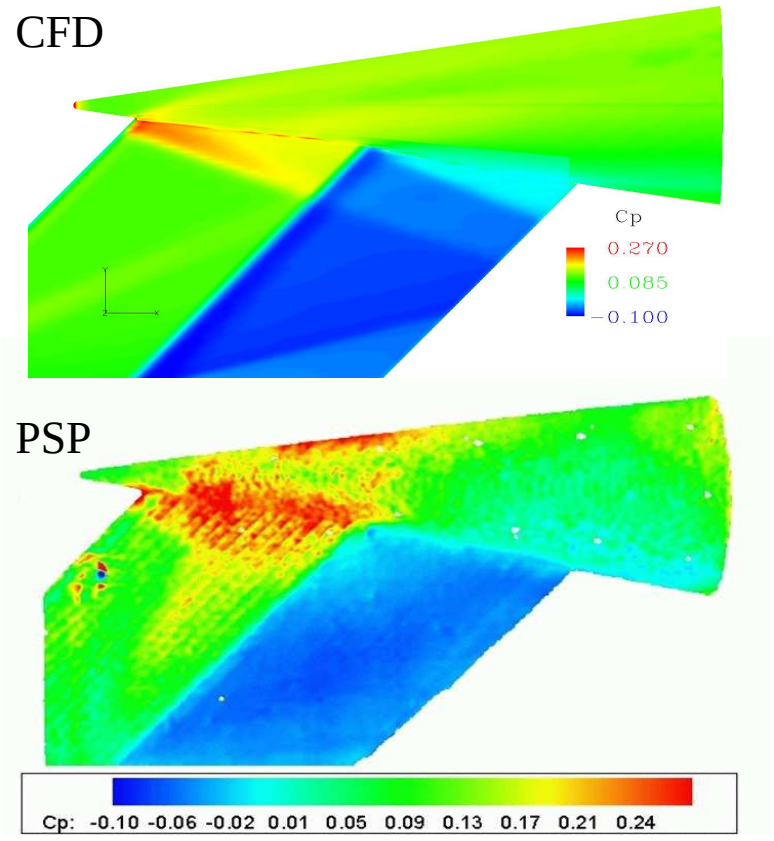

Figure 31: CFD and PSP comparisons of sting effects

the carrier is attached. The surface contours are colored with pressure coefficient and the streamlines colored with density. The asymmetry of the flow is apparent.

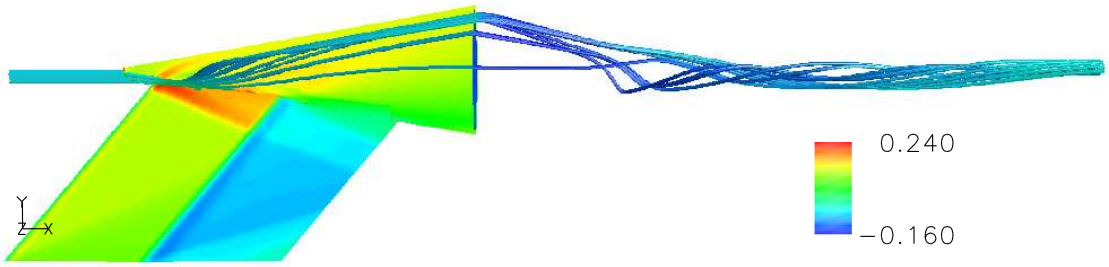

Figure 32: Asymmetric effects of sting

At the top of the PSP image in Figure 31 there is a region of high pressure which does not appear in the CFD solution. Initially, the cause of this was theorized to originate from a shock due to an upstream imperfection in the wind tunnel, which was reflected until it impinged on the upper surface of the carrier. It is visible in Figure 33. These are Mach waves according to Jung [16], which originate from a slight misalignment of joints between the wind tunnel stilling chamber and test section. This was proven by measuring the angle between the freestream direction and wave of interest and comparing to Mach angles from a Prandtl-Meyer table [2]. The measured angle was approximately between 19^o and 20^o. The Mach angle from the Prandtl-Meyer table lies between 19.8^o and 20.2^o (values taken from Mach 2.95 and Mach 2.90 respectively). Higher resolution of the measured angle was not possible, but if the angle measured from the wind tunnel Mach wave was larger, it could be considered a weak shock, which would effect the flow downstream.

This explains the vertical pressure gradient on the base of the carrier, but does not completely explain why the mean pressure is so different from symmetric cases. If the pressure is much lower on the base, inviscid flow relations should be sufficient in explaining why this happens since base pressure is heavily dependent on Mach number and the angle at which the flow is expanded. Since the current problem poses three dimensional effects, expansion angles are hard to quantify and compare around a circular body due to the asymmetric effects of the sting. An alternate

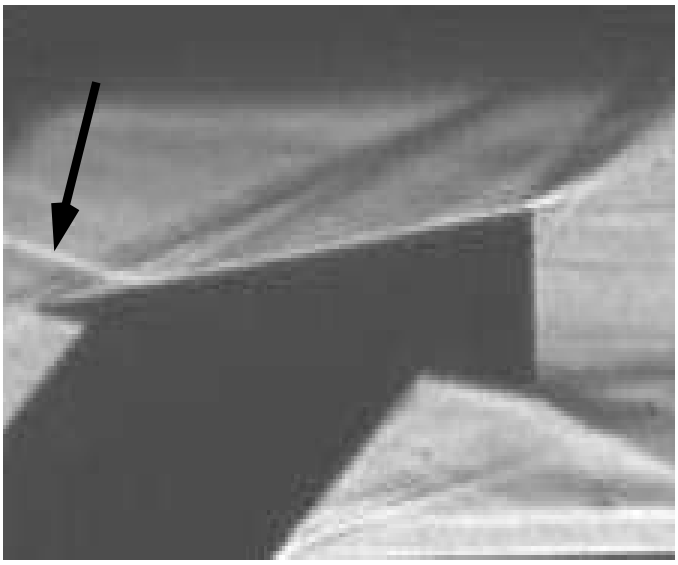

Figure 33: Schlieren image of shock reflecting off of the carrier

way of explaining this is the Mach number approaching the base on all sides of the carrier must be greater when a sting is present than Mach numbers experienced by symmetric cases. Based on free flight and no sting wind tunnel cases, it was shown that wind tunnel encasement played a negligible role in changing the base pressure. The addition of a sting, however, causes such a large base pressure difference that the sting must play a significant role in increasing the effective Mach number around the base.

Figure 34 is a contour plot of Mach number on the y-z plane immediately before the base of the carrier for the previously discussed flight cases. White is the upper limit of the color bar, Mach 3.0. The sting has interrupted the flow in such a way that an area of higher Mach numbers is seen around the base of the carrier with the sting when compared to symmetric cases. Higher Mach numbers lead to an increase in the angle of expansion around the base, which lead to lower base pressures. This explains why CFD runs are lower relative to other CFD runs, but does not explain the significant difference between experimental and CFD values. There are a number of variables that can factor into this, but they are all speculation. Figure 34 also shows the difference in boundary layers due to the stings presence just before expansion.

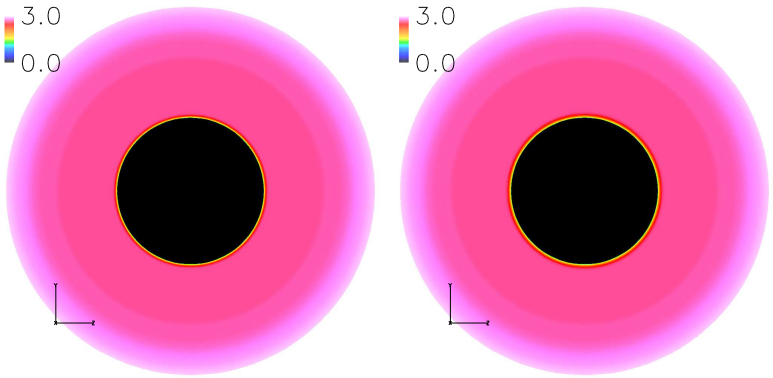

(a) B-L Atmospheric (b) DES Atmospheric

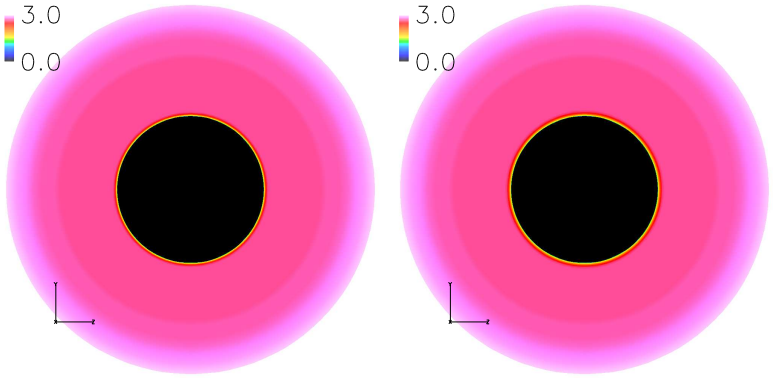

(c) B-L Tunnel (d) DES Tunnel

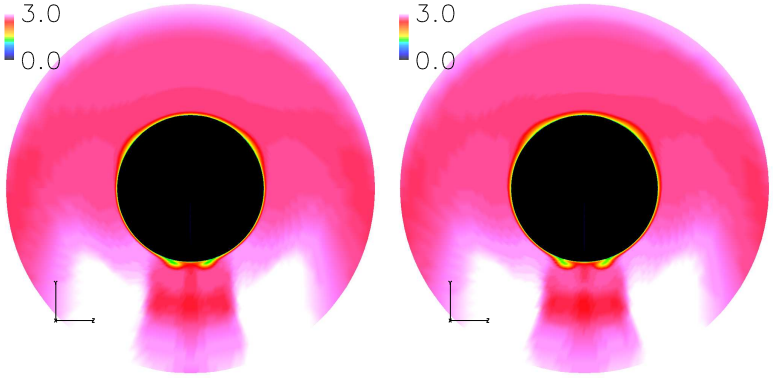

(e) B-L Tunnel - Sting (f) DES Tunnel - Sting

Figure 34: Contours of Mach number at the base of the carrier for various cases

The atmospheric and no-sting cases have a uniform boundary layer profile around the circular geometry, while the wind tunnel cases with a sting show turbulent effects creating a much thicker boundary layer in certain regions. The top portion of the circular base has a thick boundary layer due to the redirected vertical flow off of the sting. The bottom portion has tear drop shaped boundary layer profiles where the boundary layers between the sting and carrier are most likely interacting and causing vortical flow.

The difference between turbulence model base pressures can be compared by analyzing the expansion region. DES must be computing stronger expansions at the base than B-L when the sting is present, since the base pressure values are lower. This is shown to be the case as shown in Figure 35, where pressures and densities are plotted through a vertical data line which passes through the expansion fan at the base. Both

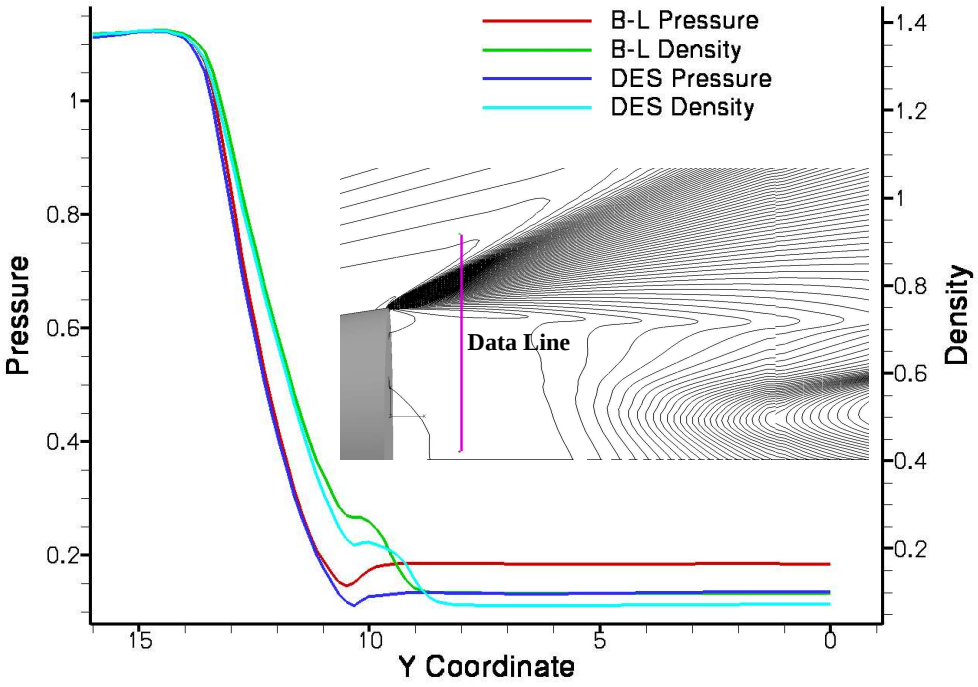

Figure 35: Pressure and density changes through expansion and shear layer for DES and B-L turbulence models

turbulence models have the same pressure and density before the expansion region. The DES turbulence model case expands both the density and pressure over a larger distance, equating to a larger/stronger expansion region. The data line is well into the near-wake, where the flow values hold constant throughout. This proves nothing within the near wake is causing the pressure and density differences. The pressure rises slightly at the end of the expansion for both turbulence models, which ultimately brings the B-L pressure even higher than the DES pressure.

The pressure rise at the end of the expansion is due the presence of a lip shock. It can be seen more clearly in Figure 36, which shows the near-wake region using density contours. The number of contours is the same for both turbulence models. Jung [16] observed lip shocks in his research only when a store was present in the wake and the carrier model had a cavity. Van Raalte and Oudheusden explain the lip shock is a recompression phenomenon that occurs in order to adjust the static pressure in the boundary layer with the expansion that occurs at the base [31]. It is clear the lip shock is stronger for the B-L turbulence model than the DES model. This helps to explain the lower pressures along the base that the DES model computes. Since lip shocks are associated with the boundary layer as it is transitioned to a shear flow, the different strengths of the lip shocks can be attributed to the ability of each turbulence model's ability to capture separated flows. This shows a major difference in base pressure calculations for the current research is traced back to the turbulence model used in the flow solver. The inability of the B-L model to capture a shear layer can also be seen in figure 36. The shear layer is smeared out compared to the DES case.

4.4.2 Near-Wake in Wind Tunnel with Sting. Vectors in the near-wake are shown in Figure 37. As one would anticipate, symmetry has clearly broken down. Both turbulence models show a recirculation region in the upper corner near the shoulder of the base, and the rest of the wake revolves around this point. Velocity vector scaling is kept the same as atmospheric and no-sting wind tunnel cases in

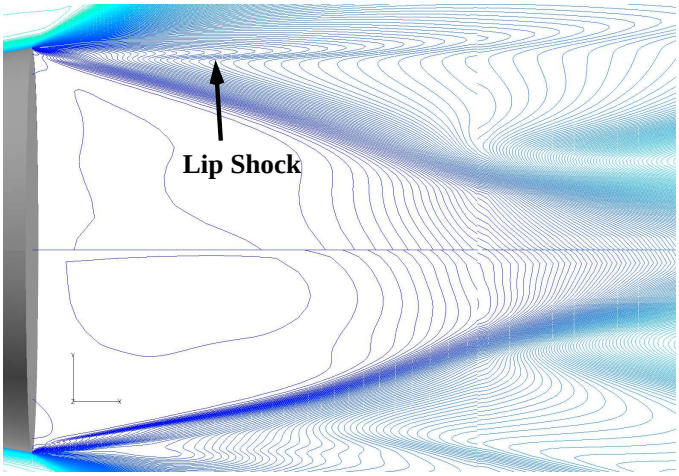

(a) B-L

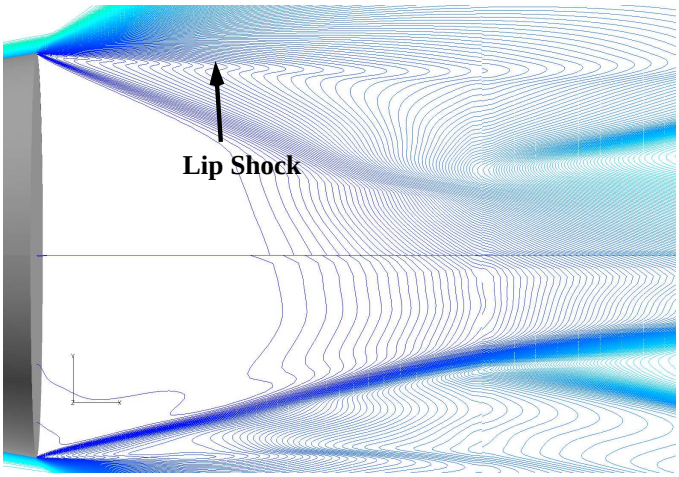

(b) DES

Figure 36: Lip shocks for B-L and DES turbulence models (x-y plane)

order to show the relative velocities of each case to one another. The asymmetry will definitely have an effect for cases in which a store is present in the wake. Since symmetry is no longer present in the near-wake, non-dimensional velocity comparisons along the centerline are not relevant. Figure 38 shows velocity vectors in the x-z plane. Symmetry is maintained as one would expect. Qualitatively speaking, the vectors in the x-z plane can be considered a better representation of the near-wake region.

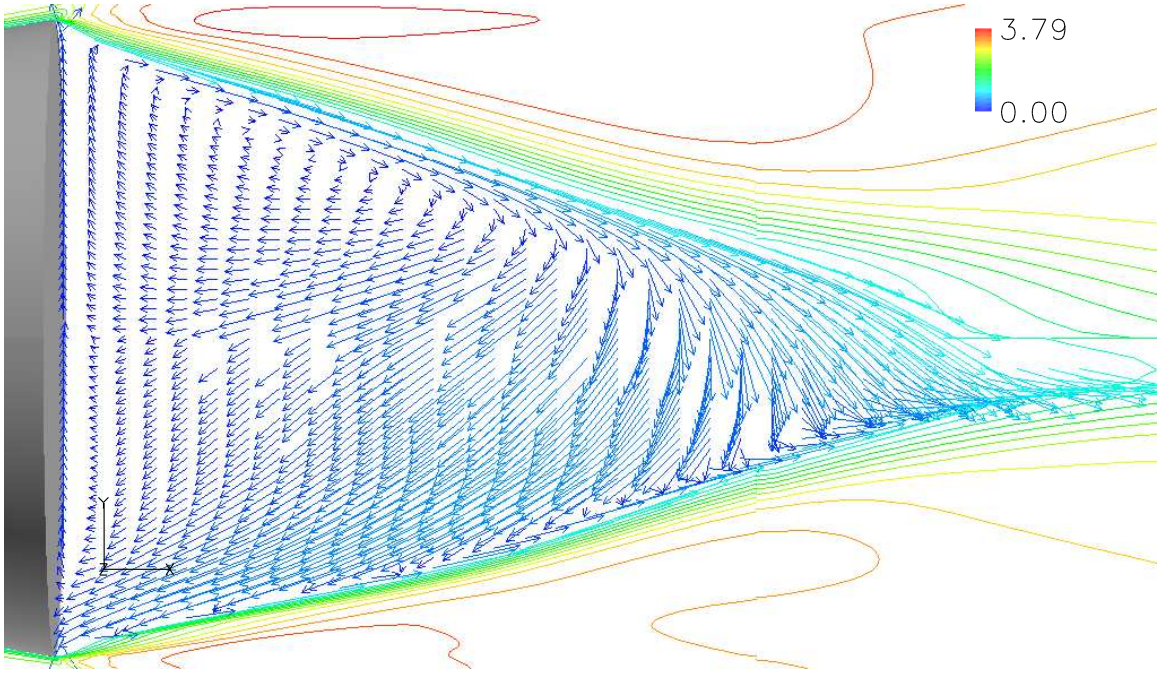

(a) B-L

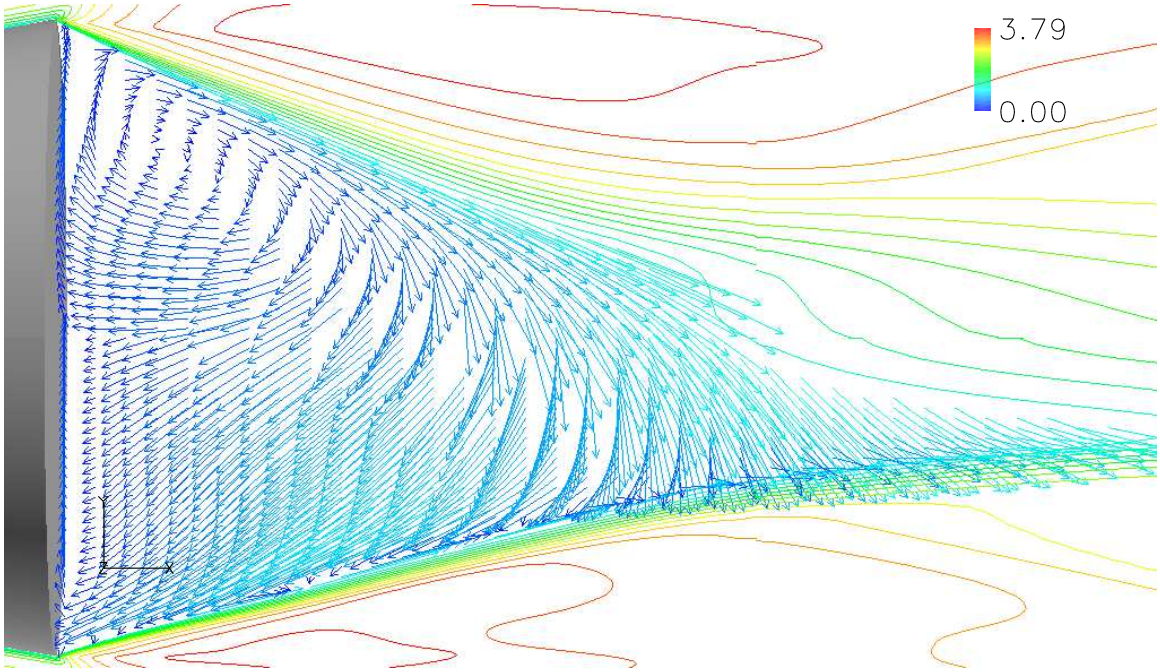

(b) DES

Figure 37: Near-wake vectors for wind tunnel cases with sting present (x-y plane)

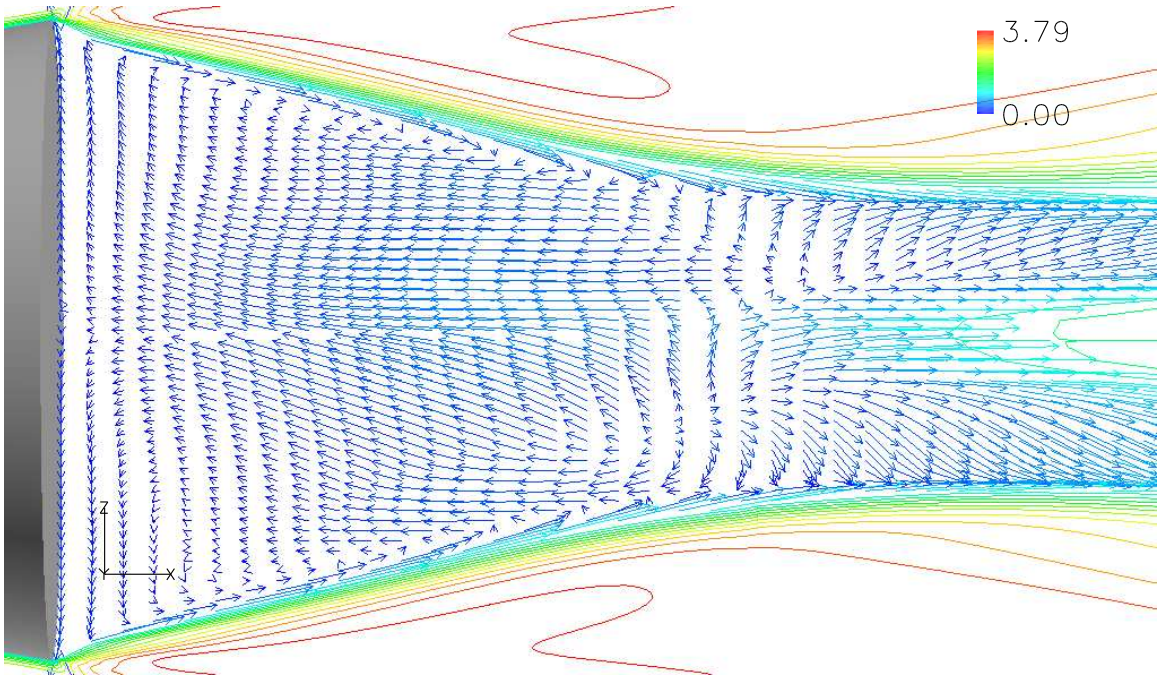

(a) B-L

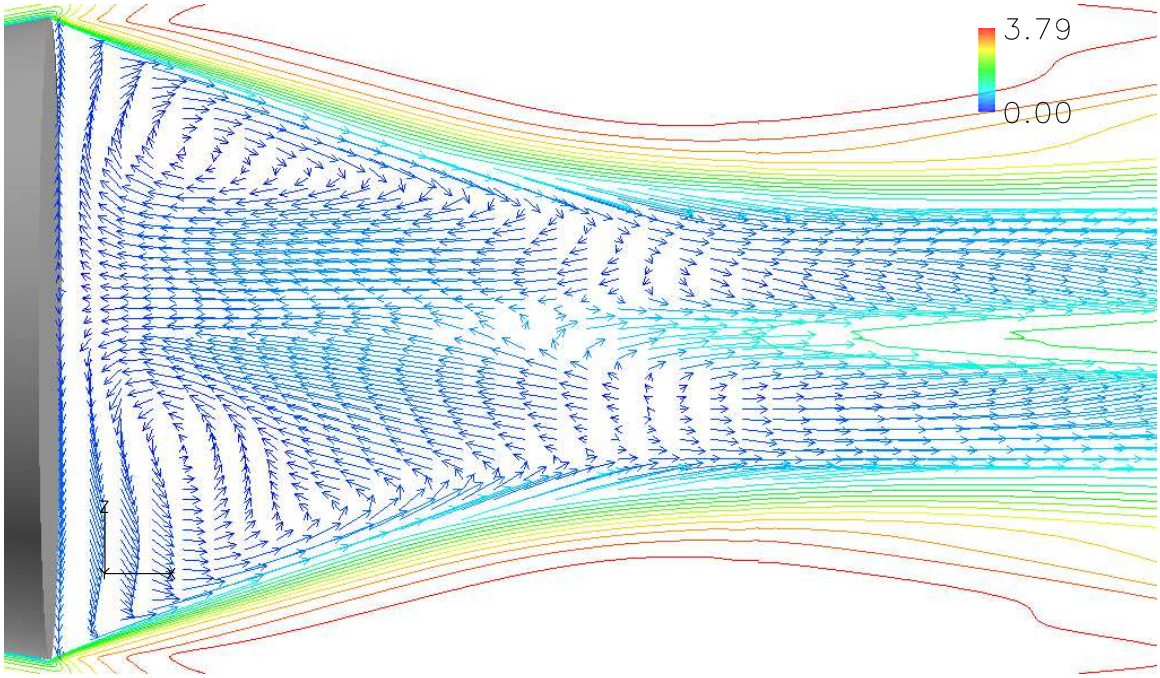

(b) DES

Figure 38: Near-wake vectors for wind tunnel cases with sting present (x-z plane)

4.5 Cavity Effects

Up until now, all cases examined have been those where the carrier is completely solid. It enabled the capture of base pressure profile and comparison to experimental data. In real life, the store ejection would take place out of a cavity. It is therefore necessary to examine the cavity's effect on the flow field since it may have an effect on the recirculation region, thus having an impact on the strength of the expansion and base drag. Figure 39 shows the non-dimensional u velocities for the cavity compared to the velocities of the solid runs without a store present using the DES turbulence model.

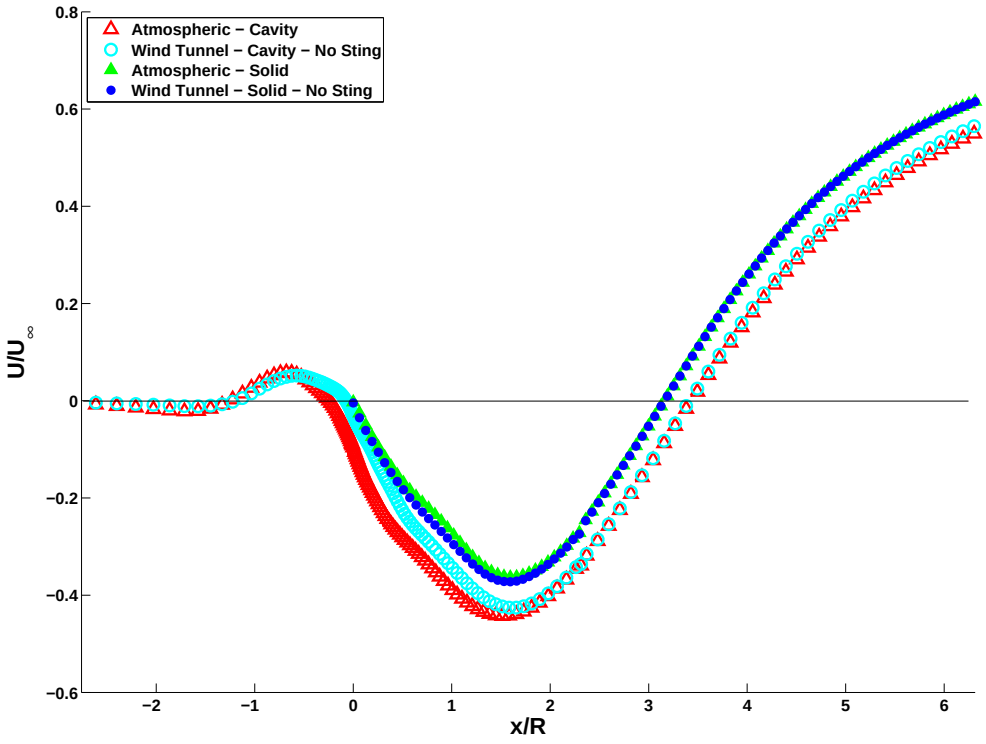

Figure 39: Non-dimensional streamwise velocity in the near-wake of the carrier

The plot shows the velocities inside the cavity are relatively benign deep inside the cavity. At -.6798 and -.5282 x/R for the atmospheric and wind tunnel cases respectively, there is a point of maximum forward velocity within the cavity. This

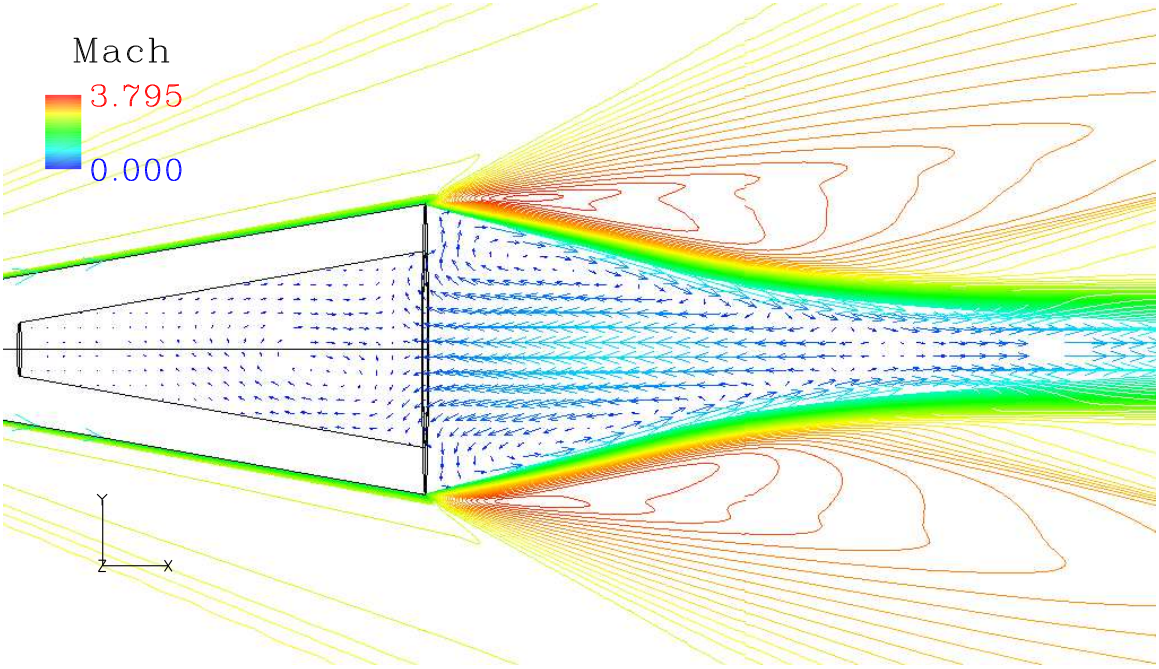

Figure 40: Velocity vectors colored by Mach number for free flight (DES)

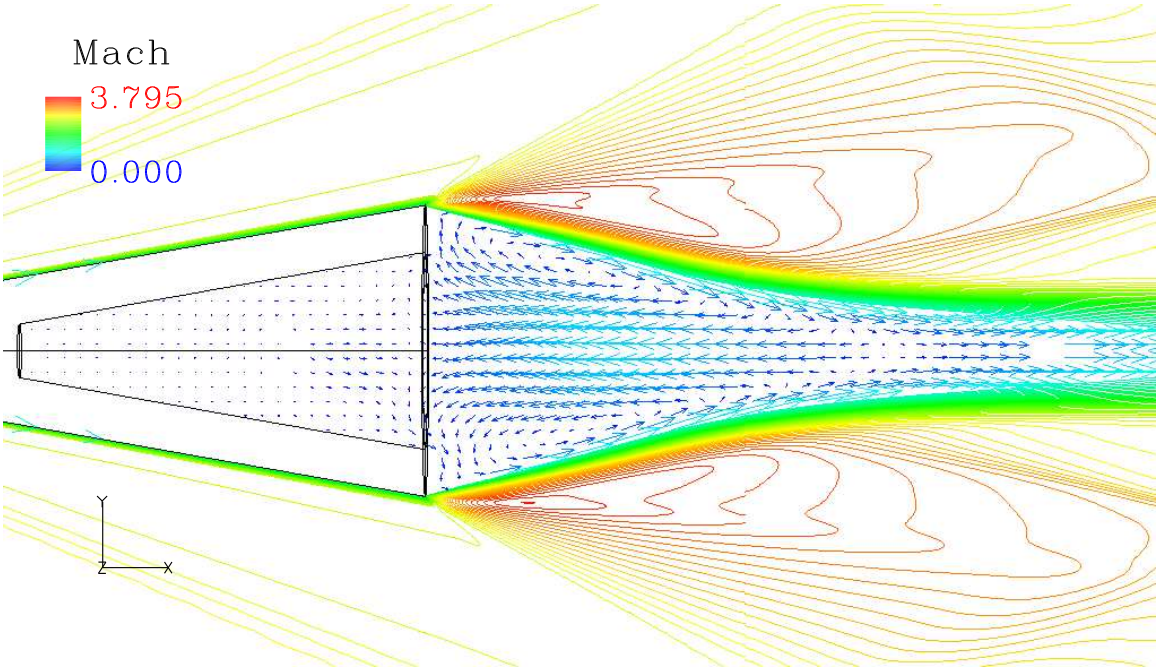

Figure 41: Velocity vectors colored by Mach number for wind tunnel (DES) - no sting

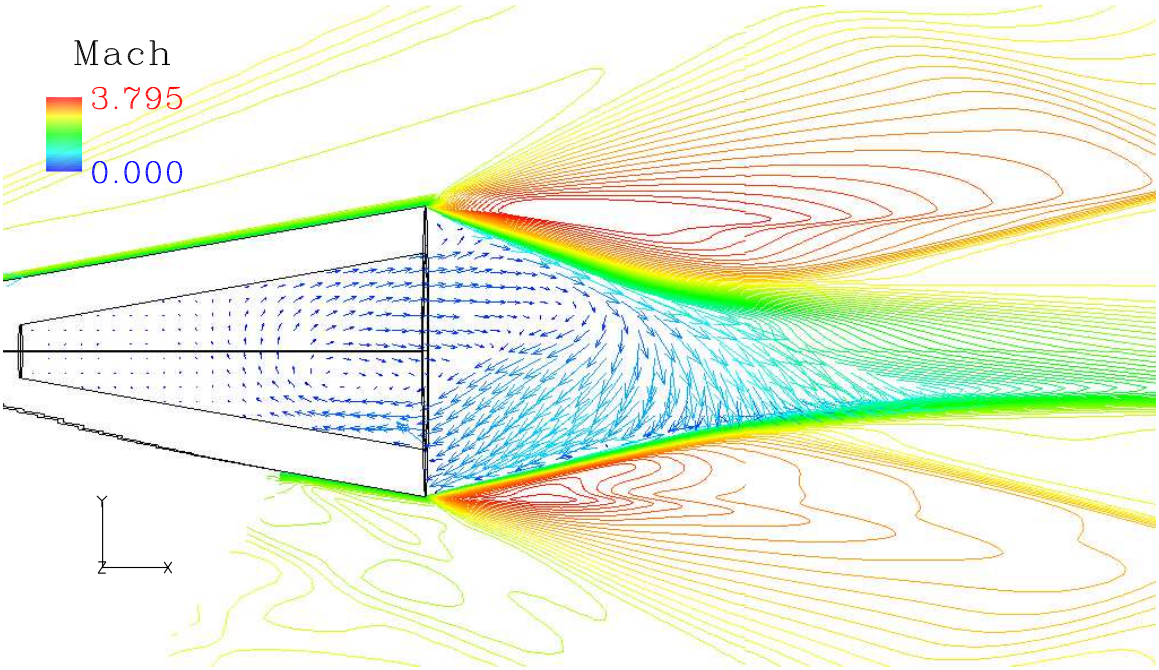

Figure 42: Velocity vectors colored by Mach number for wind tunnel (DES) - sting

value is approximately one half of a percent of freestream for both, which is equivalent to 0.1465 Mach. Using the solid cases as a reference, the maximum reverse velocity for the atmospheric case increased by 21.8% with the addition of the cavity and the wind tunnel case increased by 14.3%. The location for the maximum reverse velocity moved closer to the base by 5% and 4.5% for the atmospheric and wind tunnel cases respectively. The reattachment points were in the same location at 3.44 x/R, which is 7.5% further downstream of the solid cases. These changes show the recirculation region to have more energy than the solid cases, and encompass a longer span aft of the base before reattachment is reached. For a visual representation of the cavity and near-wake regions refer to Figures 40 through 42. Velocity vectors are colored by Mach number as they were in previous studies of solid test cases. The cavity region for the atmospheric and no-sting wind tunnel cases are not symmetric as expected. This is because the flow there is nearly stagnant, making it difficult to get a time averaged solution in a half second. The cavity region for the wind tunnel case with a sting contains higher velocities and a region of recirculation. The near-wake for

the atmospheric and no-sting wind tunnel cases are symmetric when the cavity is present, as they were during tests with a solid carrier. The near-wake for the cavity wind tunnel case with a sting shows no symmetry as the solid case did.

4.6 Force and Moment Analysis

Beggar is able to calculate force and moment data over specified entities. This is obviously important during dynamic 6DOF simulations since the movement of stores depends on knowing these. Using it on static cases enabled the capture of force and moment coefficient data on the store and carrier vehicle for comparison. These force and moment coefficients are defined in Beggar as shown in equations 42 and 43. The reference area for each is the maximum cross-sectional area and the reference length is the diameter. For the store, A_{ref} and L_{ref} were 66.46 mm^2 and 9.2 mm. The carrier A_{ref} and L_{ref} were 363.350 mm^2 and 21.512 mm. F_x and M_x are computed using non-dimensional quantities. The forces and moments of the other axes are found in the same manner.

$$C_{Fx} = \frac{2F_x}{M^2 A_{ref}} \tag{42}$$

$$C_{Mx} = \frac{2M_x}{M^2 A_{ref} L_{ref}} \tag{43}$$

Figure 43 shows an example of the raw force data recorded. The unsteady nature of the base flow region is apparent. The mean values are really what is of interest in the force history data because in most store ejection applications the inertial properties can be considered large enough that high-frequency oscillations will not impact the store trajectory. Table 2 shows those mean values on the store taken for the B-L turbulence model. Assumptions will be necessary to analyze this data. The atmospheric case will be defined as the baseline when comparing the coefficient data. Since everything in the atmospheric cases is symmetric about the x-axis, everything but C_{Fx} is expected to be very small. All force and moment values in Table 2 other than C_{Fx} are of magnitude 10^{-3} or less. It can therefore be assumed that values of the same magnitude or less can be considered negligible, which leaves only the drag coefficients for data analysis.

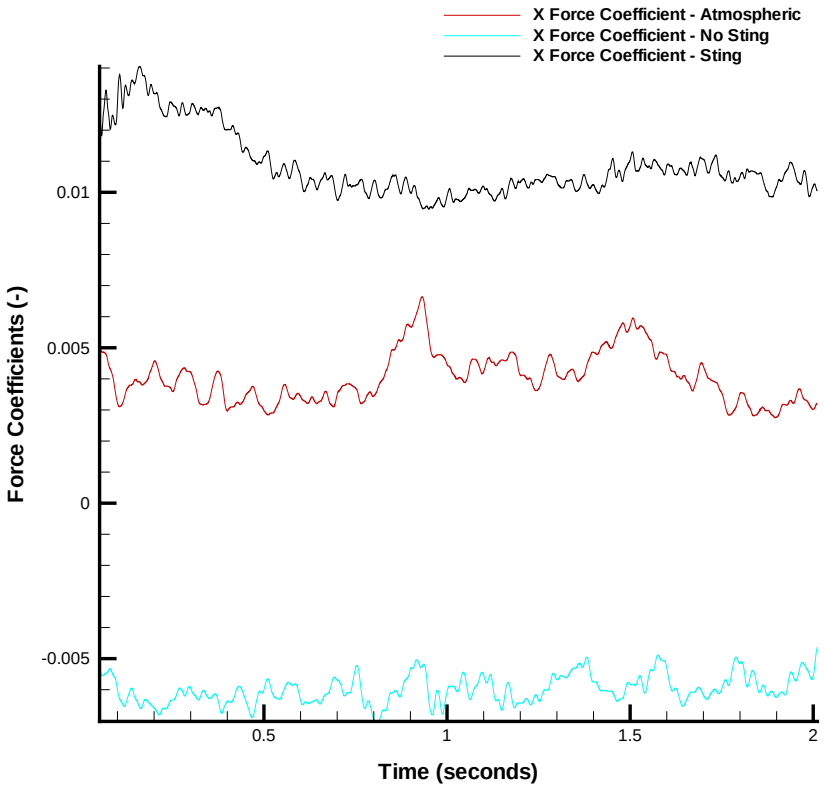

Figure 43: B-L x force coefficients on the store at 0.93 x/D

This assumption can also be applied to the wind tunnel case with no sting since it is also symmetric about the x axis. Wind tunnel data with a sting will be discussed and compared later since a direct comparison to the symmetric cases will not be helpful until effects of the wind tunnel are understood. Also, force and moment coefficients on the carrier are skewed because of the presence of the sting so the integration of pressures on that surface will not be correct. Appendix A shows the tabular forms of the rest of the force and moment data for the store and carrier.

4.6.1 Store Force and Moment Analysis. Looking at C_D data reveals important trends between wind tunnel (no sting) and atmospheric drag data. For the remainder of the force and moment analysis, triangles on the plots denote free flight cases and squares are wind tunnel runs. Filled in symbols are data points where a

Table 2: B-L forces/moments on store with hollow carrier - Re = $3.9x10^8$/m

Atmospheric						
x/D	CFx	CFy	CFz	CMx	CMy	CMz
0.22	-0.061756	0.00032513	-0.0013674	0	0.00010908	-0.00085503
0.92	0.043351	0.0019995	0.00087691	0	0.00078839	-0.0010773
2.23	0.20784	0.0011715	-0.0008095	0	-0.002766	0.0011826
Wind Tunnel - No Sting						
0.22	-0.037282	0.00070583	0.0014111	0	0.00021881	0.00022445
0.92	-0.058456	0.0025514	-0.0023404	0	6.581e-005	-0.00032723
2.23	0.10812	-0.0020036	0.0010261	0	0.00096195	0.0032809
Wind Tunnel - Sting						
0.22	-0.039496	-0.034932	0.0014415	0	-0.00026191	0.0018985
0.92	0.099735	-0.083916	0.0017702	0	0.00090343	0.013829
2.23	0.22291	-0.021402	-0.0033744	0	-0.0077307	0.10107

solid carrier was used. Figure 44 shows the store drag coefficient data for B-L and DES turbulence models with a cavity in the carrier for both atmospheric and wind tunnel cases. Both turbulence models show a suction back to the carrier vehicle at

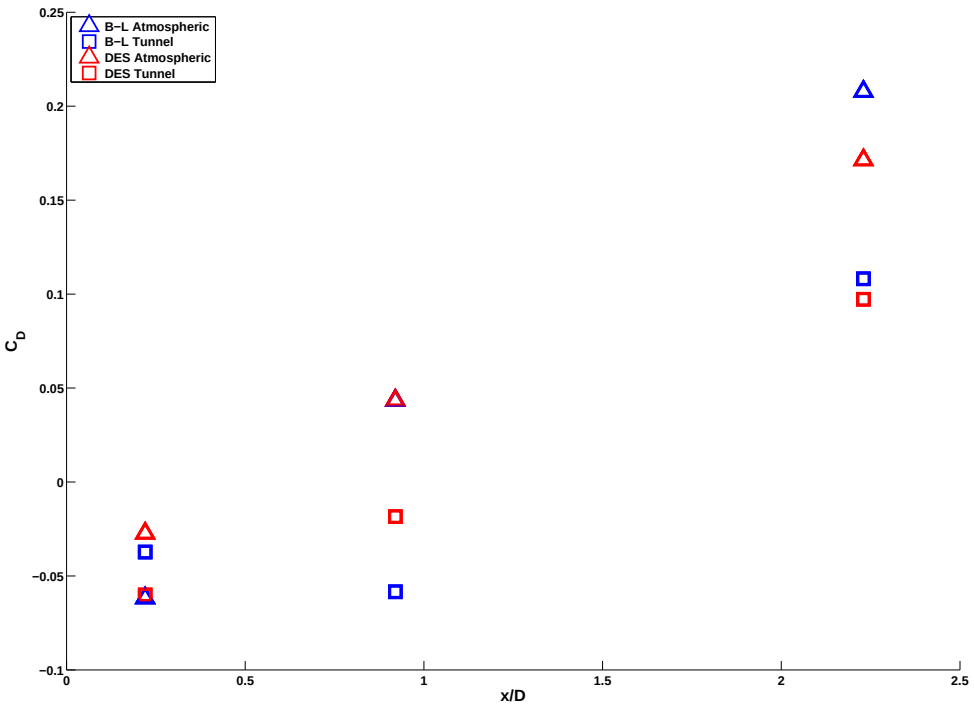

Figure 44: Turbulence model comparison of wind tunnel and atmospheric drag coefficients on store with a hollow carrier, Re = 3.9x10^8

0.22 x/D for wind tunnel and atmospheric cases. At 0.92 x/D the free flight case for both turbulence models has already transitioned to positive drag while the wind tunnel cases are still experiencing negative drag. The wind tunnel effects can therefore be shown to have a major impact on the store's drag between 0.22 and 0.92 x/D. It's clear that the encasement of the flow field in the wind tunnel causes this. Figure 45 shows pressure contour plots of both the atmospheric and wind tunnel cases overlayed in order to show difference in base pressures on the store. Orange-red colors are the wind tunnel pressure contours and bluish colors are atmospheric. The much denser distribution of blue pressure contours at the base of the store shows qualitatively the much stronger expansion which has formed at the base when the store is in the at-

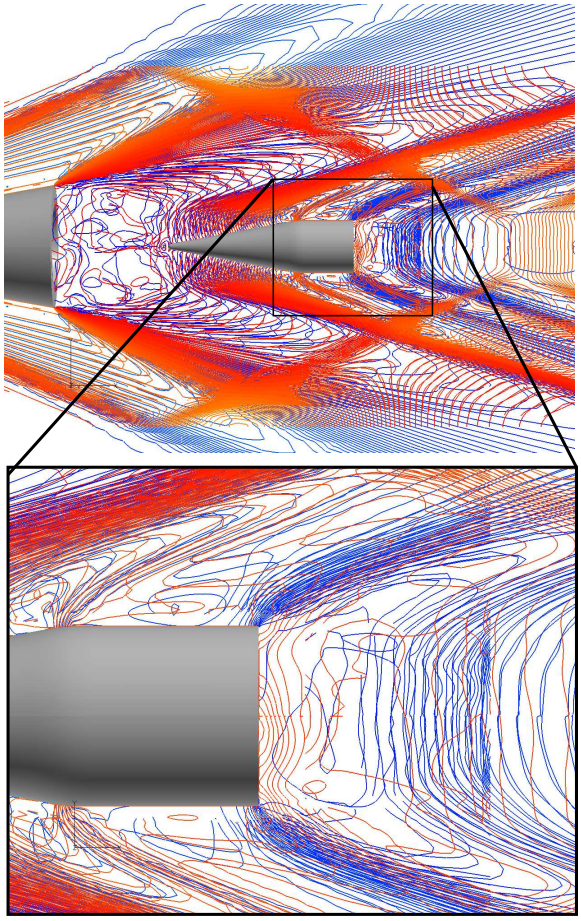

Figure 45: Expansion comparison using pressure contours on store at 0.22 x/D for free flight and wind tunnel (no-sting) cases

mosphere. The reattachment shock for the atmospheric case is also more prominent due to the stronger expansion region. The turbulence model used was DES for this comparison, but the B-L model also shows this wind tunnel effect based on drag data.

Looking at Figure 44, it is also apparent that the drag on the store is increasing as the store is brought away from the carrier. This is expected since the store is being pulled further away from the carrier and will eventually have supersonic flow turning at its base, giving it more base and skin friction drag. Skin friction will obviously have much less of an impact than base drag.

There are no discernable trends when comparing the two turbulence models in Figure 44 to show that one is more accurate than the other for force computing purposes. From what is already known of turbulence modelling, B-L is not supposed to be reliable for computing free shear layers or massively separated flows. This was shown to be the case when looking at the near-wake in Figures 18 and 23 where B-L was not able to simulate symmetry of the recirculation regions. From that standpoint, DES should be giving more accurate force and moment estimations.

As explained earlier, Chapman concluded from his experiments that if the boundary layer state before the base corner had already transitioned to turbulent, the effects of Reynolds number did not have a significant impact on base pressure. This should be the case for this CFD research, since the boundary layer on the carrier has transitioned to turbulent ($Re_L = 2.12\text{x}10^6$). The Reynolds number effects for high-Mach flow on the store is shown in Figure 46 for the B-L turbulence model with a cavity present on the carrier. This shows Reynolds number does not have a major impact on the drag experienced by the store for these CFD runs.

The effects of the cavity on the carrier are also of interest since there is no avoiding it in a dynamic separation. Figure 47 shows store drag coefficients with and without a cavity present on the carrier. The store has more drag when the carrier is solid for all cases (both turbulence model and flight environment) except the B-L wind tunnel runs at 0.22 and 0.92 x/D. Jung [16] found the presence of a cavity in

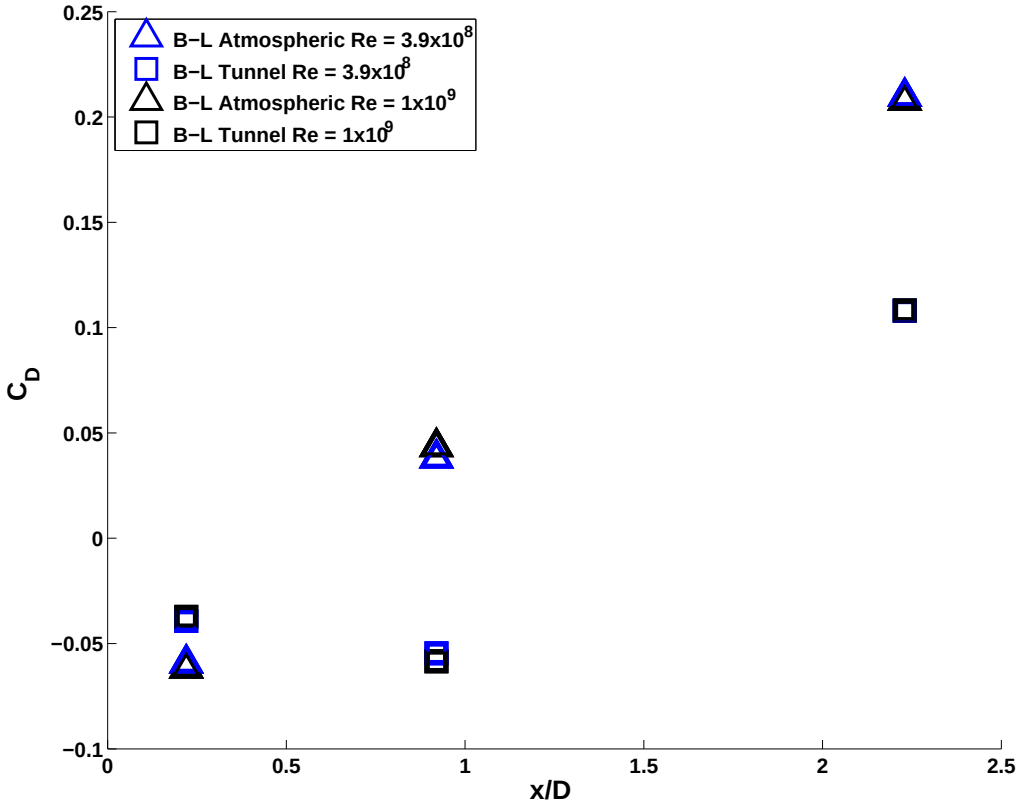

Figure 46: B-L turbulence model comparison of Reynolds number effects on store with cavity present

the carrier decreased the surface pressures on the frontal portion of the store. This would cause the store to have less drag, assuming the base pressures on the store are not significantly effected by the cavity. The lower surface pressures on the store can be explained by previous comparisons of u velocities in the near wake of the carrier, which showed the cavity caused a delayed reattachment. Since the rear stagnation point would be further aft, the velocities around the store would be less for the cavity case than the solid case. The drag decrease on the store due to the presence of a cavity are small in comparison to the effects the wind tunnel had when comparing to free flight drag data. In other workds, the reflected shocks have more of an impact on the drag measured on the store than the cavity's presence in the carrier. This is

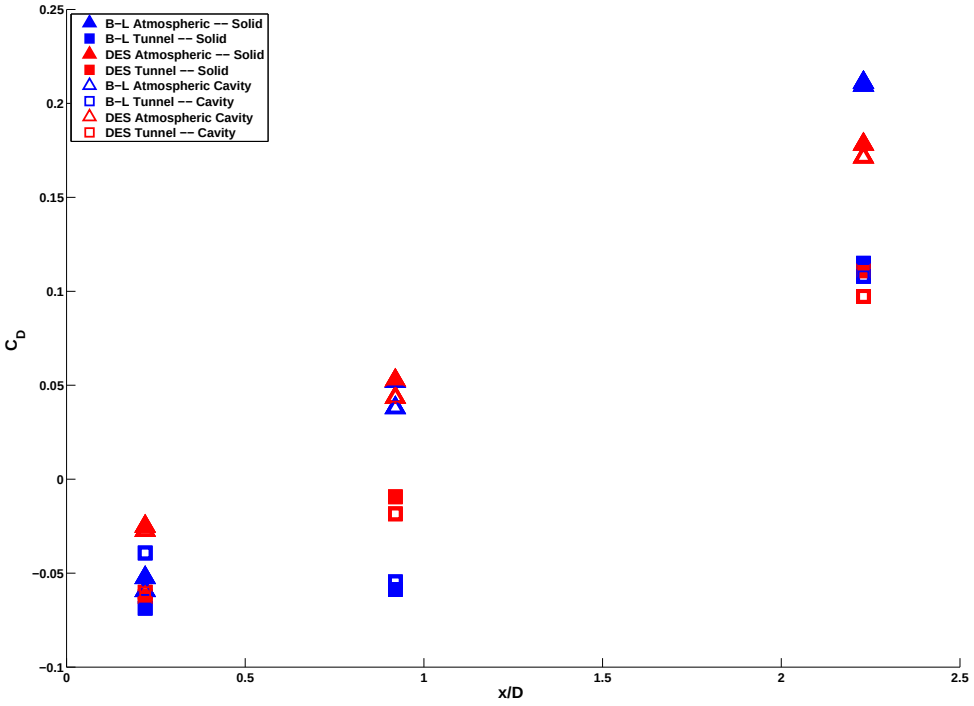

Figure 47: Comparison of cavity effects on store, $Re = 3.9\text{x}10^8$

expected since shocks will change inviscid properties in the areas of interest, which have a large impact on base drag.

4.6.2 Carrier Force and Moment Analysis. The carrier C_D values are important because they allow comparisons to drag data for the store. Since the carrier will most likely be at terminal velocity or decelerating, there could be a reconnect if the store separates back into the free stream and catches up with the carrier. This would obviously happen only if the store and carrier maintained the same path.

When the store is in the near-wake of the carrier, the shear layer will not be allowed to reattach as it was when the store was absent. Since the shear layer will turn into the centerline at a smaller angle, the expansions off of the carrier's base will be weaker. This should create lower drag for the lead vehicle since base pressures will be higher. Figure 48 shows drag comparisons on a hollow carrier in different

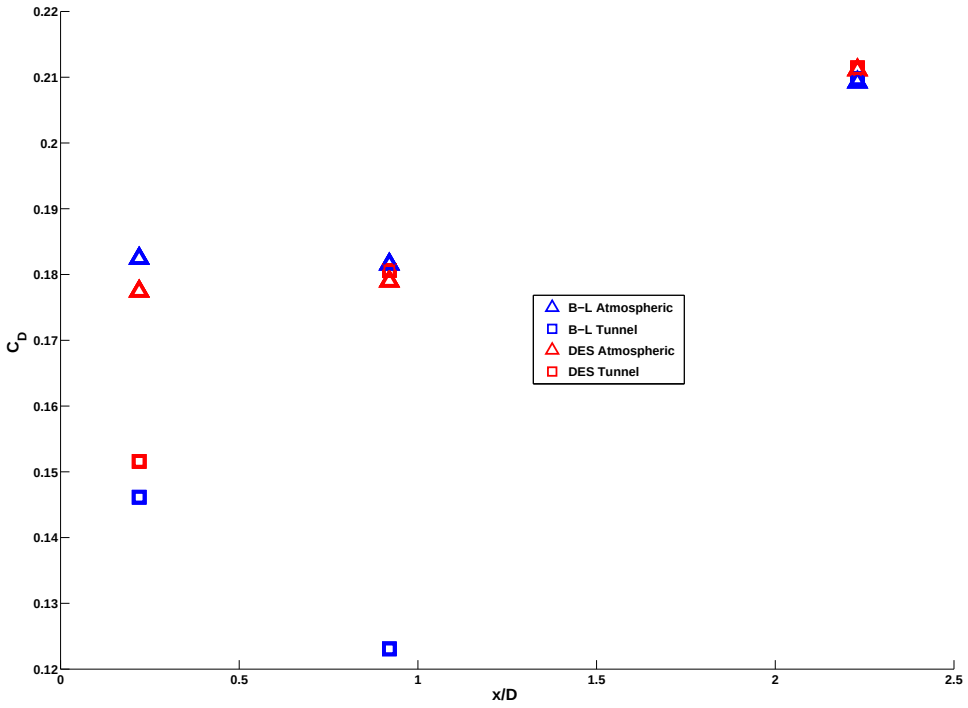

Figure 48: Comparisons of drag coefficient on the hollow carrier as a function of store position

environments. At 0.22 x/D, the drag on the carrier is higher in the atmosphere than in free flight. Figure 49 shows the difference in C_p with the store present using DES values. Values between -.005 and 0.005 have been removed. One can see the wind tunnel causes pressure differences in the near-wake with the store present, which was not the case when the same analysis was previously done without the store (Figure 25). The encasement of the flow is causing this to happen since all other variables in the simulation are identical. It is theorized that reflected shocks downstream are creating disturbances in the subsonic wake, which are then propogated back upstream to the carrier. Since the difference between atmospheric and wind tunnel C_p's is negative, the effect is higher drag on the atmospheric carrier.

From 0.22 to 0.92 x/D, the DES and wind tunnel cases have almost identical drag values, but the B-L case shows a drastic difference. Since effects in the wake are

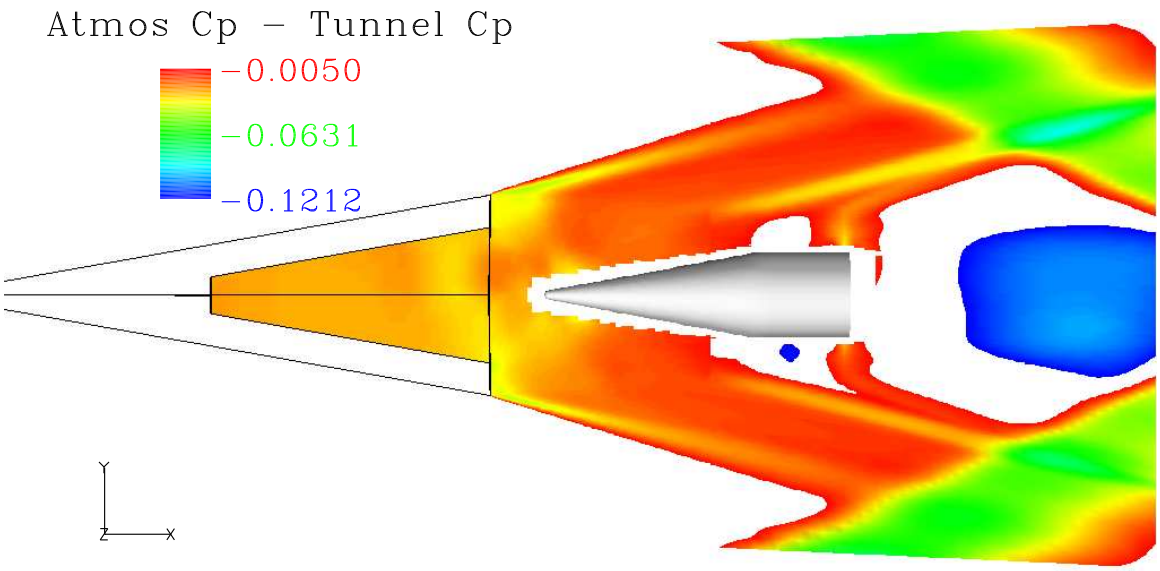

Figure 49: Difference in C_p between atmospheric and wind tunnel (with store at 0.22 x/D) cases using DES

less reliable using B-L, this was not studied in detail and are attributed to turbulence model error. The DES C_p comparison at 0.92 x/D is shown in Figure 50 and shows the pressures in the wake of the carrier agree more than when the store was at 0.22 x/D. This shows the store having less of an effect on the carrier as it is moved aft. At 2.23 x/D the drag values are nearly identical for all cases since the disturbances in the wake have all washed out so the flow has nearly returned to free stream conditions. The wind tunnel data point at 0.22 x/D for the B-L turbulence model was not looked into in more depth because we know that B-L results are not as accurate as the DES results. The trend in drag on the carrier for free flight cases does what is expected. As the store is brought away from the carrier, the shear layer can be turned into the centerline at a steeper angle, thus allowing a stronger expansion and higher base pressures.

Figure 51 shows the carrier drag coefficients relative to the store's drag coefficients. At the lowest separation distance, the frontal area of the store is completely

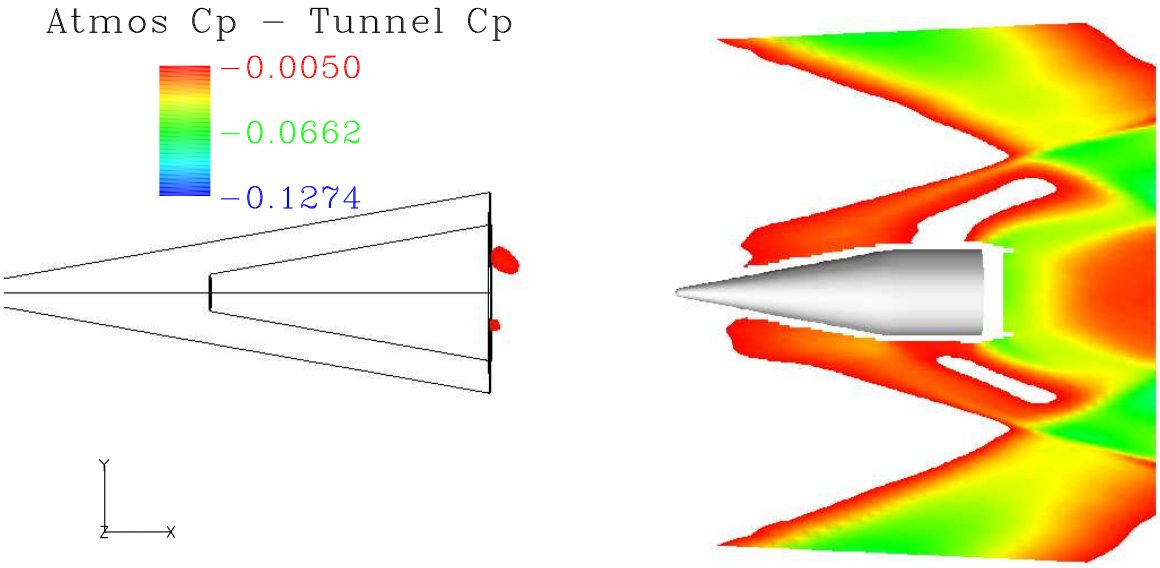

Figure 50: Difference in C_p between atmospheric and wind tunnel (with store at 0.92 x/D) cases using DES

blocked by the carrier so the store has less drag. As the store makes its way back into the freestream, the drag difference between the two gets smaller. In order to get a better idea of the drag relations, Table 3 shows the differences in drag coefficient between the carrier and store normalized by the carrier's drag coefficient for that respective case. A value of 1 would mean the store has no drag and a zero value would mean the store has the same drag as the carrier. As one can see, at 0.22 x/D the store has values greater than 1 because this is the station where all cases showed the store being pulled back towards the carrier. At 0.92 x/D, the atmospheric cases transition to positive drag and the tunnel cases remain in a suction state. At 2.23 x/D, various results are seen. The B-L cases in free flight show nearly the same drag as the carrier.

Table 3: Drag differences normalized by carrier vehicle drag coefficient

	B-L, Re =1.0x10^9/m		B-L, Re =3.9x10^8/m		DES, Re =3.9x10^8/m	
	Atmos	Tunnel	Atmos	Tunnel	Atmos	Tunnel
x/D = 0.22	1.34	1.28	1.34	1.26	1.15	1.40
x/D = 0.92	0.78	1.47	0.76	1.47	0.76	1.10
x/D = 2.23	-0.02	0.48	0.01	0.48	0.19	0.54

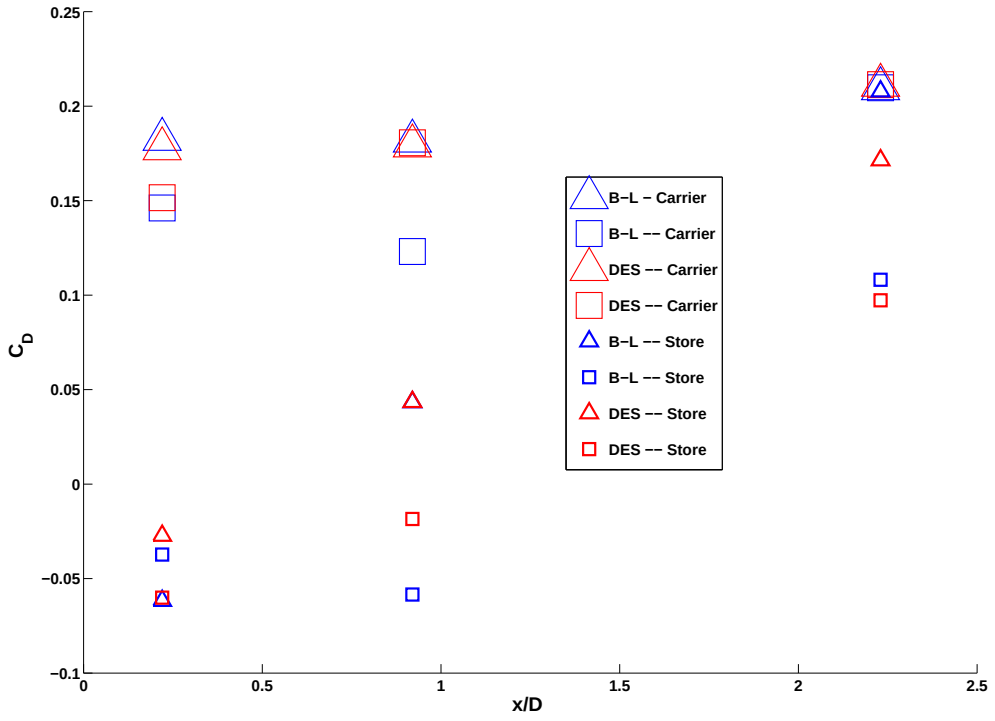

Figure 51: Comparisons of store and carrier drag coefficients

Interestingly, the B-L case with a higher Reynolds number has achieved drag greater than the carrier's and is denoted by the negative value for the normalized drag difference. Generally speaking, this shouldn't happen since the store is in the carrier's wake and the flow around it should never reach greater than freestream speeds. Since B-L cases show the store's drag is nearly the same as the carrier's at far separation distances, the turbulence model is probably washing out any wake that may have developed off of the carrier so freestream conditions are once again achieved. This seems possible since B-L is not suited for separated flows. DES however, does not show the drag on the store to be as high as the carrier's. The difference is related to each turbulence model's ability to compute separated flows.

4.6.3 Drag on Store With Sting. In future wind tunnel experimentation, it may be worth while to take drag data from the store if one can quantify the effects the

sting has on force measurements. The data presented in this section is for cases where the cavity is present on the carrier. Figure 52 shows the drag measurements on the store with the sting present compared to the previous results in the atmosphere and wind tunnel without a sting. Sting cases have significantly higher drag coefficients

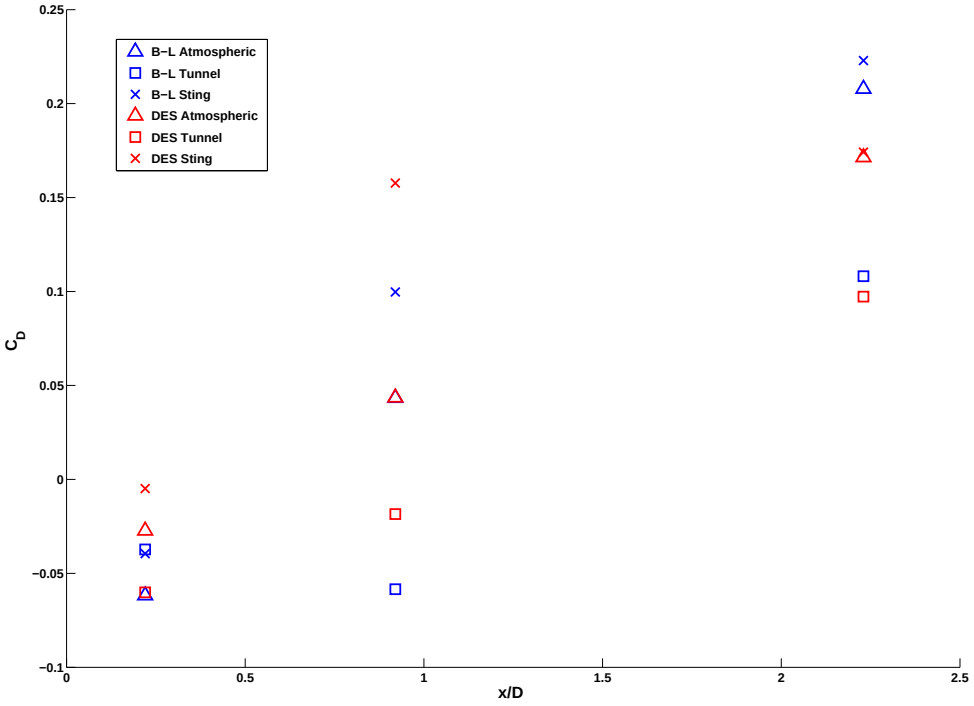

Figure 52: Store C_D comparisons for all test environments

than all wind tunnel cases without a sting and most atmospheric cases. There are no quantifiable trends that can be used to describe what differences the addition of the sting causes. However, in a previous analysis the Mach number at the base of the carrier with a sting was shown to be greater than the wind tunnel case without a sting. This would carry through the wind tunnel so that the store would have a larger Mach number around it, which would cause higher drag. The wind tunnel case without a sting should be the baseline for this since the wind tunnel encasement is already taken into account. Interestingly, most of data the in Figure 52 shows the

sting cases match up more closely with the atmospheric cases than the no-sting wind tunnel runs.

Also of interest, are force and moment coefficient differences along other axes. Force data along the z axis (lateral forces) and moment data about the y axis (yaw) are still negligible since symmetry is still maintained. These plots are included in Appendix A for reference. The force data along the y axis (vertical) and the moment data about the z axis (pitch) are expected to change due to asymmetric flow. The y forces on the store with the sting present are shown in Figure 53 with the atmospheric and no-sting wind tunnel data. Atmospheric and no-sting data are close to zero as expected. As the store is moved in the aft direction, the variation between symmetric test case results grow. All differences of the sting case to symmetric cases are negative, with the furthest deviation occurring at 0.92 x/D. The y force coefficient is 74% of the drag coefficient at 0.92 x/D. The y forces can therefor by considered to be significantly effected by the sting's presence. Figure 54 shows surface pressure coefficients for the store at 0.92 x/D. The top surface pressures have a greater net pressure than the surface pressures acting on the bottom, even though the zone of highest pressure is found on the bottom.

Figure 55 shows the moments about the z axis for the sting cases compared to symmetric cases. The atmospheric and wind tunnel data are close to zero as expected. At 0.22 x/D, the C_{Mz} for the sting is negligible. As the store is moved further aft, C_{Mz} grows larger and is positive. A positive C_{Mz} value is attributed to a nose down pitching moment. The C_{Fy} on the store at 0.92 x/D previously studied showed the top portion had higher pressures on the frontal surface than the bottom surface in Figure 54, which would cause a nose down pitching moment.

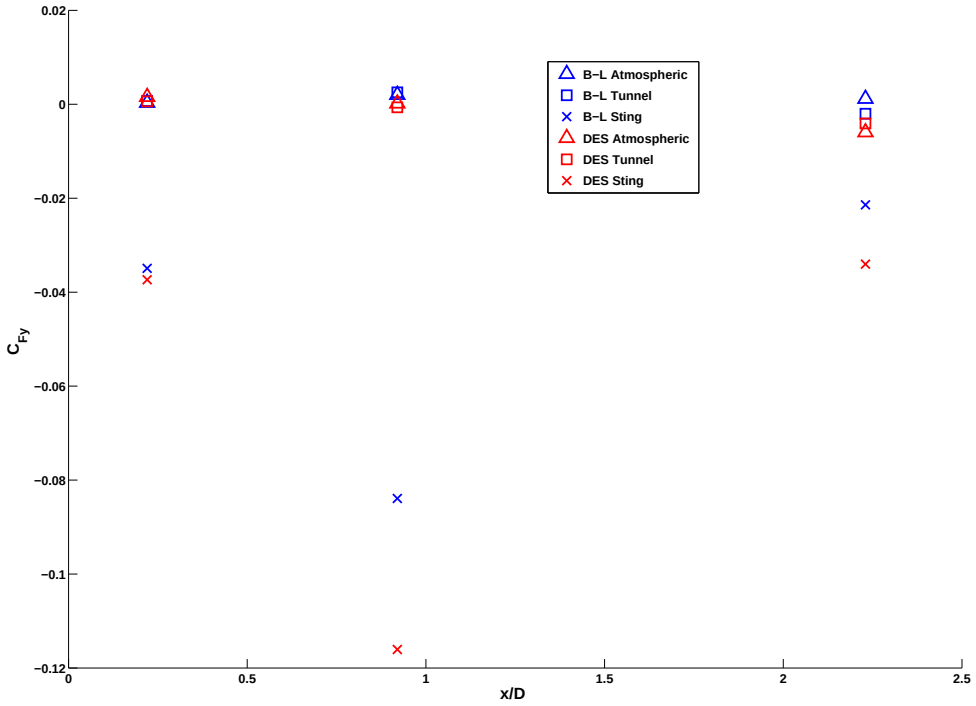

Figure 53: Store C_{Fy} Comparisons for all test environments

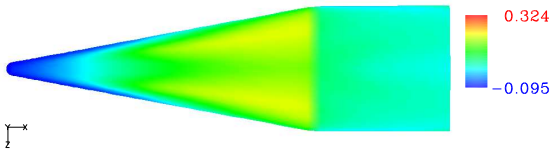

(a) Top

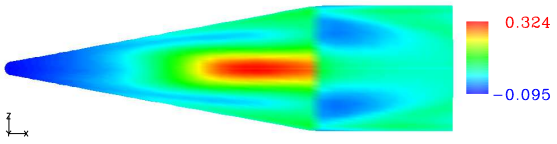

(b) Bottom

Figure 54: C_p on the top and bottom of the store at 0.92 x/D using DES

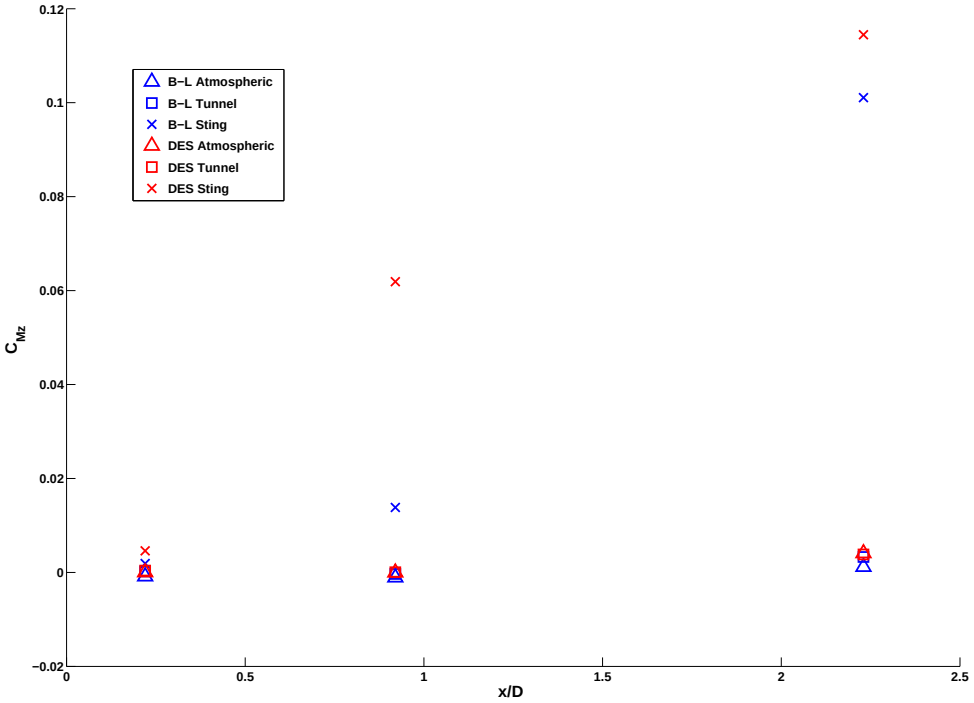

Figure 55: Store C_{Mz} comparisons for all test environments

V. Conclusions and Recommendations

5.1 Conclusions

This thesis summarizes results of a CFD analysis of the environments a store will pass through when it is ejected from the rear of a supersonic carrier. The fundamental elements of understanding this phenomena rely on base pressures, near wake studies and force/moment analyses on both the carrier and store. Experimental results also provided a unique way to compare flow structures and pressure data in order to validate computational results.

Turbulence models available for Beggar were compared. From earlier studies, it was found that the S-A turbulence model was not suitable for base flow research due to its tendency to dissipate unsteady solutions to steady state, which also led to inaccurate base pressure calculations on the carrier. The B-L and DES turbulence models computed mean base pressures with reasonable accuracy when compared to theoretical and empirical models. Differences were seen between the turbulence models once the flow was past the carrier's base. These differences were magnified significantly when the sting was added to the flow. The B-L turbulence model computed much higher base pressures than DES with the sting present. Since DES is historically proven to be satisfactory at capturing shear layers and separated flow while B-L is not, it can be concluded that B-L solutions with the sting present are unreliable. For a quick computation of mean base pressure in a symmetric environment, however, the B-L turbulence model gives valid approximations.

The presence of the wind tunnel caused little change in the near-wake when compared to free flight values. Mean base pressure deviations from atmospheric cases were less than 0.5% for the B-L turbulence model and negligible for the DES turbulence model. In the near-wake, differences in the main flow features (rear stagnation point and maximum reverse velocity) were negligible. Symmetry was maintained in the near-wake. A visual comparison of pressure differences showed the inviscid features of the flow remain the same until the conical shock from the carrier is reflected off of the tunnel wall. This is significant because all changes between the sting and

no-sting wind tunnel cases in the near-wake can be attributed to the presence of a sting. Drag studies on the store showed the wind tunnel had an effect outside of the near wake. When clean wind tunnel cases were compared to free flight data, the store remained in a "suction" state longer than atmospheric cases did. This is significant because experimental efforts to record drag on the store will remain difficult even if a mount is placed in the wind tunnel that does not impinge on the flow. It's important to accurately model this transition because it will have implications on dynamic separations.

As previously mentioned, the presence of a sting changed average base pressure calculations on the carrier. In addition to this, the base pressure profile and near-wake was void of symmetry due to the sting. Force and moment data on the store showed that the sting caused significant changes in drag as well as y forces and z moments. The three-dimensional nature of the shock interactions showed that two-dimensional views of the test section were not sufficient to analyze everything that is happening in the wind tunnel. The shock interactions come from multiple angles and are too complex to quantify. It is concluded that the sting has implications on the flow passing the carrier.

5.2 Recommendations

5.2.1 Experimental. The present CFD thesis along with the experimental studies were initial efforts to lay groundwork for future work relating to supersonic store separations. Since CFD depends heavily on experimental testing for validation, and vice versa, the most immediate recommendation would be to correct the asymmetry in the wind tunnel environment. This could be accomplished by redesigning the sting or wind tunnel to be better suited for axisymmetric flow as Jung recommended in his thesis.

5.2.2 CFD. Running more x/D cases can be done immediately following this thesis. Jung was able to run many more than three cases so there is more data

available for comparison. Also, there are large distances between the store separation distances in the current CFD study that need to be filled. For instance, when the store was between 0.22 and 0.92 x/D (atmospheric), it transitioned from negative drag to positive drag somewhere in between. It would be beneficial to determine the exact x/D where the drag becomes positive and whether the change is subtle or abrupt. An abrupt change may have implications on dynamic store separations.

One aspect not covered in detail by this thesis is a time step study. Due to time constraints and available computer resources, an in depth study of the time step was not performed. Previous works using LES and DES (unstructured) used time steps on the order of 10^{-7} and 10^{-6} to produce results which they considered to be valid [13, 14]. For the current research the dt was $2.5\text{x}10^{-4}$, which may have been too high to capture smaller frequency oscillations due to turbulence. Since the present work is more interested in mean values, the time step will probably not make a major difference in the forces and moments computed, but it is worth investigating.

Another aspect of this thesis which can be studied in more detail is the effect of grid oversetting on the flow solver. By oversetting grids, the equations which govern the flow are no longer conservative at the interpolation points. This can have a major effect on the solution if the cells interpolating from one another have different cell sizes. There are ways to limit this effect during static runs with cutting methods and settings in Beggar, but the most one can do during a dynamic separation is to design grids in a way that will minimize these effects as one is passed through the other.

There is obviously much left to do in order to produce a dynamic store separation. Most of this has to do with finding valid inertial properties for a store and defining them in Beggar. Ejection forces must be large enough to be able to successfully clear the store from the carrier. The AFSEO office has data pertaining to external weapons releases that can provide a baseline ejection force to use for initial dynamic simulations. Applying constraints on the store as it leaves the cavity may

also be needed so the store does not collide with the cavity on its way out. This can all be done in the input deck of Beggar.

Appendix A. Forces and Moments

A.1 Tables of Forces/Moments

Table 4: B-L - Store with Solid Carrier - Re = $1.0x10^9$/m

Atmospheric						
x/D	CFx	CFy	CFz	CMx	CMy	CMz
0.22	-0.052445	0.0014612	0.00073306	0	0.000277	2.2047e-005
0.92	0.051928	0.0064112	0.001173	0	-0.00039105	-0.001318
2.23	0.2111	0.0080393	0.0012438	0	0.0026302	-0.0092938
Wind Tunnel - No Sting						
0.22	-0.06861	-0.0033121	-0.010858	0	-0.0059985	0.00079602
0.92	-0.058703	0.00043263	0.0001018	0	5.7356e-005	0.0011343
2.23	0.11496	0.00012074	0.0012199	0	-0.0041465	0.0035841
Wind Tunnel - Sting						
0.22	-0.025392	-0.040847	0.0020154	0	-0.0017412	0.0069004
0.92	0.096358	-0.085526	0.0016003	0	0.0026811	0.010224
2.23	0.21996	-0.0079025	-0.005707	0	-0.014027	0.078847

Table 5: B-L - Store with Hollow Carrier - Re = $1.0x10^9$/m

Atmospheric						
x/D	CFx	CFy	CFz	CMx	CMy	CMz
0.22	-0.059356	-0.0017508	-0.0013293	0	-0.00076038	-0.00011222
0.92	0.037987	0.0021318	-0.0018938	0	-0.00016378	-0.0023763
2.23	0.20964	-0.002495	-0.0035224	0	-0.0015678	-0.00063986
Wind Tunnel - No Sting						
0.22	-0.039281	-0.0036121	-0.00041752	0	0.00081193	-0.00019561
0.92	-0.054634	-0.0023865	0.00053494	0	-0.0020897	0.00097306
2.23	0.10796	-0.002264	-0.001906	0	-0.0012999	0.0024951
Wind Tunnel - Sting						
0.22	-0.030094	-0.032304	0.00050056	0	-0.00054438	0.0037651
0.92	0.097546	-0.082526	0.00076164	0	0.0013931	0.0088596
2.23	0.20741	-0.020363	-0.0036233	0	-0.007195	0.11108

Table 6: B-L - Hollow Carrier - Re = $1.0x10^9$/m

Atmospheric						
x/D	CFx	CFy	CFz	CMx	CMy	CMz
0.22	0.17515	2.142e-005	1.4551e-005	0	-0.00021454	0.00013759
0.92	0.17178	8.2844e-005	-9.6298e-006	0	0.00021033	0.00014663
2.23	0.20554	-0.00015421	-9.3711e-005	0	-8.8545e-005	4.6824e-005
Wind Tunnel - No Sting						
0.22	0.14206	7.0559e-005	0.00016368	0	-0.00030358	5.9506e-005
0.92	0.11733	-1.095e-005	-2.7954e-005	0	-3.9545e-005	-1.5908e-005
2.23	0.20571	6.1631e-006	3.0898e-005	0	0.00042577	-0.0001554
Wind Tunnel - Sting						
0.22	0.010271	-0.028234	0.00013878	0	0.00023735	-0.0015174
0.92	0.18317	-0.082668	-2.5918e-005	0	0.00014715	-0.069691
2.23	0.20994	-0.082712	-2.1626e-005	0	0.00013304	-0.069596

Table 7: B-L - Hollow Carrier - Re = $3.9x10^8$/m

Atmospheric						
x/D	CFx	CFy	CFz	CMx	CMy	CMz
0.22	0.18246	3.5052e-005	0.00010871	0	-0.00030593	3.1666e-005
0.92	0.18157	-0.00013493	-4.493e-005	0	3.6619e-005	-0.00035261
2.23	0.20926	-2.977e-005	-2.7569e-005	0	0.0002868	-0.0004834
Wind Tunnel - No Sting						
0.22	0.14614	-4.4517e-005	-6.2814e-005	0	7.8941e-005	3.7894e-005
0.92	0.12308	3.7006e-005	4.8259e-005	0	4.825e-005	2.7089e-005
2.23	0.20975	-5.1506e-005	-5.5715e-005	0	0.00030391	-0.00024905
Wind Tunnel - Sting						
0.22	0.19046	-0.082996	5.6596e-005	0	7.2712e-005	-0.071051
0.92	0.18894	-0.082573	-1.1088e-005	0	0.00017311	-0.070561
2.23	0.21638	-0.082625	6.1355e-006	0	0.00015008	-0.070573

Table 8: DES - Store with Solid Carrier - Re = $3.9x10^8$/m

Atmospheric						
x/D	CFx	CFy	CFz	CMx	CMy	CMz
0.22	-0.025069	5.0056e-006	-0.00021065	0	-4.7575e-005	-0.0001729
0.92	0.052608	-0.0013617	0.0030202	0	-0.00062942	-0.0035285
2.23	0.17823	-0.0038815	0.002085	0	-0.0015108	0.0038707
Wind Tunnel - No Sting						
0.22	-0.062478	0.006919	-0.025835	0	-0.01009	-0.0039303
0.92	-0.0093688	-0.0058463	-5.8617e-005	0	0.0012205	0.0018168
2.23	0.11088	0.0064157	-0.00043174	0	-0.0037027	-0.0068432
Wind Tunnel - Sting						
0.22	0.005042	-0.043723	0.0091594	-8.5204e-005	0.0022253	0.011512
0.92	0.15631	-0.10702	0.0014932	3.2325e-005	0.00081309	0.055318
2.23	0.16952	-0.033413	-0.00064389	0	-0.0067136	0.11637

Table 9: DES - Store with Hollow Carrier - Re = $3.9x10^8$/m

Atmospheric						
x/D	CFx	CFy	CFz	CMx	CMy	CMz
0.22	-0.027288	0.0015627	0.00060638	0	-0.00037977	3.5474e-005
0.92	0.043529	0.00016018	-0.0024851	0	-0.0016734	-2.4865e-005
2.23	0.1714	-0.0059615	0.0035849	0	0.0013028	0.0040946
Wind Tunnel - No Sting						
0.22	-0.060109	0.00062537	-0.00026272	0	-0.00035557	0.00039734
0.92	-0.018441	-0.00065358	-0.00077727	0	-0.0013455	4.3928e-005
2.23	0.097267	-0.004085	0.0046031	0	0.0035434	0.0038236
Wind Tunnel - Sting						
0.22	-0.0048539	-0.037354	0.0027615	0	0.00076393	0.0046014
0.92	0.15769	-0.11606	0.00032316	0	0.00026142	0.061897
2.23	0.17416	-0.034037	0.0017352	0	-0.0032162	0.11447

Table 10: DES - Solid Carrier - Re = $3.9x10^8$/m

Atmospheric						
x/D	CFx	CFy	CFz	CMx	CMy	CMz
0.22	0.17712	0	0	0	2.4162e-005	-5.4103e-005
0.92	0.17849	-3.7776e-005	3.8794e-006	0	0.00076179	0.0014884
2.23	0.21339	0	2.8339e-005	0	0.00056564	-0.0002991
Wind Tunnel - No Sting						
0.22	0.17918	0	2.4267e-005	0	0.0011365	0.0003869
0.92	0.17997	2.5588e-006	-8.8044e-007	0	-0.00084268	-0.00039328
2.23	0.21379	1.1005e-006	-2.7679e-005	0	0.00042885	0.00054816
Wind Tunnel - Sting						
0.22	0.19157	-0.086206	5.4147e-005	0	-0.00029318	-0.077322
0.92	0.21199	-0.086191	5.5027e-005	0	0.00019322	-0.077651
2.23	0.22268	-0.0862	5.5027e-005	0	0.0001876	-0.077398

Table 11: DES - Hollow Carrier - Re = $3.9x10^8$/m

Atmospheric						
x/D	CFx	CFy	CFz	CMx	CMy	CMz
0.22	0.17746	-0.00015614	-0.00019917	0	0.00060609	-0.00044738
0.92	0.17899	-1.1886e-005	6.7298e-005	0	-0.00033355	-0.00016756
2.23	0.2111	2.2301e-005	6.3195e-005	0	0.00019131	0.00012527
Wind Tunnel - No Sting						
0.22	0.15159	-1.9947e-005	-0.00011459	0	3.1141e-005	-0.00020846
0.92	0.18062	-0.00028372	0.00024757	0	-0.00022256	-0.00023254
2.23	0.21142	-0.00016657	-2.4047e-005	0	6.4083e-005	-0.00026308
Wind Tunnel - Sting						
0.22	0.19002	-0.086503	0.00012734	0	-1.6429e-005	-0.077788
0.92	0.21171	-0.086049	2.5808e-005	0	0.00019262	-0.077758
2.23	0.22294	-0.086173	8.7769e-006	0	0.00025536	-0.077522

A.2 Plots of Forces/Moments

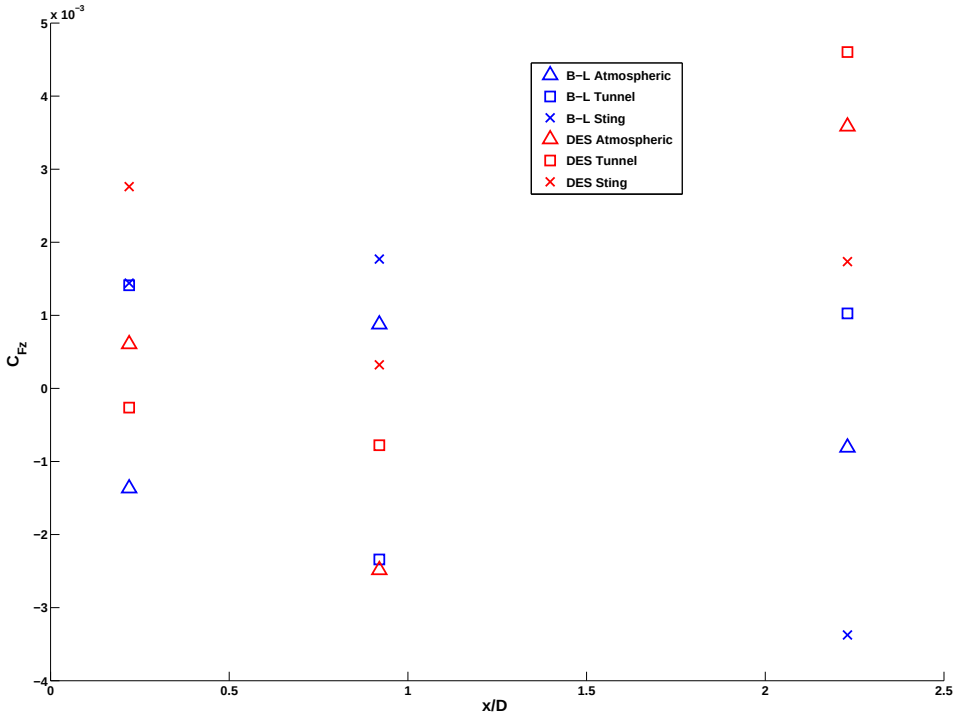

Figure 56: Store C_{Fz} Comparisons for all test environments

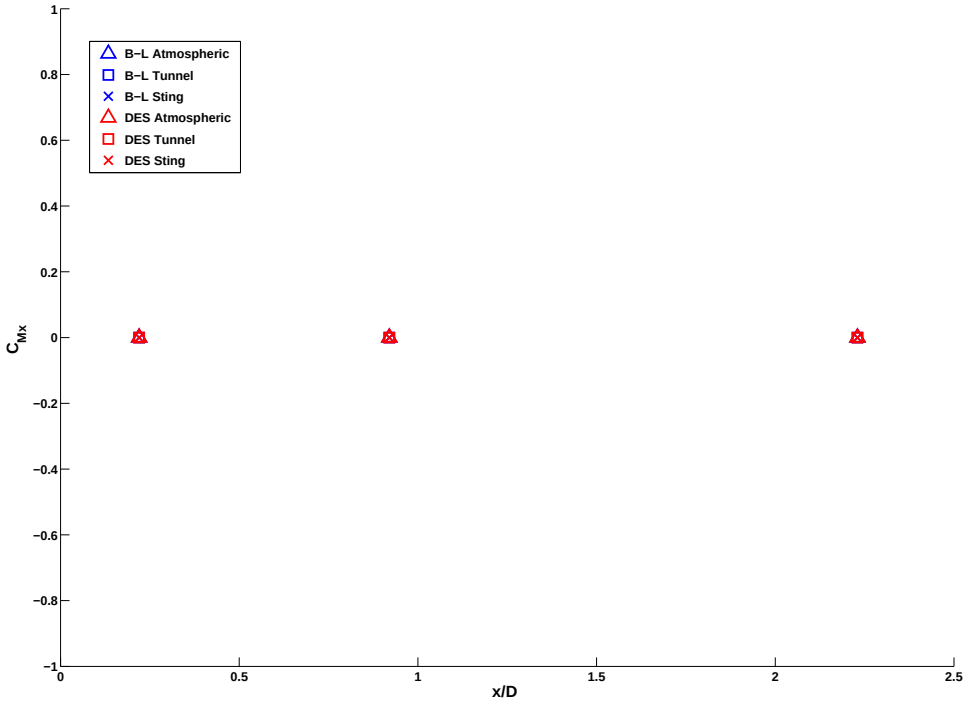

Figure 57: Store C_{Mx} Comparisons for all test environments

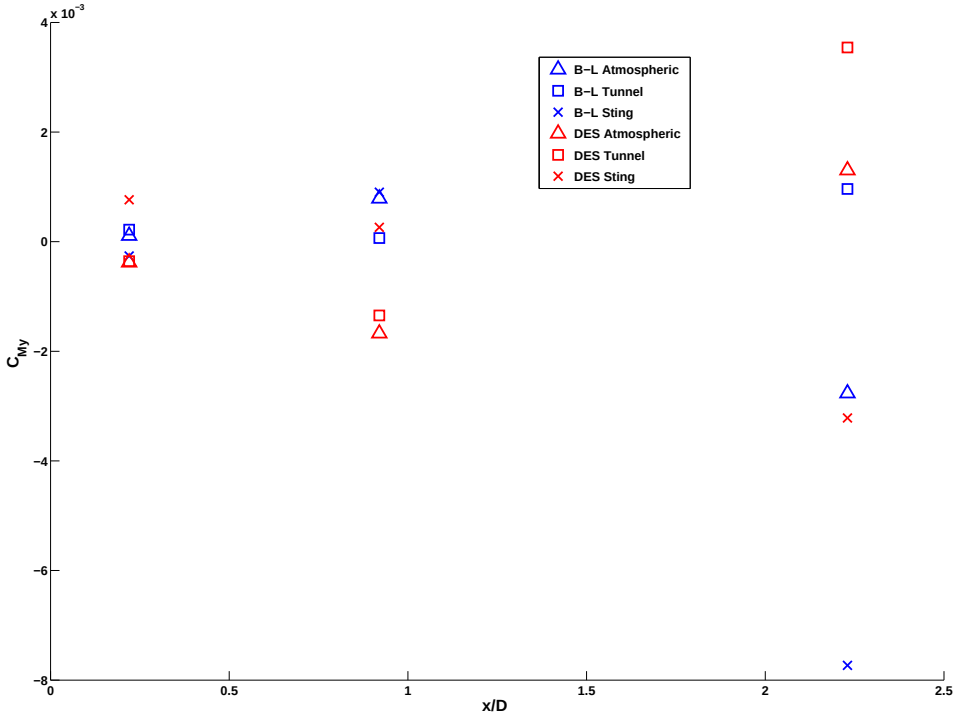

Figure 58: Store C_{My} Comparisons for all test environments

Bibliography

1. "Beggar Version 110C+ User's Manual," May 2005. Air Force SEEK Eagle Office Computational Aeromechanics Team.

2. Anderson J. D. *Modern Compressible Flow* (3rd Edition). Boston: McGraw-Hill, 2003.

3. August H., Hardy F. W., Floyd J. Wilcox J., and Pinney M. *Leeside Separation of Hypersonic Weapons*. Technical Report ADA318744, Tuscon, AZ: Hughes Aircraft, 1993.

4. Baldwin B. and Lomax H. *Thin-Layer Approximation and Algebraic Model for Separated Turbulent Flows*. Technical Report 78-0257, AIAA, Jan 1978.

5. Bjorge S. T., Reeder M. F., Subramanian C., and Crafton J. *Flow Around an Object Projected From a Cavity into a Supersonic Freestream*. Technical Report 04-1253, Reno, NV: AIAA, Jan 2004.

6. Blazek J. *Computational Fluid Dynamics: Principles and Applications*. Oxford, UK: Elsevier Science LTD, 2001.

7. Boswell B. A. and Dutton C. "Flow Visualizations and Measurements of a Three-Dimensional Supersonic Separated Flow," *AIAA Journal*, *39*(1):113–121 (Jan 2001).

8. Boswell B. A. and Dutton C. "Velocity Measurements in a Three-Dimensional Compressible Base Flow," *AIAA Journal*, *41*(5):785–794 (May 2003).

9. Bulmer B. M. "Study of Base Pressure in Laminar Hypersonic Flow: Re-entry Flight Measurements," *AIAA Journal*, *13*(10):1340–1348 (Jun 1975).

10. Bulmer B. M. "Fight-Test Base Pressure Measurements in Turbulent Flow," *AIAA Journal*, *14*(12):1783–1785 (Sep 1976).

11. Chapman D. R. *An Analysis of Base Pressure at Supersonic Velocities and Comparison With Experiment*. Technical Report 1051, NACA, 1951.

12. Dutton J., Herrin J., Molezzi M., T.Mathur , and Smith K. *Recent Progress on High-Speed Separated Base Flows*. Technical Report 95-0472, Reno, NV: AIAA, Jan 1995.

13. Forsythe J. R., Hoffman K. A., and Dietiker J.-F. *Detached-Eddy Simulation of a Supersonic Axisymmetric Base Flow with an Unstructured Solver*. Technical Report 00-2410, Denver, CO: AIAA, Jun 2000.

14. Fureby C., Nilsson Y., and Anderson K. *Large Eddy Simulation of Supersonic Base Flow*. Technical Report 99-0426, Reno, NV: AIAA, Jan 1999.

15. Herrin J. and Dutton J. "Supersonic Base Flow Experiments in the Near Wake of a Cylindrical Afterbody," *AIAA Journal*, *32*(1):113–121 (Jan 1994).

16. Jung T. P. *Wind Tunnel Study of Interference Effects Relating to Aft Supersonic Ejection of a Store*. MS thesis, Graduate School of Engineering, Air Force Institute of Technology (AETC), Wright-Patterson AFB, OH, Dec 2005. AFIT/GAE/ENY/05-04.

17. Kawai S. and Fujii K. *Computational Study of a Supersonic Base Flow Using LES/RANS Hybrid Methodology*. Technical Report 04-0068, AIAA, Aug 2004.

18. Korst H., Page R., and Childs M. "A Theory for Base Pressures in Tansonic and Supersonic Flow." Contract no. AF 18 (600)-392, Univ of Illinois, 1955.

19. Lamb J. P. and Oberkampf W. L. "A Review and Development of Correlations for Base Pressure and Base Heating in Supersonic Flow." Prepared by Sandia National Laboratories, 1993.

20. Lee J. M., Dunworth K. S., Rizk M., Westmoreland W. S., and Atkins D. J. *Studies of Combined Use of CFD and Wind Tunnel Test Approaches to Simulate a Store Separation from F-15E Using Efficient CFD Database Generation*. Technical Report 04-4724, Providence, RI: AIAA, Aug 2004.

21. Mathur T. and Dutton J. *Base Bleed Experiments With a Cylindrical Afterbody in Supersonic Flow*. Technical Report 1995-62, Reno, NV: AIAA, Jan 1995.

22. Newman G. and Fulcher K. *On the Aerodynamics/Dynamics of Store Separation From a Hypersonic Aircraft*. Technical Report 92-2722, Palo Alto, CA: AIAA, Jun 1992.

23. Nichols R. "Turbulence Models and Their Application to Complex Flows." HPCMP/PET CFD Onsite, Contract no. N62306-01-D-7110.

24. Prewitt N. C., Belk D. M., and Maple R. C. "Multiple-Body Trajectory Calculations Using the Beggar Code," *Journal of Aircraft*, *36*(5):802–808 (Sep 1999).

25. Prewitt N. C., Belk D. M., and Shyy W. "Improvements in Parallel Chimera Grid Assembly," *AIAA Journal*, *40*(3):497–500 (Mar 2002).

26. Rizk M., Ellison S., and Prewitt N. C. *Beggar - A Store Separation Predictive Tool*. Technical Report 2002-3190, St. Louis, MO: AIAA, Jun 2002.

27. Schlicting H. and Gersten K. *Boundary Layer Theory* (8th Edition). Berlin, Germany: Springer, 2000.

28. Spalart P. and Allmaras S. *A One-Equation Turbulence Model for Aerodynamic Flows*. Technical Report 92-0439, Reno, NV: AIAA, Jan 1992.

29. Storm K. G. *Validation of Turbulence Models for the Beggar Code in Unsteady Flows*. MS thesis, Graduate School of Engineering, Air Force Institute of Technology (AETC), Wright-Patterson AFB, OH, Mar 2005. AFIT/GAE/ENY/05-M22.

30. Tannehill J. C., Anderson D. A., and Pletcher R. H. *Computational Fluid Mechanics and Heat Transfer* (2nd Edition). Philadelphia, PA: Taylor & Francis, 1997.

31. van Raalte M. and van Oudheusden B. *An Analytical Model to Describe the Reynolds Number Effects in a Supersonic Base Flow*. Technical Report 01-2785, Anaheim, CA: AIAA, Jun 2001.

32. Wilcox D. C. *Turbulence Modeling: An Overview*. Technical Report 01-0724, Reno, NV: AIAA, Jan 2001.

Vita

Lt Simko graduated from Slidell High School in Slidell, Louisiana in 1998. He then attended the United States Air Force Academy and graduated in May 2002 with a Bachelor of Science degree in Aeronautical Engineering. Upon his commission into the Air Force from the Air Force Academy, he spent his first assignment in the Air Force Research Laboratory where he worked with engineering level aircraft simulations for the Air Vehicles Directorate. In August 2004, he entered the Graduate School of Engineering and Management, Air Force Institute of Technology. Upon graduation in March 2006, he will be assigned to the Space and Missile Systems Center, Los Angeles Air Force Base, California.

REPORT DOCUMENTATION PAGE

Form Approved
OMB No. 074-0188

1. REPORT DATE *(DD-MM-YYYY)*	**2. REPORT TYPE**	**3. DATES COVERED** *(From – To)*
23-03-2006	**Master's Thesis**	Aug 2004 – Mar 2006

4. TITLE AND SUBTITLE

Store Separations from a Supersonic Cone

5a. CONTRACT NUMBER

5b. GRANT NUMBER

5c. PROGRAM ELEMENT NUMBER

6. AUTHOR(S)

Simko, Richard J., 1st Lt, USAF

5d. PROJECT NUMBER
JON # 05-304

5e. TASK NUMBER

5f. WORK UNIT NUMBER

7. PERFORMING ORGANIZATION NAMES(S) AND ADDRESS(S)

Air Force Institute of Technology
Graduate School of Engineering and Management (AFIT/EN)
2950 Hobson Way
WPAFB OH 45433-7765

8. PERFORMING ORGANIZATION REPORT NUMBER

AFIT/GAE/ENY/06-M29

9. SPONSORING/MONITORING AGENCY NAME(S) AND ADDRESS(ES)

AFRL/VAAI
Attn: Mr. Rudy Johnson
2130 8th Street
WPAFB OH 45433-7765 DSN: 785-3037

10. SPONSOR/MONITOR'S ACRONYM(S)

11. SPONSOR/MONITOR'S REPORT NUMBER(S)

12. DISTRIBUTION/AVAILABILITY STATEMENT

APPROVED FOR PUBLIC RELEASE; DISTRIBUTION UNLIMITED.

13. SUPPLEMENTARY NOTES

14. ABSTRACT

The purpose of this research was to analyze the environment a store would travel through if ejected from a supersonic cone. This was done using the Beggar Computational Fluid Dynamics (CFD) code from the Air Force SEEK Eagle Office at Eglin Air Force Base, FL. CFD simulations were compared to experimental results from a previous AFIT thesis and conclusions were drawn based on whether or not the current wind tunnel setup at AFIT is capable of performing analyses of supersonic store separations. Also included in this research is a study of supersonic base pressure profiles, near-wake velocity profiles, wind tunnel shock interactions and force/moment studies on a conical store and parent vehicle.

This thesis provided the ground work for future CFD studies relating to aft supersonic store separations. Eventually, this research will be used as the basis of dynamic store separations using the Beggar code. Once dynamic separations are possible, store trajectories and ejection forces can be studied in more detail for a number of different flight conditions.

15. SUBJECT TERMS

Computational fluid dynamics, base pressure, supersonic drag, stores, conical bodies

16. SECURITY CLASSIFICATION OF:			**17. LIMITATION OF ABSTRACT**	**18. NUMBER OF PAGES**	**19a. NAME OF RESPONSIBLE PERSON**
REPORT	**ABSTRACT**	**c. THIS PAGE**			Lt Col Ray C. Maple
U	**U**	**U**	**UU**	109	**19b. TELEPHONE NUMBER** *(Include area code)* (937) 255-3636, ext 4577; e-mail: Raymond.Maple@afit.edu

Standard Form 298 (Rev: 8-98)
Prescribed by ANSI Std. Z39-18